[IMPROVED UNDERSTANDING OF EARTHQUAKE INTERACTION WITH WAVEFORM MATCHING METHOD]

A Dissertation
Presented to
The Academic Faculty

by

[Chenyu Li]

In Partial Fulfillment
of the Requirements for the Degree
[Doctor of Philosophy] in the
[School of Earth and Atmospheric Sciences]

Georgia Institute of Technology
[August 2020]

[IMPROVED UNDERSTANDING OF EARTHQUAKE INTERACTION WITH WAVEFORM MATCHING METHOD]

Approved by:

Dr. Zhigang Peng, Advisor
School of Earth & Atmospheric Sciences
Georgia Institute of Technology

Dr. Felix Herrmann
School of Earth & Atmospheric Sciences
Georgia Institute of Technology

Dr. Andrew V. Newman
School of Earth & Atmospheric Sciences
Georgia Institute of Technology

Dr. Sheng Dai
School of Civil Engineering
Georgia Institute of Technology

Dr. James H. McClellan
School of Electrical Engineering
Georgia Institute of Technology

Date Approved: [July 24th, 2020]

ACKNOWLEDGEMENTS

I would like to express my deepest gratitude to my advisor Dr. Zhigang Peng for all of his mentoring and guidance during the last six years. He is very encouraging when I encounter challenges in my research and study, and is always providing valuable advices either in my current research or future career plans. His high standard on research results motivates me to think critically and continue to think about what else could be improved. I want to thank my committee members, Dr. Andrew Newman, Dr. James McClellan, Dr. Felix Herrmann and Dr. Sheng Dai for their constructive suggestions and help, which significantly improved this thesis. I also want to thank many (former) faculty and staff members in EAS, Dr. Josef Dufek, Dr. Christian Huber, Dr. Ken Ferrier, Dr. Robert Black and Dr. Martial Taillefert, Olivia Kulisz, Laura Cederquist, Natasha Lawson for their help and support during my Ph.D. at Georgia Tech (GT).

During the past six years, I've had many great opportunities to collaborate with excellent researchers from many institutes, including Dr. Guoming Liu, Dr. Zhongwen Zhan, Dr. Haijiang Zhang, Dr. Jing Wu, Dr. Chengyuan Zhang, Dr. Nori Nakata, Dr. Tim Sickbert, Dr. Yufang Rong, Dr. Jing Du. I've learned so much by working with them. I really appreciate former GT students Dr. Xiaofeng Meng, Dr. Dongdong Yao, Dr. Zefeng Li, Dr. Chastity Aiken and Dr. Yanqing Su for their help. When I first came to GT with little experience in research and life in the US, they gave me plenty of guidance and advice, ranging from data processing, presentation skills, to adjusting life in the US. I also want to thank all the colleagues and friends I met in GT, Dr. Lijun Zhu, Dr. Hao Guo, Dr. Amy Williamson, Dr. Tiegan Hobbs, Dr. Lucas Liuzzo, Dr. George McDonald, (soon

to be Dr.) Justin Lawrence, Dr. Lu Li, Dr. Xin Cao, Dr. Longlei Li, Dr. Shuozhi Xu, Qiushi Zhai, Lindsay Chuang, Clara Daniels, Miguel Neves, Mingyu Ji and many others.

I would also like to thank my friends and family in the Westminster Christian Fellowship and North Avenue Presbyterian Church, especially Jason and Jasmine Chen, Carol and Neale Hightower and so many others, for all their help and prayers, and the precious time we spent together.

Finally I want to thank my parents for their selfless love and believing in me. I also would like to thank my husband Bin Wu for his endless love and support. He always reminds me to work harder when I take pride in little achievement or start procrastinating, and we are accompanying each other through the hard yet meaningful Ph.D. journey at GT, and surely every journey for the rest of our lives.

TABLE OF CONTENTS

LIST OF TABLES

LIST OF FIGURES

LIST OF SYMBOLS AND ABBREVIATIONS

WFMF	Waveform Matched-filter Technique
UNE	Underground Nuclear Explosion
SSGF	Salton Sea Geothermal Field
CNN	Convolutional Neural Network
PGV	Peak Ground Velocity

SUMMARY

As one of the most common natural phenomena, earthquakes occur along active faults at various geological settings, such as major plate boundaries, active volcanoes, and oil/gas production sites. The stress changes caused by a large earthquake are capable of triggering additional seismicity from near-field to far-field. A better understanding of the triggering mechanism among diverse seismic events is significant for better deciphering fundamental fault-slip behaviors as well as mitigating seismic hazards.

To achieve these goals, detailed documentation and analysis of microseismicity are essential. Traditional earthquake catalogs built by analysts or simple automatic algorithms tend to miss weak events buried in the coda wave of large earthquakes or high background noise, resulting in an incomplete catalog. In this study, a semi-automatic template-matching earthquake detection method is utilized to detect weaker seismic events and build a more complete catalog. This method cross-correlates waveforms of known events with continuous data and detects new events with high waveform similarities. It has been widely applied to detect microearthquakes before and after major earthquakes, and low-frequency earthquakes within continuous tectonic tremors.

During my Ph.D. study, I applied the template matching method to study dynamically triggered earthquakes in volcanic and geothermal regions and an aftershock sequence of an intermediate-depth earthquake. Volcanic and geothermal regions are particularly sensitive to stress changes caused by surface waves of large distant earthquakes. I systematically searched for remotely triggered events in three volcanic/geothermal regions: the Changbaishan volcano in China, Mount Erebus volcano

in Antarctica, and the Salton Sea Geothermal Field in California, USA. In the Changbaishan region, I found clear high-frequency local signals during the 2004 Mw 9.3 Sumatra and 2011 Mw 9.0 Tohoku earthquakes. In addition, a 3-year volcanic unrest was likely delay-triggered by a magnitude 7.2 deep-focus earthquake in June 2002. Next I applied the template matching method to automatically detect triggered micro-earthquakes in the Mt Erebus and Salton Sea Geothermal Field (SSGF) in Southern California. I also found triggering of high-frequency signals at Mt. Erebus following the 2010 Mw 8.8 Maule earthquake, and triggered events around the SSGF following 6~7 M>5.5 earthquakes at regional distance. The diverse observations of dynamic triggering in these regions indicate that the triggering mechanism is site specific.

Using the template matching method, I searched for early aftershocks following the 2015 Mw7.5 Hindu Kush intermediate-depth earthquake. I detected more than 2000 aftershocks within 35 days of the 2015 Mw7.5 Hindu Kush earthquake, which is about 14 times more than listed in the standard catalog. The relocated aftershocks show nearly vertical alignment, and are around the region with large slip during the mainshock. This study demonstrated that the aftershock activity of earthquakes deeper than 200 km could be comparable to that of shallow earthquakes, and highlights the potential to improve deep earthquake catalogs with the template matching method.

Additionally, I also worked on seismic event detection with other newly-developed methods. The local similarity method was applied to a large-N array in Oklahoma to search for both small-magnitude earthquakes and long-period long-duration seismic events. I also demonstrated the potential for transfer learning by applying a convolutional-neural-network (CNN)-based Phase Identification-Classifier (CPIC) on

several different regions, and the results showed that CPIC could be applied to regions with relatively small datasets. These studies offer new opportunities to automatically detect seismicity in regions without many previous catalog events as templates.

CHAPTER 1. INTRODUCTION

Thanks to the rapid development in observational seismology and seismic data processing, our understanding of the Earth's interior structures and seismic phenomena has been greatly improved since last century. The Elastic-Rebound Theory states that earthquakes are sudden release of accumulated energy on a fault as the Earth's crust deforms (Reid, 1911). With the establishment of the Plate Tectonics theory and dramatic improvements in geological/geophysical observations, slow tectonic movements and sudden violent natural events occurring on and beneath the Earth's surface, such as mantle convection, earthquakes and volcanic eruptions, have been gradually revealed to us. In addition to regular earthquakes, scientists have discovered different types of fault-slip behaviors, and enormous efforts have been spent to better understand how earthquakes interact with each other, and with other geological phenomena, such as volcanic eruptions, tsunamis, storms, landslides, etc.

The mechanisms of interactions among various seismic events are important for better understanding of fundamental fault-slip behaviors and mitigating future seismic-related hazards. This thesis focuses on utilizing large-scale detection and precise relocation of seismic events, and using the expanded seismic catalogs to improve our understanding of earthquake interactions in different regions. In this chapter, I first summarize previous studies on fault-slip behavior and earthquake triggering, and then give an overview on earthquake detection methods. Chapters 2-6 are case studies that I have worked on in the past 6 years. Chapter 2 is about earthquake triggering in volcanic regions, and Chapter 3 focuses on detecting microseismicity in Salton Sea Geothermal

Field with a GPU-based waveform matched-filter technique. Chapter 4 focuses on detecting early aftershocks of the 2015 M7.5 Hindu-Kush intermediate-depth earthquake. Chapter 5 is a case study of detecting long-period long-duration signals in Oklahoma with the local-similarity earthquake detection method and Chapter 6 is case study using Convolutional Neural Network for seismic phase picking and earthquake detection.

1.1 Earthquake triggering and various types of seismic events

The majority of earthquakes occur on plate boundaries due to relatively fast motion between rigid lithospheric plates. There are three types of plate boundaries: divergent, convergent and transform boundaries, categorized by the relative movements between two plates. Accordingly, there are three types of faults: normal, reverse (also known as thrust) and strike-slip faults. Earthquakes could happen as deep as 700 km in the mantle transition zone, but also occur beneath active volcanoes, or fast-moving glaciers.

1.1.1 Earthquake triggering

Earthquake triggering has been widely observed since wide-spread increases in microseismicity from near-field to long-range distances were reported following the 1992 M7.3 Landers Earthquake in Southern California (Hill et al., 1993; King et al., 1994). After an earthquake, there are various types of stress changes that are capable of triggering seismicity from near-field to far-field, such as co-seismic static stress change, post-seismic quasi-static stress change, and dynamic stress changes (e.g., Freed, 2005; Brodsky and van der Elst, 2014; Hill and Prejean, 2015; and references therein). The changes of the permanent static stress and quasi-static stress changes could lead to changes in seismicity at nearby region (i.e., aftershock zone), while dynamic stress perturbations carried by passing surface waves can propagate further away and play

dominant roles in remotely triggering activities (Gomberg et al., 2001; Hill and Prejean, 2015). Hence, dynamic stress is mainly responsible for the increase of seismicity beyond traditional aftershock zones (Kilb et al., 2000). There are also clear evidence suggesting that transient dynamic change is important in the traditional aftershock zone in addition to the permanent stress changes (Pollitz and Johnson, 2006; Toda et al, 2012; Meng et al., 2013; Hill and Prejean, 2015). In addition to triggering seismicity during the passage of mainshock seismic waves, some studies also observed triggered activities with time delays since the perturbing waves ranging from minutes to days. These delays are potentially related to secondary triggered phenomenon (e.g., fluid movements, slow slip) or changes in fault frictional properties (Freed, 2005; Parsons, 2005; Shelly et al., 2011; van der Elst and Brodsky, 2010; Brodsky and van der Elst, 2014).

1.1.2 Slow earthquakes

A broad spectrum of seismic events has been discovered in the last decades, ranging from regular earthquakes to slow earthquakes. The latter include low-frequency earthquakes (VLF) and deep tremors, very-low-frequency earthquakes (VLE), and slow slip events (SSE) (e.g., Obara 2002; Rogers and Dragert, 2003; Peng and Gomberg 2010; Beroza and Ide, 2011; Obara and Kato, 2016). Tectonic tremor has emergent waveforms and last from minutes to hours, longer than regular earthquakes. Shallow earthquakes mostly nucleate in brittle portion of seismogenic crust, while deep tectonic tremors and SSEs mainly occur below the brittle-ductile transition zone at depth of 20-40 km along plate-boundary faults (Peng and Gomberg 2010; Beroza and Ide, 2011). Deep tremors and SSEs are discovered in most major subduction zones, while shallow tectonic tremors are only observed in a few selected regions (i.e. To et al., 2015; Wallace et al., 2016;

McGuire et al., 2018). Slow earthquakes are highly sensitive to external stress perturbations along subduction zones and might be used to forecast occurrence of future large megathrust earthquakes (Obara and Kato, 2016).

1.1.3 Volcanic seismicity

Similarly, there are different types of seismic events around active volcanoes (McNutt, 2005): volcano-tectonic (VT) earthquakes, which reflects brittle failure on a fault in volcanic regions; volcanic tremors, continuous ground vibrations commonly observed at volcanoes, some of them showing harmonic signals on spectra; long-period (LP) or low-frequency (LF) events, likely originating from low crust or upper mantle (15-30 km); and explosion earthquakes that are commonly observed during explosive eruptions.

1.1.4 Deep earthquake

Earthquakes with hypocentral depth greater than 70 km are termed as deep earthquakes, and they could be further categorized into intermediate-depth earthquakes between 70 km and 300 km, and deep-focus earthquakes below 300 km (Wadati, 1928; Frohlich, 1989, 2006; Houston, 2015). Intermediate-depth and deep-focus earthquakes mostly occur along subduction plate boundaries, forming the so-called Wadati-Benioff zones (Wadati, 1928; Frohlich, 1989). The deepest recorded earthquakes are close to the bottom of mantle transition zone at ~700 km (Houston, 2015; Ye et al., 2016). Deep earthquakes only account for a small portion of the Earth's seismicity. For example, 18% of earthquakes with magnitude > 5.8 from 1977 to 2006 in the global centroid moment tensor (CMT) catalog are deeper than 100 km, and only 6 % between 400 km and 700 km (Houston, 2015). Although deep earthquakes generally produce less shaking than shallow

earthquakes with similar magnitudes due to their larger depths, they are widely felt at greater distances from the epicenter. Some of them could cause damages, especially in regions without strict building codes (Frohlich, 2006). Seismic radiation and focal mechanism of deep earthquakes mostly indicate predominant shear failure plane, consistent with a double-couple focal mechanism and similar to shallow earthquakes (Green and Houston, 1995; Wiens 2001; Green and Marone, 2002; Houston, 2015; Ye et al., 2016). However, the stress drop of deep earthquakes are generally larger than shallow earthquakes (Wiens, 2001; Liu et al., GRL, 2020).

Deep earthquakes also show some differences in focal mechanisms and statistical properties as compared with shallow earthquakes. For example, some of them have clear non-double-couple components and their *b*-values and aftershock productivities show large variations in different regions (e.g., Houston, 2015; Poli et al., 2016a, 2016b; Zhan, 2017). Furthermore, deep earthquakes occur well below depths where brittle failures would occur, requiring alternative weakening mechanisms (Green and Houston, 1995; Frohlich, 2006). At present, the underlying physical mechanisms of deep earthquakes are still in debate (e.g., Houston, 2015). These include dehydration embrittlement (Rayleigh and Paterson, 1965; Petit and Barquins, 1988; Houston 2015), transformational faulting (Green and Houston, 1995; Kirby et al., 1996; Houston 2015), and thermal shear instability (Ogawa, 1987; Hobbs and Ord, 1988; Karato et al., 2001; Poli et al., 2016a).

The interaction of deep earthquakes with either deep or shallow earthquakes are not well studied, but there were a few case studies showing large deep earthquakes can trigger other earthquakes beyond their traditional aftershock zones (Myers et al., 1995; Tibi et al., 2003). Earlier studies demonstrated that deep earthquakes have smaller

number of aftershocks than shallow earthquakes (Kagan and Knopoff, 1980; Prozorov and Dziewonski, 1982; Frohlich, 1987; Persh and Houston, 2004). However, some deep earthquakes could produce relatively large aftershock sequences. For example, the March 1994 Tonga deep earthquake recorded 82 aftershocks decaying with the Omori's Law (Wiens et al., 1994; Nyffenegger and Frohlich, 2000). The Omori's Law (Omori, 1894; Utsu et al., 1995) describes how aftershock number decays with time,

$$n(t) = \frac{k}{(c+t)^p} \tag{1}$$

where $n(t)$ is the number of aftershocks after time t from the mainshock, and k is the productivity rate, p is the decay constant (typically p=1), and c is a time constant to avoid singularity at time t = 0.

The frequency (number) of earthquakes with certain magnitudes in a given region is controlled by their magnitudes, according to the Gutenberg-Richter Law (Gutenberg and Richter, 1944),

$$logN = a - bM \tag{2}$$

where N is the number of earthquakes larger than magnitude M, and the decay constant b value varies with regions with a global average of 1. The aftershock decay rate p value and b value of deep earthquakes show significant variabilities around the world (Wiens, 2001). It was suggested that b-value of deep earthquakes are higher in cooler slabs than warmer ones (Wiens and Gilbert, 1996; Persh and Houston, 2004; Houston, 2015; Zhan 2017). Aftershock productivity of deep earthquakes also showed clear variation with depth (Persh and Houston, 2004), with the aftershock productivity from 100 km to 300 km lower than shallow earthquakes above 100 km. The lowest productive region is

between 300 km and 500 km. Below 500 km the productivity of aftershock increases abruptly. This change might indicate different physical mechanisms of deep earthquakes (Houston, 2015).

1.1.5 Human-induced earthquake

Earthquakes induced by human activities such as oil and gas productions were recognized as early as the 1920s (McGarr et al., 2002). However in the last decade it became a more widely-discussed topic in both science and general society, largely due to an abrupt increase of injection-induced seismicity in central and eastern U.S, such as Oklahoma, Texas, etc. (e.g., Ellsworth, 2013; Weingarten et al., 2015; Frohlich et al., 2016) and elsewhere around the world (Foulger et al., 2018; Lei et al., 2019; Atkinson et al., 2020). In addition, earthquakes can be induced by numerous of human activities, such as mining, dam impoundment, fluid injection, geothermal systems and hydraulic fracturing (Schultz, et al. 2017).

1.2 Catalog Incompleteness

In order to better understand the physical mechanism of earthquake triggering, a complete earthquake catalog is needed. However, earthquake catalogs following large earthquakes are suspectable to missing small events because of the masking from the coda waves of the mainshock and large aftershocks (e.g., Kagan, 2004; Peng et al., 2006, 2007). In addition, the paucity of recorded aftershocks for deep earthquakes could also be related to their incomplete catalogs. An effective way to detect missing small-magnitude events from conventional catalogs is the aforementioned waveform matched-filter technique (WMFT) (Gibbons and Ringdal, 2006; Shelly et al., 2007; Peng and Zhao, 2009). It utilizes waveforms and travel time information of known events as templates, or

"matched filters" (Shearer, 1994), to search for similar patterns in the continuous recordings. WMFT has been successfully applied to detect missing earthquakes before (e.g., Kato et al., 2012, 2014; Walter et al., 2015; Ruan et al., 2017) and after large shallow earthquakes (Peng and Zhao, 2009; Meng et al., 2013; Meng and Peng, 2014), as well as low-frequency earthquakes within deep tectonic tremors (Shelly et al., 2007, 2011). In this thesis, I apply the WMFT to study dynamic triggered earthquakes in volcanic and geothermal regions, as well as aftershock sequences of intermediate-depth earthquakes.

1.3 Event Detection

Event detection, classification and location are essential components of seismological studies and provide the basis for other subsequent analysis. Traditional earthquake catalogs are mainly based on manual picking by experienced analysts, and as discussed above, they could miss small-magnitude events or events buried in coda wave of large earthquakes. Classic automatic seismic phase-picking methods transform seismic waveforms to characteristic function (CF) such as short-time average/long-time average (STA/LTA) (e.g., Allen, 1982; Earle and Shearer, 1994), envelope functions (Baer and Kradolfer, 1987) and apply subsequent detections on the CFs. Usually the seismic phase picking is followed by phase association which attribute phases on different stations to a common source. However, these methods also tend to miss events that have low signal to noise ratio. Techniques based on waveform similarities between adjacent stations or between events at nearby distances have greatly increased detection capability. The source-scanning algorithm detects and locates earthquakes or tremors based on the time-shifted envelope functions across a small network (Kao and Shan, 2004). Template-

matching utilizes known events as templates to look for events that are spatially close to them and have similar waveforms (Gibbons and Ringdal, 2006; Shelly et al., 2007; Peng and Zhao, 2009). Auto-correlation is an automatic method to detect events by computing cross-correlations between each short-time window with the rest windows (Brown et al., 2008). Recently several new algorithms are developed to deal with large volume of data recorded by seismic arrays. Local-similarity is a method that computes cross-correlation across stations in large-N array to enhance signals of seismic events that are too small to be detected by traditional methods (Li et al., 2018). Fingerprint and sensitive thresholding (FAST) is an automatic method that converts waveforms to subspace to detect repetitive events with large-T data (Yoon et al., 2015). Machine learning methods such as random forest and CNN have also demonstrates their power to detect and classify seismic events (e.g., Perol et al., 2018; Ross et al., 2018; Zhu and Beroza, 2018; Li et al., 2018; Zhu et al., 2019). In this thesis, we use the template-matching, local similarity and CNN-based event detection methods for different tasks.

CHAPTER 2. DYNAMIC TRIGGERING IN VOLCANIC REGIONS

In this chapter I present two case studies of remote dynamic triggering in volcanic regions. Section 2.3 focuses on the Changbaishan volcano near the border of China and North Korea. Some results have been published in Liu et al. (2017, GRL & 2020, in prep). They are included here, since I have contributed significantly in these studies. Section 2.4 focuses on dynamic triggering of icequakes/microearthquakes on Mount Erebus volcano in Antarctica.

2.1 Summary

We systematically investigate the dynamic triggering phenomena in two volcanic regions, the Changbaishan Volcano in northeast Asia and Mount Erebus in Antarctica, after distant (>1000 km) large (>M 7.0) earthquakes from 2000-2017. Our analysis is based on high-pass filtered waveforms following the large earthquakes, and we combine visual inspection, STA/LTA and matched-filter technique to search for possible triggered local events. For the Changbaishan Volcano, we find evidences of dynamic triggering after 3 distant earthquakes, and large earthquakes with higher amplitude in long-period surface waves are more likely to trigger seismicity. The Mount Erebus have less cases of dynamic triggering, and the clearest evidence after 2010 M8.8 Maule earthquake shows high-frequency triggered seismicity during the short-period surface waves.

2.2 Introduction

Volcanic seismicity is sensitive to transient disturbances such as tidal stress and passing seismic waves (Kawakatsu and Yamamoto, 2015; Enescu et al., 2016). Previous

studies showed that volcanic and geothermal regions are more suspectable for being triggered than other regions by distant earthquakes (Aiken and Peng, 2014; Hill and Prejean, 2015). For example, remote triggering of volcanic seismicity was observed at the Long Valley Caldera following the 1992 Landers and 1999 Hector Mine earthquakes, and the Yellowstone National Park Region following these two events and the 2002 Denali Fault earthquake (Hill et al., 1993; Hill et al., 2002; Husen et al., 2004). The abundance of fluid in volcanic/geothermal regions is a possible explanation for their sensitive response to external disturbances (Brodsky et al., 2003; Brodsky and Prejean, 2005; Kawakatsu and Yamamoto, 2015).

To better understand whether dynamic triggering of volcanic seismicity is ubiquitous, one could compare how different volcanic regions respond to large earthquakes. The two study regions in this chapter are the Changbaishan Volcano in northeast Asia and Mt. Erebus in Antarctica, which are located in distinct geological settings. Furthermore, the proximity of Changbaishan Volcano to Japan Trench provides unique opportunity to study relationship between volcanic seismicity and both shallow and deep subduction-zone earthquakes, and Mt. Erebus might reflect interactions among local icequakes, volcanic activity and distant earthquakes.

2.3 Triggering study at Changbaishan Volcano

2.3.1 Introduction

The Changbaishan volcano is an intraplate stratovolcano located on the broader between Northwest China and North Korea, and it's about 1200 km from the plate boundary between Pacific Plate and Eurasia Plate (Figure 2.1). A major explosive eruption with a Volcano Eruption Index of 7 occurred in 946 AD., and the latest eruption

is on 1903. It is proposed the magma reservoir of Changbaishan volcano is generated by upwelling of high-temperature asthenospheric material above a stagnant slab of the Pacific subducting plate (Zhao and Tian, 2009; Tang et al, 2014). Previous studies showed that the Changbaishan Volcano experienced an unrest period from 2002 to 2006, with a clear increase of volcanic earthquakes and more gas releasing from hot springs (Xu et al., 2012; Liu et al, 2017).

The Changbaishan Volcano has been instrumented with 11 seismic stations, 15 campaign GPS measurement sites, 2 precision leveling lines, and 3 hotspring gas monitoring stations since 1999 (Xu et al, 2012). As a collaborative work with researchers in the Changbaishan Volcano Observatory and the Earthquake Administration of Jilin Province, we conduct a systematic study of dynamically triggered volcanic seismicity on Changbaishan since 2000 (Liu et al, 2017; Liu et al, 2020, in prep). The propose of our study is to better understand the volcanic seismicity on Changbaishan Volcano and how they might interact with other shallow and deep earthquakes, as well as Underground Nuclear Explosions (UNEs) in North Korea.

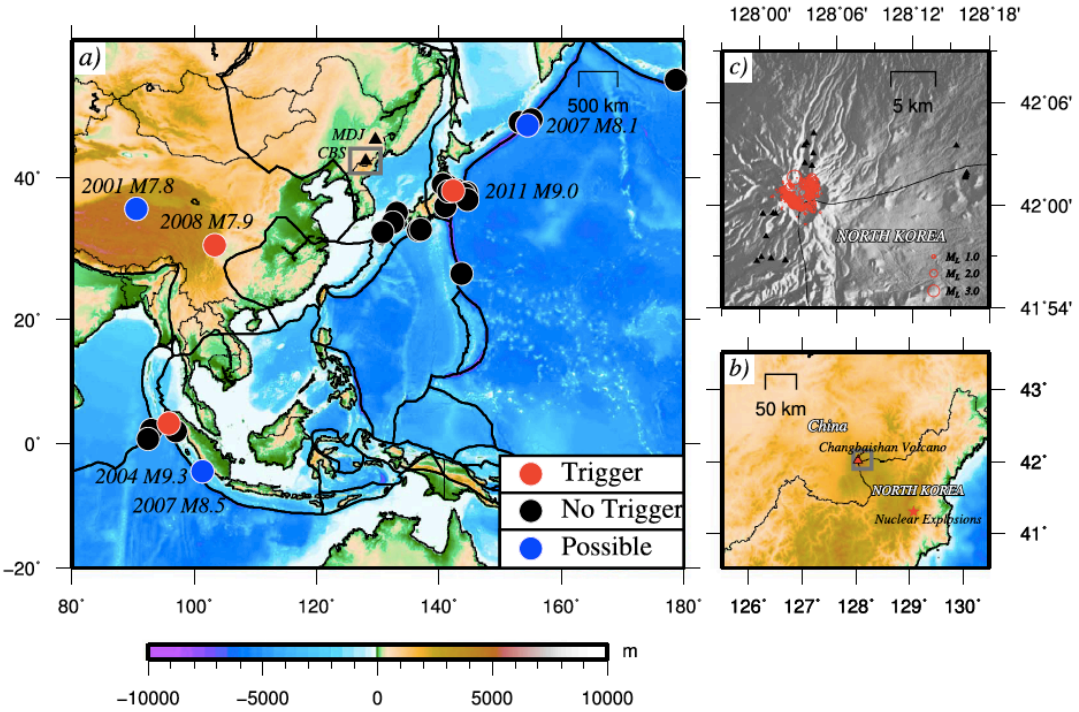

Figure 2.1. (a) Location of Changbaishan Volcano and distributions of all distant earthquakes examined. Thick black lines show plate boundaries from Bird (2003). The black triangle represents stations CBS and MDJ. The gray box marks a zoom-in plot in (b). (b) Locations of Changbaishan Volcano (red triangle) and underground nuclear explosion sites (red stars). (c) Locations of CBS station (black triangle) and relocated earthquakes during 2002–2004 from Xu et al. (2012). Modified from Figure 1 in Liu et al (2017).

2.3.2 Remote triggering by distant earthquakes and nuclear explosions

The goal of this study is to search for and analyze remote triggered seismicity on Changbaishan Volcano after large distant shallow earthquakes, such as the 2004 M9.2 Sumatra earthquake, 2011 M9.0 Tohoku earthquake, the 2012 M8.6 Indian Ocean earthquake, as well as five UNEs from 2006-2016 in North Korea (Figure 2.1). The analysis procedure generally follows Aiken and Peng (2014) and is briefly described here. A total of 26 large distant earthquakes are selected from the Advanced National Seismic System (ANSS) catalog from January 2000 to August 2016 with the following the threshold: magnitude above 7.0; distance from Changbaishan Volcano larger than 1000

km; depth less than 100 km; and predicted dynamic stress change on station CBS higher than 5 kPa. The predicted stress is estimated with the empirical ground-motion relationship based on magnitude and distance from earthquakes (van der Elst and Brodsky, 2010). We then apply high-pass (5 Hz) filter to waveforms 5 hours before/after the large earthquakes and UNEs, and carry out manual-picking for local micro-earthquakes. Because the high-frequency components of mainshock decays rapidly with distance, we could better observe local signals without contamination from mainshock or aftershocks with high-pass filtering. In addition, we generate spectrograms to help visually identify and characterize potential triggered events (Peng et al., 2011).

Three of the 26 large distant earthquakes triggered seismicity in Changbaishan Volcano: the 2004 M9.2 Sumatra earthquake and 2008 M7.9 Wenchuan earthquake, and the 2011 M9.1 Tohoku earthquake. The catalog seismicity, logarithm of envelope and high-pass filtered waveforms, and spectrograms around the 2004 M9.2 Sumatra earthquake, 2008 M7.9 Wenchuan earthquake, and 2011 M9.1 Tohoku earthquake are shown in Figure 2.2 and Figure 2.3. The spectrograms on the bottom reveal how the amplitudes of different frequency ranges involve with time. As shown in Figure 2.2f and Figure 2.3f, the local events with high frequencies are well correlated with the surface waves of the 2004 Sumatra earthquake and 2008 Wenchuan earthquake, which is typical for dynamically triggered seismicity. The magnitudes of manually detected events in Figure 2.2 and Figure 2.3 are estimated in the same way as the catalog events with the equation:

$$M_L = logA + R(\Delta) \tag{3}$$

where $A(\mu m)$ is the average maximum amplitude of North-South and East-West components and $R(\Delta)$ is a function of epicentral distances, which is estimated from the S–P differential time.

The significance of seismicity increase is evaluated with the β-statistic value (Matthews and Reasenberg, 1988; Gomberg et al., 2001; Aron and Hardebeck, 2009). The β-statistic value is computed by

$$\beta = \frac{N_a - N(T_a/T)}{\sqrt{N(T_a/T)(1 - T_a/T)}} \tag{4}$$

where T_a is the time window considered for triggering, T is the total 10-hour time window, and N_a and N are event numbers in T_a and T, respectively. For a triggering window only during the surface wave, it is estimated as the time window between surface wave velocity of 2 km/s and 5 km/s. When the β-statistic value is higher than 1.96, it indicates that the seismicity increase is significant with 95% confidence (Hill and Prejean, 2015). The β-statistic value for the 2004 M9.2 Sumatra earthquake is 3 if the triggering window is 5 hours following the mainshock, and 6.78 if the triggering window is set to be the surface wave window, suggesting the events shortly after the mainshock are dynamically triggered.

The triggered events are not counted in cumulative number for the 2011 Tohoku earthquake because of their unclear P-S arrival times. A simple short-time average over long-time average algorithm with a threshold of 1.5 is applied to detect events 5 hours before/after the 2011 Tohoku earthquake, and the β-statistic values are 0.14 and 9.97 for 5-hour and surface wave triggering windows, respectively. Together with the fact that

envelope function of these high-frequency events is in phase with the long-period surface waves, the 2011 Tohoku earthquake is considered as a triggering event.

The case for the 2008 M7.9 Wenchuan earthquake is complicated due to clipping of waveforms. After a detailed visual inspection, we could still identify some locally triggered events. This is because the three components are not clipped at the same time. For example, when the vertical component is clipped around 940s, the north component is recording on scale. Finally, the β-statistic values are 1.3 and 3.9 for 5-hour and surface wave triggering windows respectively, again indicating that they are dynamically triggered local microearthquakes. For the five UNEs, none of them trigger any local seismicity recorded at station CBS. For example, no high-frequency local signal is observed during the seismic wave of the 2016 M5.1 UNE (Figure 2.3).

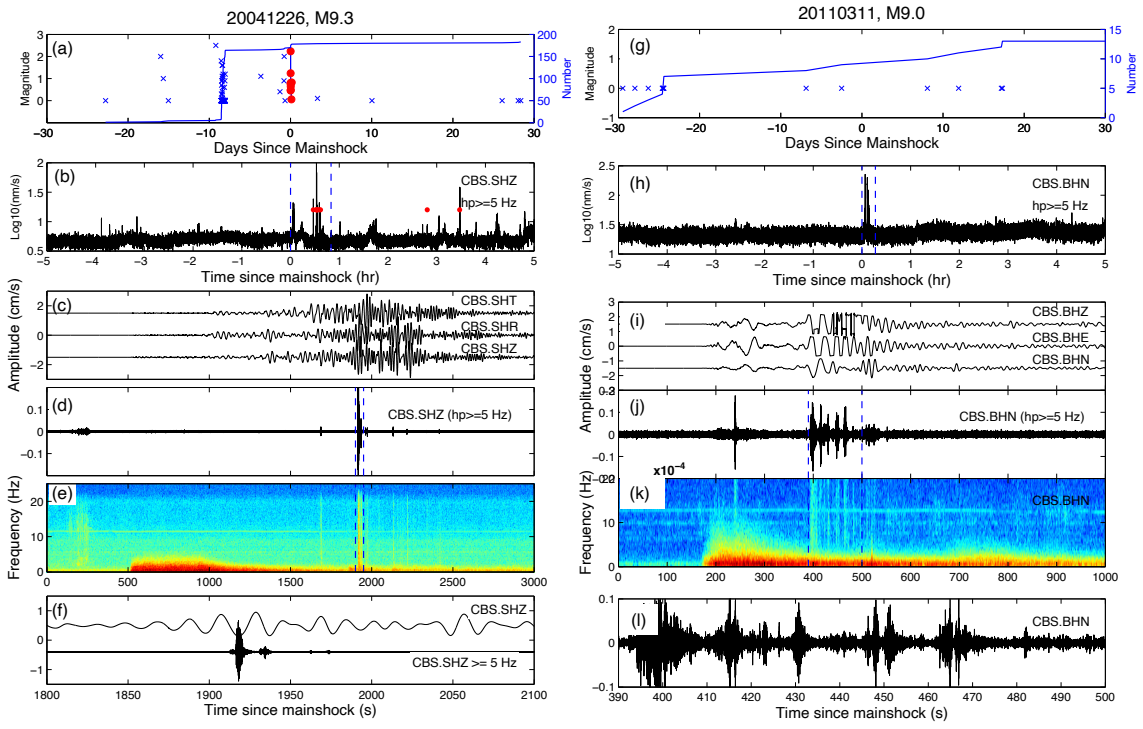

Figure 2.2. (a) Seismicity within 30 days before and after the 2004 M9.3 earthquake, the crosses mark events on the local catalog, and red dots mark hand-picked events 5 hours before and after the mainshock, the thick gray line marks cumulative number of

earthquakes. (b) Envelope function of high-pass filtered 5 Hz waveform 5 hours before and after the 2004/12/26 M9.3 Sumatra earthquake. The manually picked earthquakes are marked as black and red dots, representing before and after the teleseismic P waves, respectively. Blue dotted lines indicate the time range in (c). (c) Three-component seismograms showing the teleseismic waves of the Sumatra mainshock. (d) 5-Hz high-pass filtered vertical component showing triggered seismicity. (e) Spectrogram of (d), black dotted lines indicate time range in (f). (f) A zoom-in of waveforms showing triggered seismicity. (g)-(l) Same as for the 2011 M9.0 Tohoku-Oki earthquake.

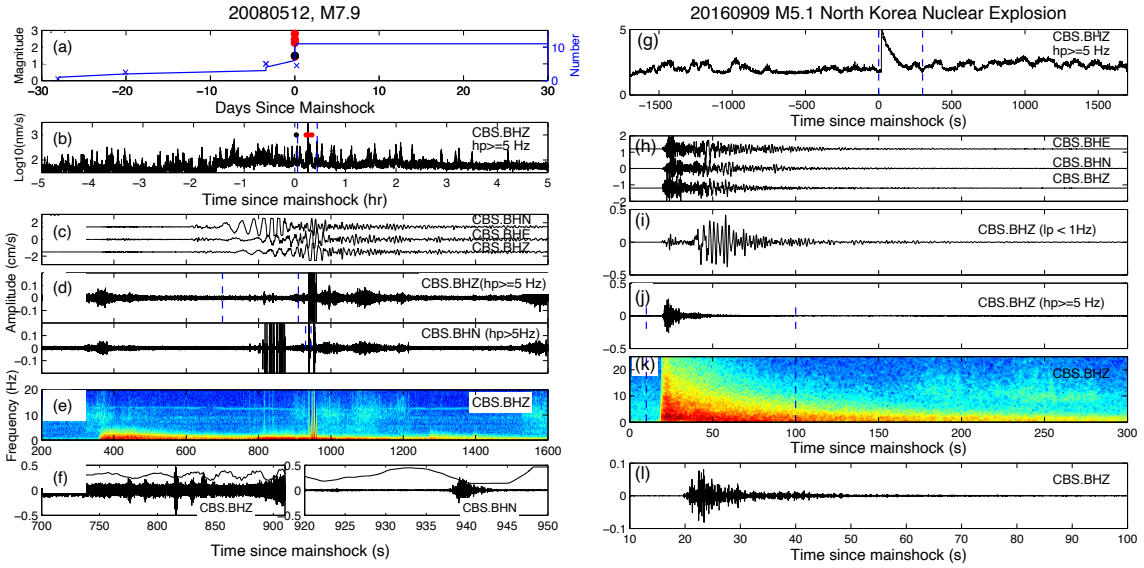

Figure 2.3. (a)-(f) same as Figure 2.2 for 2008 M7.9 Wenchuan earthquake. (d) 5-Hz high-pass filtered vertical and north component. (e) Spectrogram for vertical component in (d). (f) Zoom-in of waveforms showing triggered seismicity. (g) Envelope function of high-pass filtered 5Hz from 0-300s for the 2016/01/06 UNE. (h) Three components of original waveform showing the UNE. (i) 1-Hz low-pass filtered, (j) 5-Hz high-pass filtered and (k) spectrogram of vertical component. (l) Zoom-in of (j) showing no triggered seismicity. Modified from Liu et al. (2017).

There are also some distant earthquakes with possible triggering: the 14 November 2001 M7.8 Kunlun, 13 January 2007 M8.1 Kuril Island, and 12 September 2007 M8.5 Sumatra earthquakes. Some high-frequency signals are observed during their large-amplitude surface waves. However, there is lack of strong evidence to confirm a strong triggering relationship. These events are not considered as positive cases mainly because the waveforms before the mainshocks are so noisy that the β-statistic value

based on manual-picking is not reliable to conclude that the local events during surface waves are triggered. The envelope, waveforms and spectrogram of these possible events are displayed in Figure 2.4. The waveforms shown in Figure 2.5 are examples for no evidence of triggering.

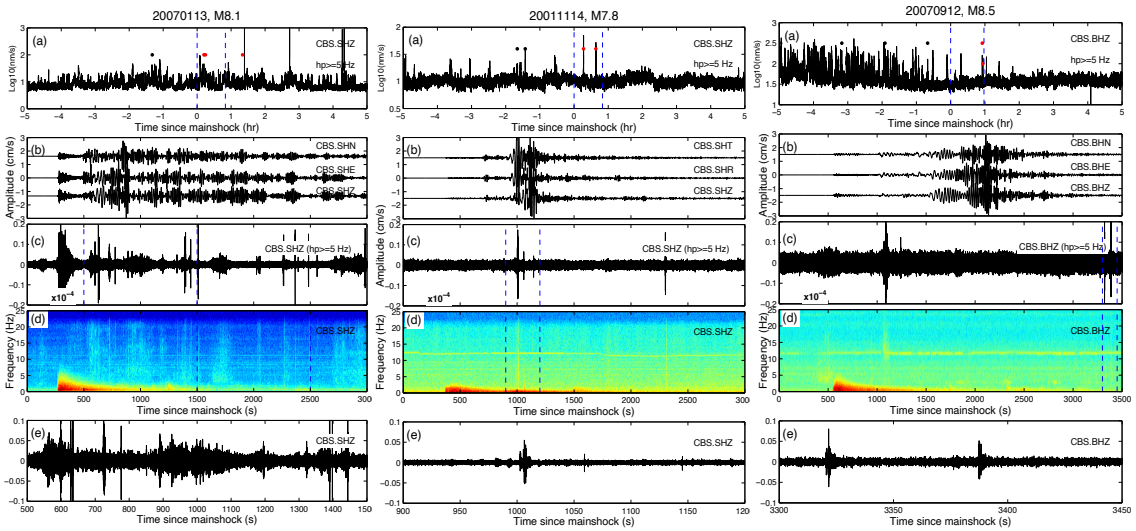

Figure 2.4. Three cases with possible evidence of triggering. (Left) 2001/11/14 M7.9 Kunlun earthquake; (Middle) 2007/01/13 M8.1 Kuril Island earthquake; (Right) 2007/09/12 M8.5 Sumatra earthquake. Other symbols and notations are the same as in Figure 2.2.

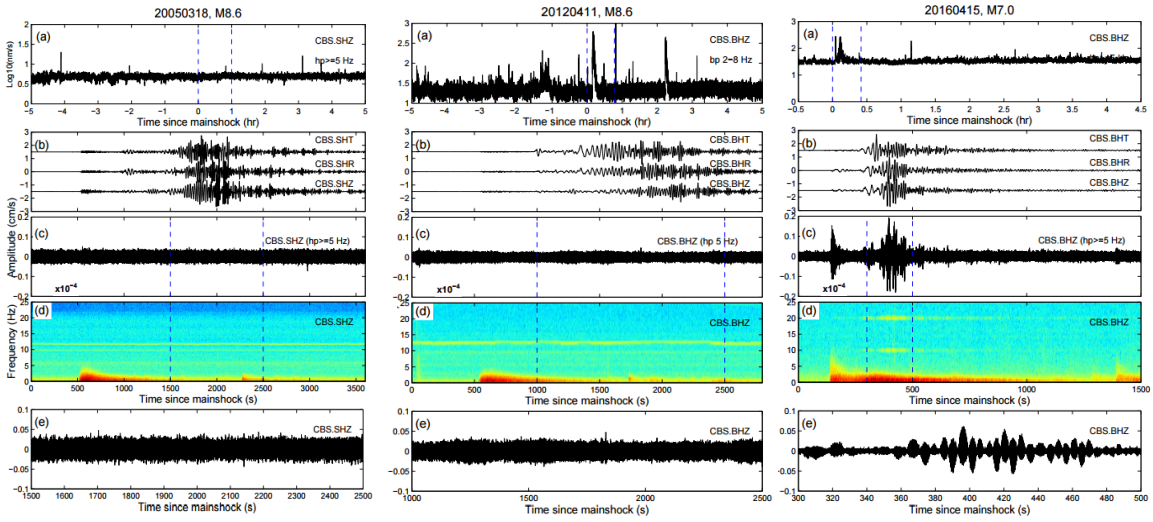

Figure 2.5 Examples of non-triggering earthquakes. (Left) 2005/03/28 M8.6 Nias earthquake; (Middle) 2012/04/11 M8.6 Indian Ocean earthquake; (Right) 2016/04/15 M7.0 Kumamoto earthquake. Other symbols and notations are the same as in Figure 2.2.

Next we examine possible triggering threshold for the Changbaishan volcano. We compare the peak dynamic stress change of recorded surface waves on station CBS and MDJ for all the earthquakes and UNEs (Figure 2.6). The peak dynamic stress change is estimated from peak ground velocity (PGV),

$$\sigma_d = \frac{\mu(PGV)}{V_{ph}} \tag{5}$$

here the nominal shear rigidity μ is 30 GPa and phase velocity V_{ph} is 3 km/s for the surface Rayleigh waves. Figure 2.6a,b shows the dynamic stress changes for all distant earthquakes and the North Korea's UNEs with a low-pass filter of 1 Hz and 30 s, respectively. The triggering events such as the 2001 M7.8, 2008 M7.9 and 2011 M9.0 earthquakes all have higher dynamic stress changes with a low-pass filter of 30s. It is also supported by the amplitude spectra of all events, where the three positive triggering and possible triggering events have higher energies at longer periods (lower frequencies). The dynamic stress and amplitude spectra for another broadband station IC.MDJ (about 200 km from CBS) is consistent with CBS observations. Therefore, the dynamic triggered seismicity on Changbaishan Volcano are likely controlled by long-period (low-frequency) seismic energy, and the triggering threshold may be slightly lower during the unrest period from 2002-2007.

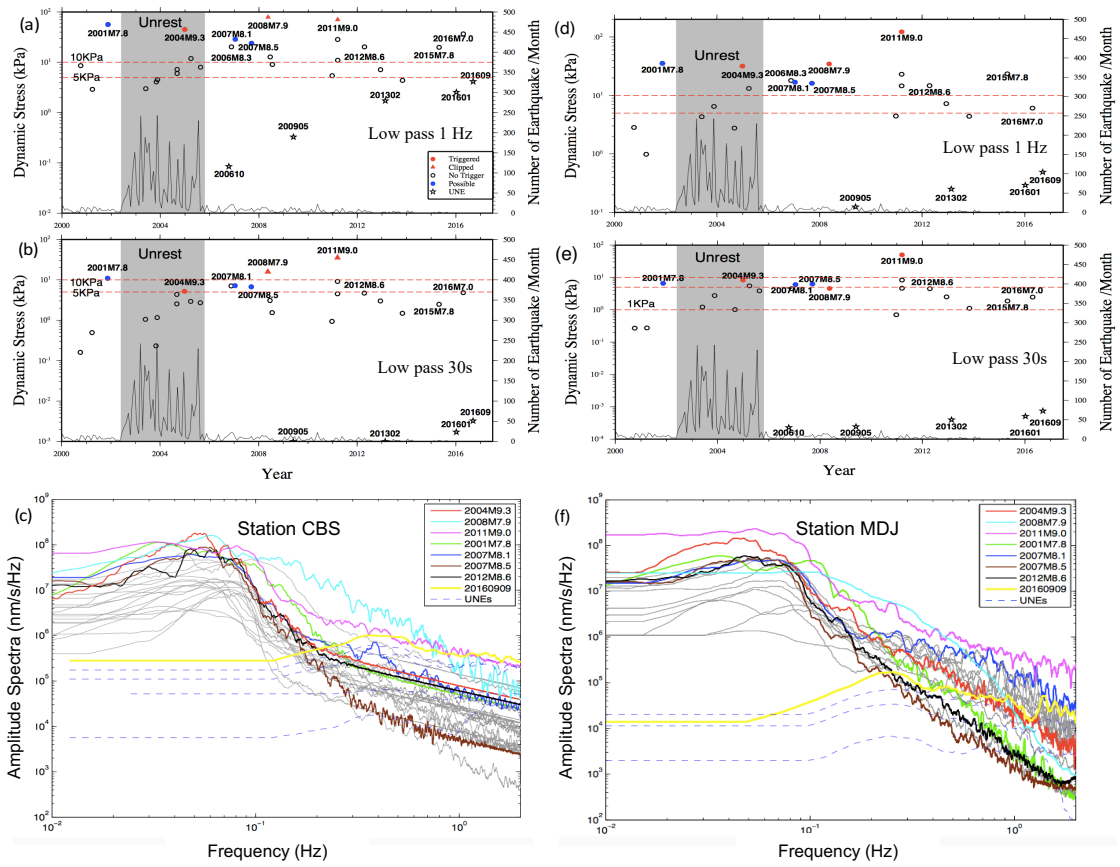

Figure 2.6. Peak dynamic stresses versus occurrence times of (a) low-pass filtered 1 Hz, (b) low-pass filtered 30s. Red, blue and black dots mark events that show positive, possible and no evidence of triggering, and red triangles are events with clipped recordings. The black stars mark the 5 UNEs since 2006. The black line shows the monthly earthquake rate, and the gray area marks the volcanic unrest period between 2002-2005 (Xu et al., 2012). The two red dashed lines mark the apparent triggering threshold of 5 and 10 kPa. (c) Amplitude spectra for all the events. (d)-(f) Same as (a)-(c) for data recorded at station MDJ, a broadband station located in Jilin Province, China. Modified from Liu et al. (2017).

We note that in this region when dynamic triggering was found, all triggered events occurred instantaneously during large-amplitude surface waves, and there were virtually no changes in subsequent volcanic activities or long-term seismic activities. This suggests that the triggering behaviors of microseismicity and volcanic activities could be different. The only possible exception is that the aforementioned 2002-2005 volcanic

unrest (Xu *et al.*, 2012) occurred immediately following the 2002 Mw7.3 Wangqing earthquake. This will be discussed in the next section.

Although our study did not directly address the question on the triggering relationship between large distant earthquakes and major volcanic eruptions, they are still useful for improving our understanding of triggering behaviors at active volcanoes. Our results suggested that peak dynamic stresses of incoming waves, as well as their frequency contents are among the most important factors in controlling triggering behaviors. These findings are generally compatible with recent studies of dynamic triggering at other volcanic/geothermal regions (e.g., Aiken and Peng, 2014). Similar to monitoring major plate boundary faults (Brodsky and van der Elst, 2014), we suggest that seismic triggering behaviors at active volcanoes can be used to infer their stress states and sensitivity to external stress perturbations. These are important parameters that could be used for accurate estimations of seismic and volcanic hazards.

2.3.3 Triggered seismicity by deep earthquakes

A few days before the onset of a recent unrest period (2002-2005) on Changbaishan Volcano, a magnitude 7.3 deep earthquake occurred on June 28, 2002, near Wangqing, China, with depth of 566 km and about 290 km from Changbaishan. Deep earthquakes including the 2002 Wangqing earthquake occurred frequently on the Pacific subduction slab, to the east of Changbaishan magma in the mantle (Zhao and Tian, 2013). The 2002 M7.3 Wangqing earthquake occurred only a few days before the unrest of Changbaishan Volcano on July 5, 2002, indicating potential triggering relationship between them.

Here we applied a template-matching method named Match & Locate (Zhang and Wen 2015) to the continuous waveform on station CBS during unrest period from 2002-

2007 in Changbaishan volcano (Liu et al., in prep). Figure 2.7 shows seismicity from the newly detected catalog 15 days before/after the 2002 Wangqing earthquake. There is a slight increase within 1 day after the Wangqing earthquake, then the unrest started around 7 days after. The β-statistic value with triggering window of 30 days after the Wangqing earthquake is 7.39, suggesting a statistically significant increase of seismicity.

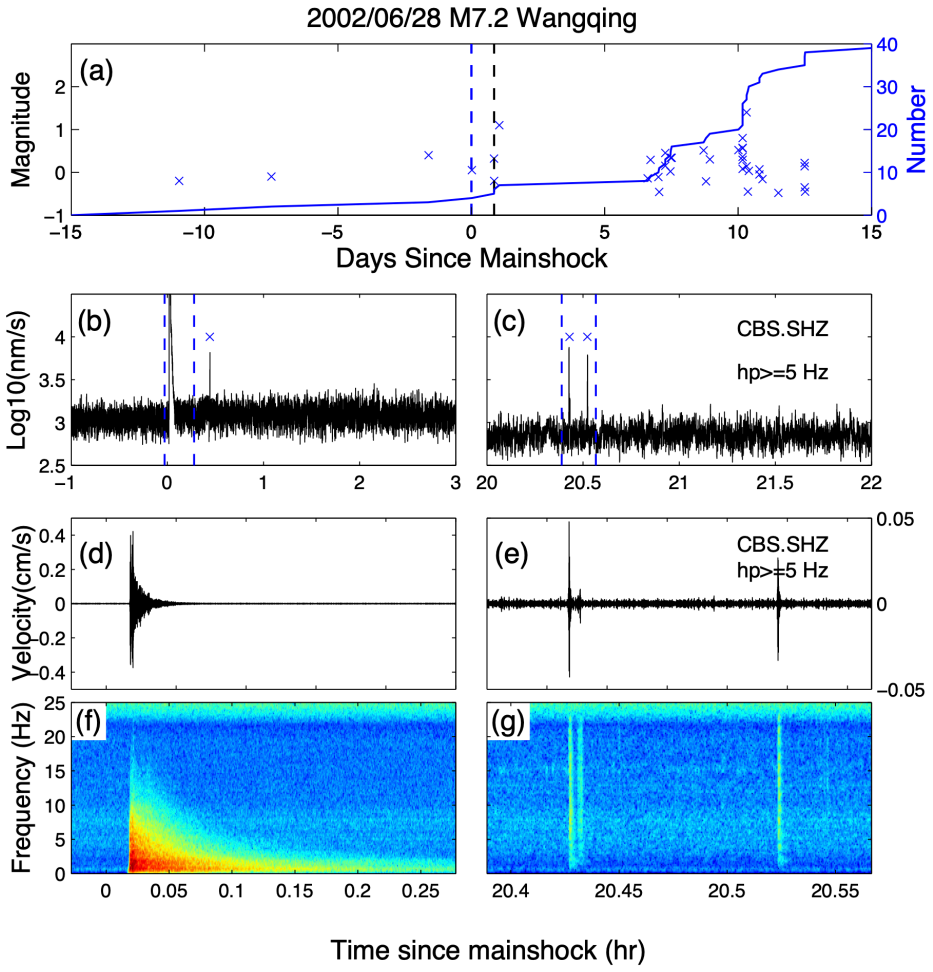

Figure 2.7. (a) Seismicity within 15 days before and after the 2002 M7.2 Wangqing earthquake, the crosses mark events listed in the newly detected catalogue, the blue line marks cumulative number of earthquakes. The red circle marks the original CHVO catalog. The vertical blue lines mark the time window plotted in (b) and (c). (b) – (c) Envelope functions of high-pass filtered 5 Hz waveform during and after the 2002 M7.2 Wangqing earthquake. The newly detected earthquakes are marked as blue crosses. (d) – (e) Zoom-in plots of blue dashed-lines in (b) and (c). (f) – (g) Spectrogram of (d) and (e).

We compared the peak ground velocities and estimated dynamic stress of other deep earthquakes with magnitude larger than 4 within 500 km from Changbaishan. As shown in Figure 2.8, the 2002 Wangqing earthquake has highest PGV compared to other deep earthquakes. Its PGA is also slightly higher than the large shallow earthquakes that have dynamically triggered shallow microseismicity near Changbaishan (Liu et al. 2017).

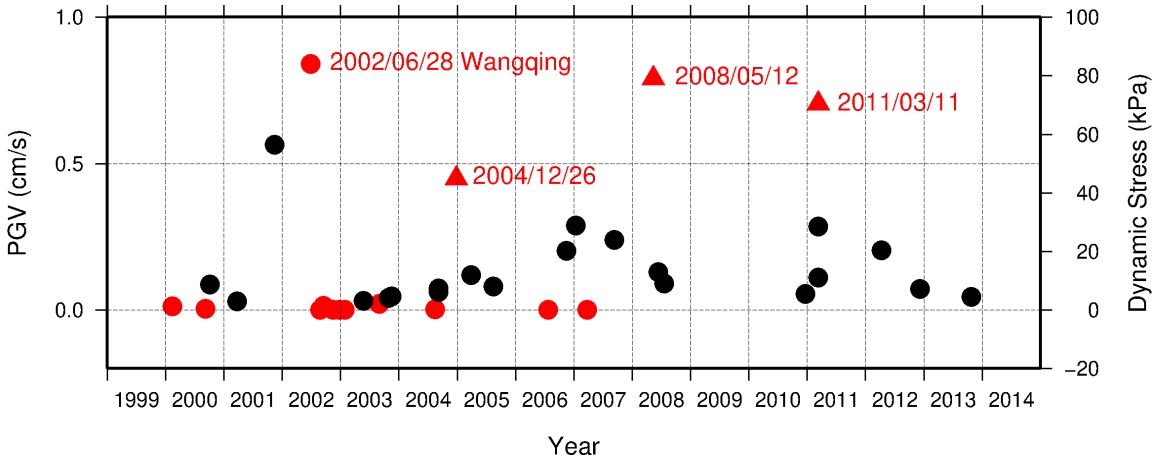

Figure 2.8. PGV and dynamic stress of deep-focus earthquakes and large distant earthquakes. Red circles represent deep-focus earthquakes within 500 km. Black circles represent large distant earthquakes beyond 1000 km. Three large distant earthquakes that dynamically triggered micro-seismicity in Changaishan volcano are marked by red triangle.

The amplitude spectra of the Wangqing earthquake and other shallow triggering earthquakes are shown in Figure 2.9, and the Wangqing earthquake produced higher seismic energy in the few second period range than other large distant earthquakes. Brodsky and Prejean (2015) demonstrated that long-period (>30s) waves are more effective at triggering seismicity in Long Valley Caldera, California, and they proposed that fluid flow could play an important role as a low-pass filter and respond to long-period wave triggering. The triggered seismicity by 2002 Wangqing Earthquake is likely a more complicated scenario if bubble pressurization in magma is involved, which is

likely independent of frequencies for the incoming seismic waves (e.g., Hill and Prejean, 2015; Brodsky and Prejean, 2015).

We hypothesize that the Changbaishan volcano was already in a state prone to active unrest. Hence, with a small disturbance from seismic waves of the deep Wangqing earthquake, magma in the crust began to move and drove the recorded seismic swarms. The magmatic movement is supported by the independent observation of increasing CO_2 and other gas emissions and ground deformations during the volcanic unrest period (Xu et al., 2012). However, because we did not have enough high-quality recordings to relocate all the seismicity, we cannot provide additional evidence for magmatic or fluid movements such as spatio-temporal migration of aseismic slip and seismic swarms (e.g., Shelly et al., 2016).

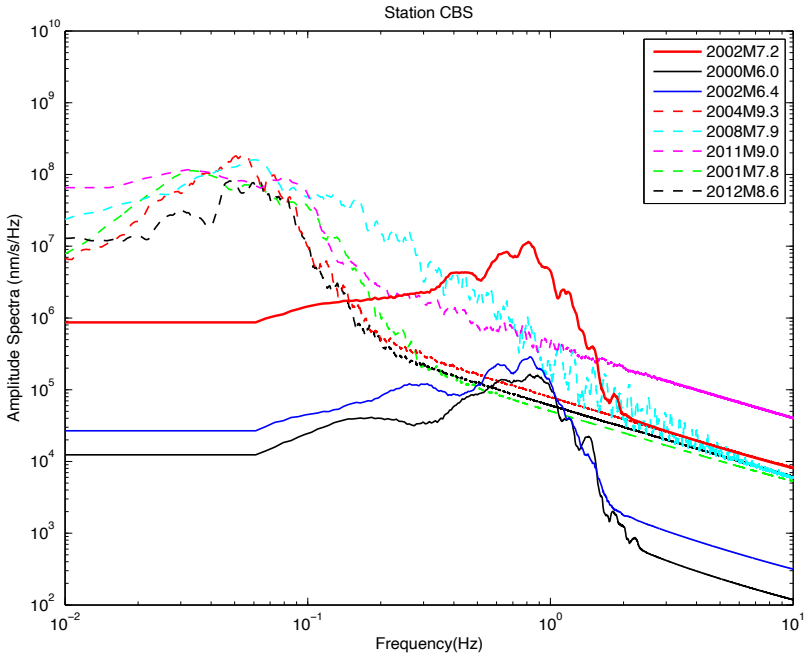

Figure 2.9. Amplitude spectra for the 2002 M7.2 Wangqing earthquake and two other M>=6 deep earthquakes on station CBS, dashed lines correspond to shallow distant earthquakes that have triggered or possibly triggered seismicity in Changbaishan.

2.4 Dynamic triggering at Mt. Erebus, Antarctica

Mt. Erebus is a large polygenetic stratovolcano located on Ross Island in Antarctica. It is the southernmost active volcano on Earth and is close to the Antarctic McMurdo Station (United States) and Scott Base (New Zealand). It is also heavily glaciated (Figure 2.10). The eruption style on Mt. Erebus is relatively mild Strombolian-type eruption with the volcanic explosion index of 1-3. With ongoing small-scale eruptions, persistent lava lakes, and existing monitoring infrastructures, it is a natural laboratory to study volcanic processes and interactions between volcanoes, earthquakes and ice movements.

This work is an extension of Peng et al. (2014) and Ji (2019), which found clear evidence of dynamic triggering in West Antarctica and the Antarctica Peninsula after the 2010/02/27 M8.8 Maule, 2012/04/11 M8.6 Indian Ocean, and 2016/11/13 M7.8 Kaikoura earthquakes. Their studies also found possible dynamic triggering on broadband station SBA located on Ross Island. Here we conduct a systematic search for remotely triggered seismicity at Mt. Erebus using additional permanent stations. Seismometers have been deployed on Mt. Erebus since 1980s, and the permanent ER network is maintained by the Mt. Erebus Volcano Observatory Seismic Network (MEVO). Temporary stations and dense arrays have also been deployed in recent years, providing high-quality seismic data for subsequent body wave and ambient-noise imaging of the volcano (Chaput et al., 2012, 2015, 2016).

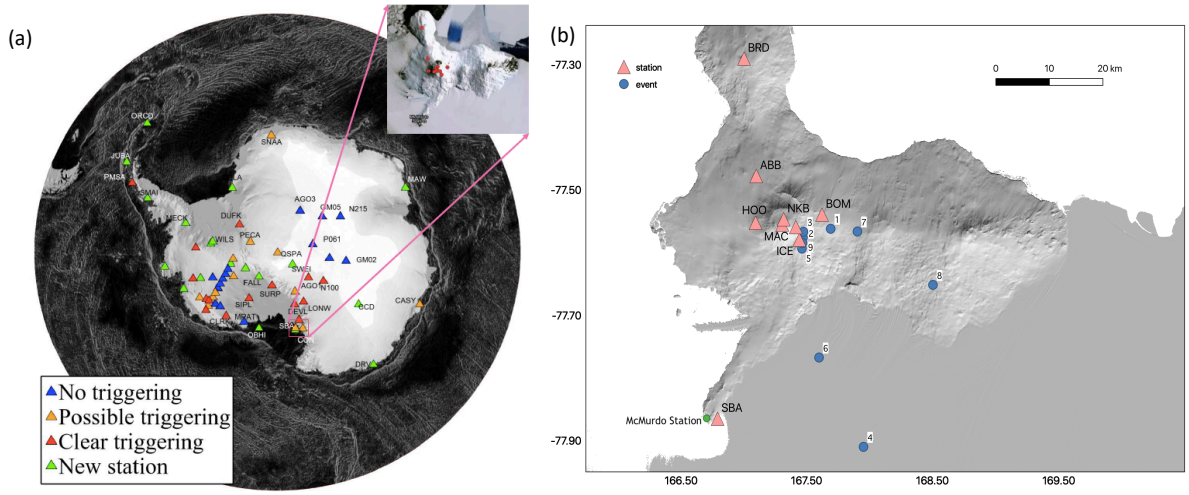

Figure 2.10. (a) Map of stations in previous studies on Antarctica and location of Mt. Erebus. (b) Stations distribution and detected event on Mt. Erebus, and the McMurdo Station.

Here we show additional evidence of triggered seismicity at Mt. Erebus during the 2010 Mw8.8 Maule, Chile earthquake. High-frequency seismic signals are recorded by multiple stations during the short-period Rayleigh waves of the Maule mainshock, suggesting that they are likely driven by dilatational stress perturbations (Figure 2.11). This behavior is similar to recent observations of triggered icequakes at other stations in Antarctica during the Chile mainshock (Peng et al., 2014). However, based on visual inspections alone, it is not clear whether those triggered events at Mt. Erebus are associated with magma, tectonic, or ice movements. We locate those remotely triggered events with manually picked arrival times and a grid-search method across the ER network (Figure 2.12). The resulting locations of these triggered events are shown in Figure 2.10.

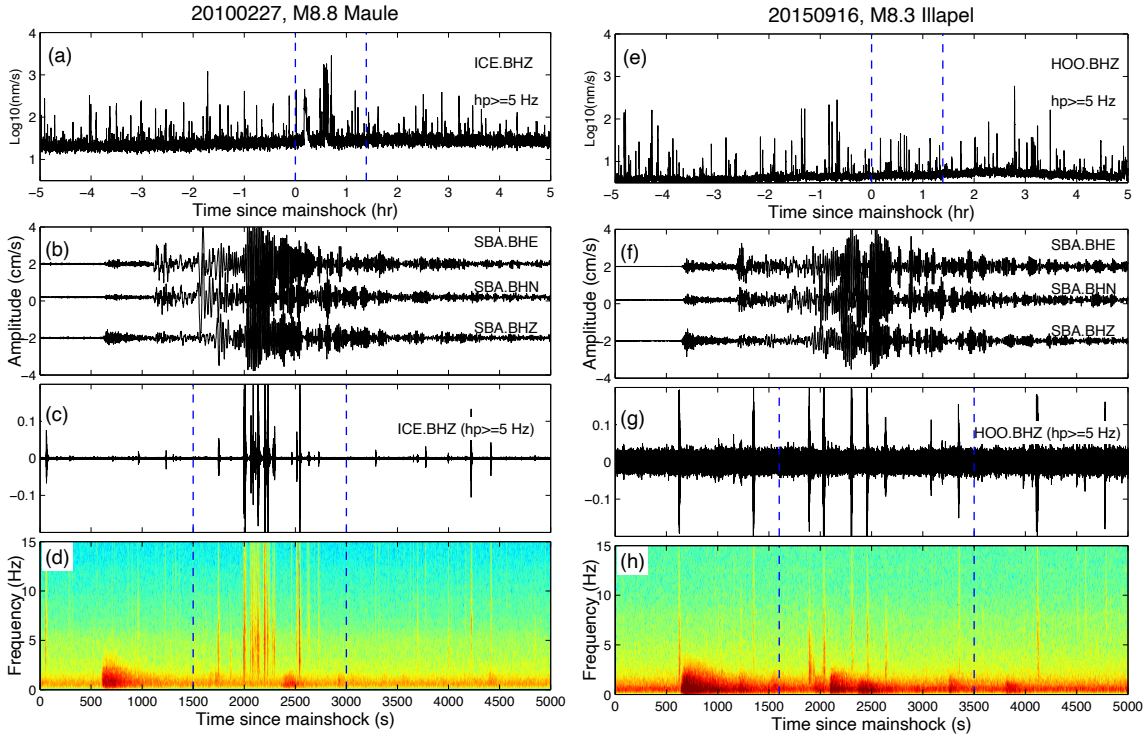

Figure 2.11. (a) High-pass filtered envelope function 5 hours before/after the 2010 M8.8 Maule mainshock in station ICE. (b) Unfiltered waveform in SBA during 0~5000s. (c) High-pass filtered waveform and (d) spectrogram of the vertical component. (f) - (i) Results for the 2015 M8.3 Illapel, Chile earthquake.

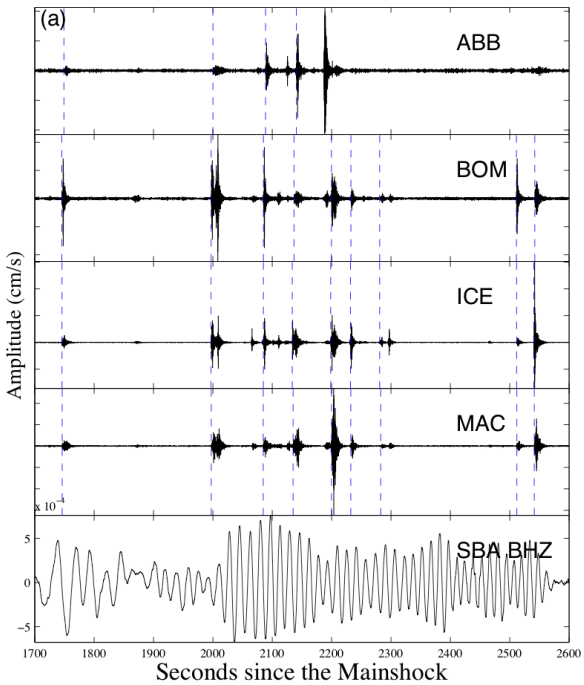

Figure 2.12. High pass filtered waveforms of four stations during the Maule surface waves. Blue dashed lines mark manually picked arrivals, which are subsequently located using a grid-search method. The bottom trace is unfiltered waveform of station SBA.

Similar to the analysis procedure at Changbaishan volcano (section 2.3.2), we conduct a systematic study of dynamic triggering on Mt. Erebus. We select 56 M>5.5 global earthquakes with predicted dynamic stress changes larger than 1 kPa, and retrieve continuous data 1 day before/after each earthquake. Then we run STA/LTA on bandpass (2-16 Hz) filtered waveform, and compute the β-statistic value for significance of triggering. For events with β value larger than 1, we apply the matched-filter detection to the continuous waveform and visual inspection to further confirm evidence of triggering. The templates used for matched-filter are the detected/located events during the surface waves of the 2010 M8.8 Maule earthquake. The high-pass filtered envelope, waveforms and spectrograms of 2015 M8.3 Illapel earthquake are in Figure 2.11. However, the persistent high-frequency signal before and after the mainshock makes it difficult to conclude that these events are dynamically triggered. We also find other events with possible dynamically triggered signals during the surface waves. About 3-4 stations record high-frequency signals during surface waves for the 2012 M8.6 Indian Ocean event, and 2 stations show high-frequency signals after S wave of the 2004 M9.2 earthquake (Figure 2.13). However, the persistent high-frequency background noises make it difficult to evaluate the significance of seismicity increase and determine whether they can be robustly considered as triggered seismicity.

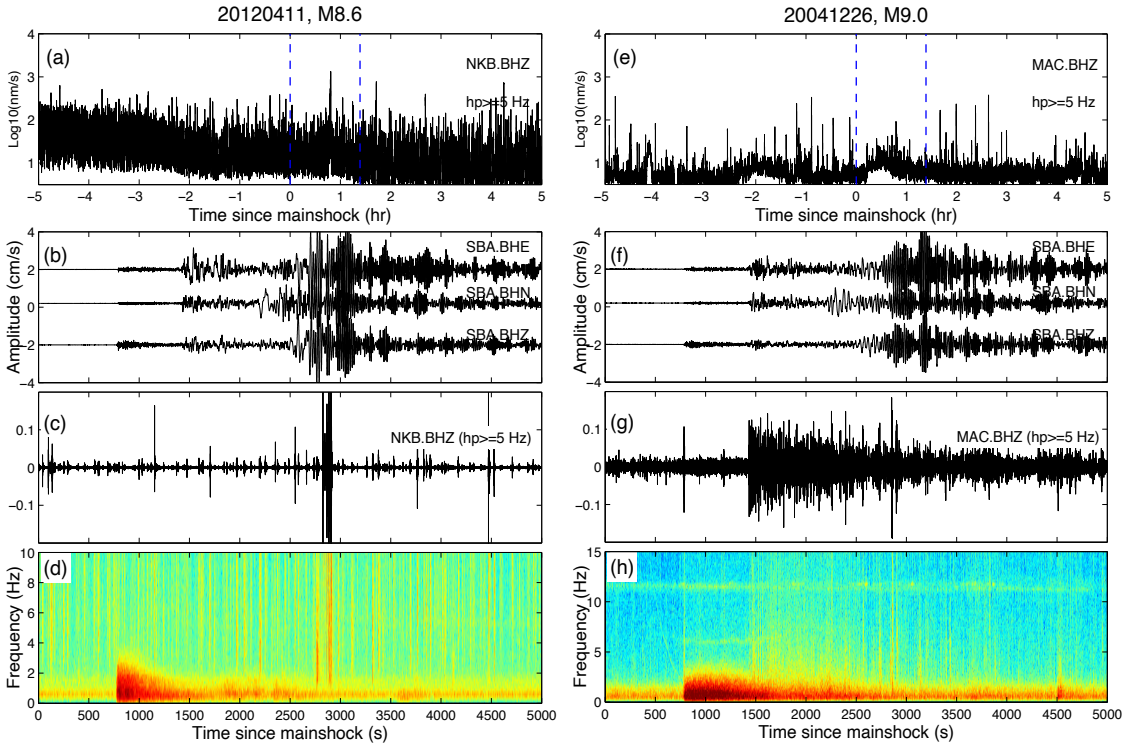

Figure 2.13. (a) High-pass filtered envelope function 5 hours before/after 2012 M8.6 Indian Ocean earthquake in station NKB. (b) Unfiltered waveform in SBA during 0~5000s. (c) High-pass filtered waveform and (d) spectrogram of the vertical component. (f) - (i) Results for 2004 M9.0 Sumatra earthquake.

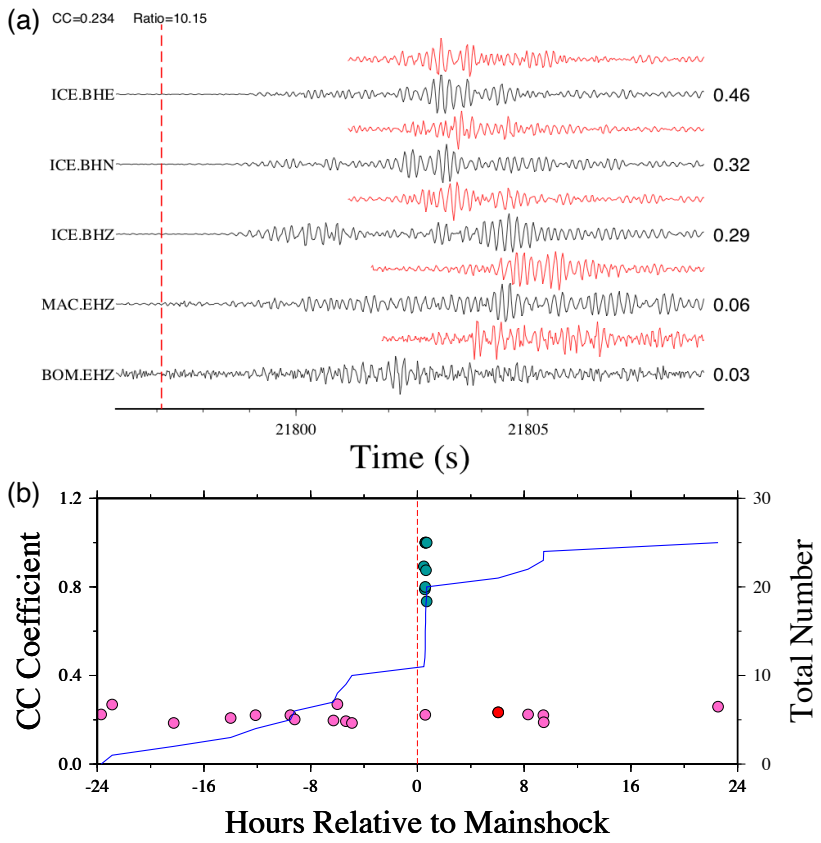

Figure 2.14. (a) Example of a new event detected by template events during the surface wave of 2010 M8.8 earthquake. (b) Catalog of detected events 1 day before/after the 2010 M8.8 mainshock. The green circles are templates and purple ones are detected events, the event shown in (a) is the red circle.

Figure 2.14 shows example of an event detected by the template events during the surface wave of 2010 M8.8 Maule earthquake. This event occurred at 21797 seconds after the origin time of the 2010 M8.8 earthquake and has a mean cross-correlation coefficient of 0.234 with the template. The events detected 1 day before/after the 2010 M8.8 mainshock have relatively low cross-correlation coefficient, suggesting that the events during surface waves are not very similar compared to other times before and after the mainshock. The detections around other 13 mainshocks also show no clear evidence of seismicity changes, suggesting that the triggered seismicity during the Maule

earthquake is different with the background seismicity and during other distant earthquakes.

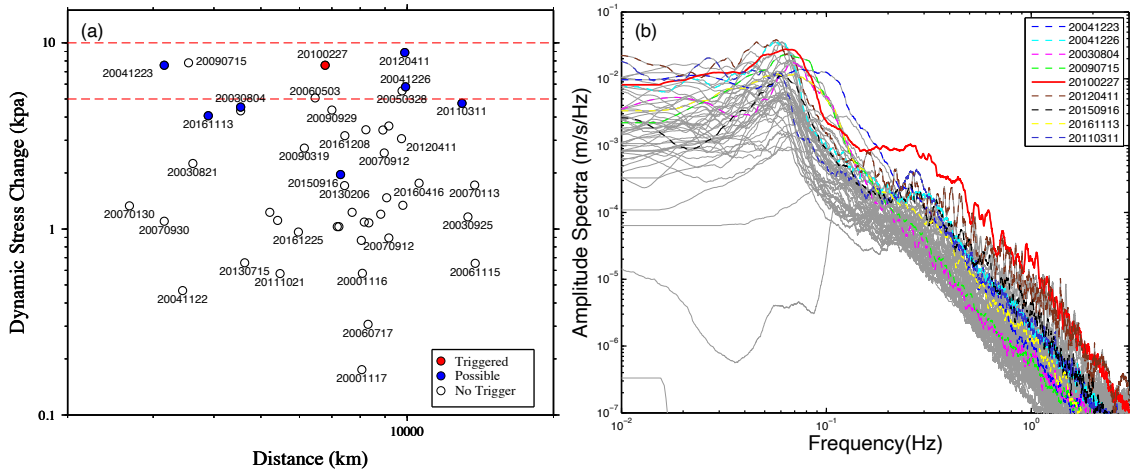

Figure 2.15. (a) Estimated dynamic stress change from PGV on station SBA and distance for all the studies remote earthquakes. The remote earthquakes with clear evidence of triggering and potential triggering are marked as red and yellow circles. (b) Amplitude spectra for all the earthquakes.

After examination of 56 target earthquakes for dynamic triggering at Mt. Erebus, the only event with clear evidence of dynamic triggering is the 2010 M8.8 Maule earthquake. We then compare the PGV and corresponding peak dynamic stress changes of all distant earthquakes. The largest dynamic stress change in Mt. Erebus is around 9 kPa, which is smaller than tens of kPa in Changbaishan volcano. This might be the reason that there is only one confirmed case (the Maule earthquake) of dynamic triggering. On the other hand, all earthquakes with dynamic stress higher than 6 kPa seems to have clear or possible evidence of dynamic triggering, consistent with dynamic triggering threshold between 5-10 kPa from previous studies (Hill and Prejean, 2015). Based on the amplitude spectra, the 2010 M8.8 Maule earthquake has higher energy in shorter-period (0.1 Hz – 1 Hz). This is likely because the triggered events are shallow icequakes and are more sensitive to large-amplitude short-period seismic waves. The seismograms of triggered

events during 2010 M8.8 Maule earthquake are similar to recorded icequakes, with impulsive or semi-impulsive onsets in stations within 1 km, and become emergent at distant stations (Knox, 2011). In addition, there is lack of volcano-tectonic seismic sources on Mt. Erebus, which is likely caused by an open conduit and ongoing degassing (e.g., Aster et al., 2003; Rowe et al., 2010). Based on these background information, we argue that the triggered events around Mt. Erebus by surface wave of 2010 M8.8 Maule earthquake are likely shallow stick-slip icequakes. Further observation of large distant earthquakes capable of generating higher dynamic stress changes can provide more insight into how icequakes and volcanic source events interact with external perturbations.

CHAPTER 3. CHARACTERISTIC OF SEISMICITY IN SALTON SEA GEOTHERMAL FIELD WITH MATCHED-FILTER TECHNIQUE

With an improved catalog from WMFT, I study the characteristic of seismicity in the Salton Sea Geothermal Field (SSGF), one of the largest geothermal fields in California. The study focuses on dynamic triggering of seismicity in SSGF following regional and distant earthquakes. In addition, the relationship between seismicity and geothermal production is also examined.

3.1 Summary

The Salton Sea Geothermal Field (SSGF) is one of the most seismically active and geothermally productive fields in California. Here we present a systematic investigation of seismicity change in SSGF from 2008 to 2014 utilizing the Calenergy Borehole Network (EN) and a waveform matched-filter catalog. We apply a recently developed GPU-based waveform matched-filter technique (WMFT) to obtain a more complete catalog and analyze the seismicity rate changes in SSGF, for both long-term and short-term changes in rates following regional and large teleseismic earthquakes. We find triggered seismicity in SSGF following several regional M6-7 earthquakes. However M>8.0 teleseismic earthquakes did not trigger significant seismicity rate change in SSGF, suggesting that short-period surface waves are more efficient in triggering seismicity in the SSGF than long-period surface waves. We also characterize the correlation between seismicity and geothermal production rates, and the temporal and spatial variation of Guttenberg-Richter b-values inside and outside SSGF with the newly-detected catalog.

3.2 Introduction

Geothermal resource is considered as a promising renewable energy to reduce the green house warning effects from burning fossil fuels. However, in the past two decades several M>3.0 earthquakes occurred very close to geothermal fields, such as the 2017 Mw5.4 Pohang earthquake, raising concern of induced earthquakes by geothermal productions (Ellsworth et al., 2019; Kim et al., 2018). The Salton Sea Geothermal Field (SSGF) is located in the southern shorelines of Salton Sea in Southern California, which is a shallow saline lake within the Salton Trough. It is bounded by the Southern San Andreas Fault to the NE, and the Imperial Fault, and Cerro Prieto Fault to the SW (Figure 3.1). The high variation of temperature in SSGF is likely caused by magmatic intrusion due to the rifting process along the Salton Trough (Younker et al., 1982). The Salton Trough is seismically active with numerous earthquake swarms, driven by aseismic creep and fluid diffusion (Lohman and McGuire, 2007; Chen and Shearer, 2011).

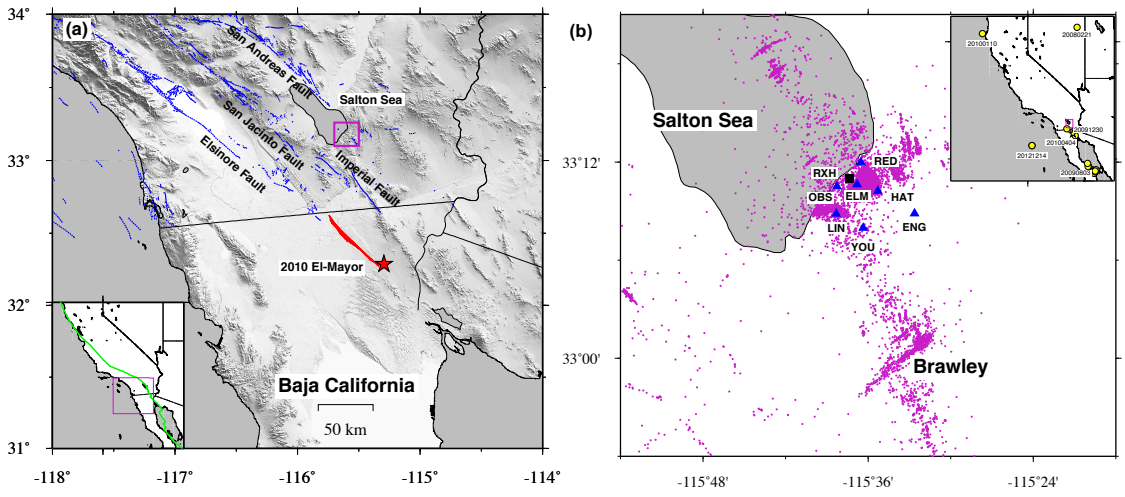

Figure 3.1. (a) Salton Sea Geothermal Field and surrounding tectonic background. (b) Template events and EN stations (blue triangles), the RXH station is broadband in Southern California (CI) network and is used for supplementary check of the waveforms. The yellow circles and star in the inset marks selected regional target mainshocks.

Geothermal fields in California are highly sensitive to external stress perturbations such as dynamic stresses caused by passing surface waves of large earthquakes (Gomberg and Davis, 1996; Brodsky, 2006; Aiken and Peng, 2014). Triggered seismicity in SSGF has been found after several M>7 earthquakes, including the 1999 M7.1 Hector Mine Earthquake and 2010 M7.2 El Mayor-Cucapah Earthquake (Hough and Kanamori, 2002; Meng and Peng, 2014; Castro et al., 2017). Peng et al. (2017) and Taira et al. (2018) observed seismic velocity reduction in SSGF after local and regional earthquakes, likely caused by dynamic stress transients, as well as long-term seismicity velocity increase due to poroelastic contraction during the geothermal production. Brodsky and Lajoie (2013) also reported temporal correlation between background seismicity rate and net production volumn from 1982 to 2013. Spatial correlation between seismicity and injection wells has also been found in the SSGF (Chen and Shearer, 2011; Cheng and Chen, 2018).

Detailed analysis of spatial and temporal changes of seismicity in SSGF can help to better understand its interaction with teleseismic earthquakes and anthropogenic activities, and thus the mechanisms of earthquake triggering and induced earthquakes. Many previous studies on seismicity changes were based on regional or global earthquake catalogs (Hill et al., 1993; Zhang et al., 2017), or manually picked earthquakes (Gomberg et al., 2004; Prejean et al., 2004; Aiken and Peng, 2014). Recently waveform-matched filter technique (WMFT) has been widely used in detecting missing earthquakes, such as aftershocks/foreshocks, triggered earthquakes/tremors, as well as hidden small-magnitude earthquakes in a seismically active region (i.e., Aiken et al., 2016; Shelly et al., 2017; Ross et al., 2019). Several recent studies have utilized

earthquakes detected by matched filter technique to study remote earthquake triggering (van der Elst et al., 2013; Wang et al., 2015; Yao et al., 2015; Johnson and Burgmann, 2016). Compared to manual picking, the WMFT provides a complete and consistent catalog to look into triggering around multiple target earthquakes.

For example, Meng and Peng (2014) examined physical mechanisms of triggered seismicity in SSGF with a GPU-based WMFT applied to ~150 days around the 2010 M7.2 El-Mayor Cucapa earthquake. They found that dynamic triggering played the most important role in triggering microseismicity at the SSGF (and other regions in Southern California) immediately following the mainshock. However, in the long term (i.e., a few months after the mainshock), the seismicity changes in SSGF and elsewhere in Southern California are mostly controlled by static stress changes from the El-Mayor Cucapa mainshock. Similar conclusions are drawn by Ross et al. (2019), which applied a WMFT technique to 10-years of continuous waveforms in Southern California.

Meng and Peng (2014) utilized seismic data recorded by the 7-station Calenergy Borehole (EN) Seismic Network located within the SSGF. However, they only detected microseismicity within ~150 days of the 2010 M7.2 mainshock. The work done by Ross et al. (2019) covers a much longer period (2009-2018) in Southern California, but they only used the regional surface stations. Here we apply a GPU-based WMFT (Meng et al. 2012) to the seismic data recorded by the Borehole Seismic Network between 2008 and 2014, when the continuous data is openly available. With a more complete earthquake catalog, we systematically analyze seismicity change after 40 M>5.5 earthquakes at local-regional distances (50-1000 km) and remote distances (> 1000 km) that are capable of triggering seismicity in SSGF. We also manually examine high-frequency waveforms

at selected surface stations outside the study time window for additional evidence of instantaneous dynamic triggering. Finally, we compare the long-term seismicity rate change with geothermal fluid injection/extraction rates, and characterize the variation of Guttenberg-Richter *b*-values both inside and outside the geothermal field in order to better understand long-term evolution of seismicity patterns and the relationship with geothermal power productions.

3.3 Data and Method

As mentioned before, the seismic data used in this study is from the Calenergy Borehole Network (EN), which includes 7 borehole stations and the continuous data is open to public from 2008 to 2014 (Figure 3.1). We use 8900 events from the relocated catalog during 2007-2014 as templates for detection (SCEDC (2013): Southern California Earthquake Center; Hauksson et al., 2011). We first bandpass filter template and continuous waveforms between 5-20 Hz. We choose this frequency range because the borehole sensor has a corner frequency of 5 Hz. In addition, cultural and industrial noises are stronger at frequencies higher than 20 Hz. The template time window is 1 sec before and 4 sec after the analyst-picked P arrival for vertical component and S arrival for horizontal components. All three channels of templates are cross-correlated with continuous waveforms at each data point, and then the cross-correlation (CC) functions of all channels are shifted back to the origin times of templates and then stacked and normalized (Figure 3.2). Detection threshold is set above 20 times of the median absolute deviation (MAD) of the daily trace together with the mean CC value above 0.3. We use a relatively higher threshold than other recent studies (e.g., Meng and Peng, 2014; Ross et al., 2019), mainly because it can help to remove potential false detections caused by

aftershocks of M>6 earthquakes within 100 km (e.g., Meng et al., 2013; Meng and Peng, 2014). In addition, a relatively high CC threshold ensures that the newly detected events are spatially close to the template event.

The magnitude of detected event is estimated based on the magnitude of template with highest CC value: $M_d = M_t + \log(R)$, where R is the median of maximum amplitude ratio for all the channels (Peng and Zhao, 2009). Newly detected events are assigned the same location as the best matching template. We did not apply any magnitude calibration and relocation methods as was done in recent studies (Shelly et al., 2016; Chen et al., 2018; Ross et al., 2019; Yao et al., 2020), mainly because the locations and magnitudes in the relocated catalog used as template are already well-resolved. In addition, we use a relatively high CC threshold as compared with these studies, which ensures that the newly detected and template events are spatially close to each other.

Figure 3.2 shows a comparison of cumulative frequency magnitude distribution for the Matched-Filter Detected (MFD) catalog in this study (with a threshold of 20× MAD), the Quake Template Matching (QTM) catalog (with a threshold of 12×MAD) from Ross et al. (2019) and the relocated catalog for Southern California Seismic Network (SCSN) from Hauksson et al. (2011). The total number of events is 101035 in the MFD catalog in region within the rectangular grid (latitude range [33.12°, 33.22°], [−115.67°, −115.53°]), which is 3 times and 15 times of events listed in the QTM and SCSN catalogs, respectively. This is mainly because the latter two catalogs were based on waveforms/phases recorded by regional surface stations, while the catalog in this study is detected based on local short-period borehole recordings. The corresponding magnitude of completeness (*Mc*) as determined by the simple maximum curvature

method (Wiemer, 2001) shows a clear reduction from *Mc* = 1 and 0.5 for the SCSN and QTM catalogs to *Mc* = –0.5 for catalog obtained in this study.

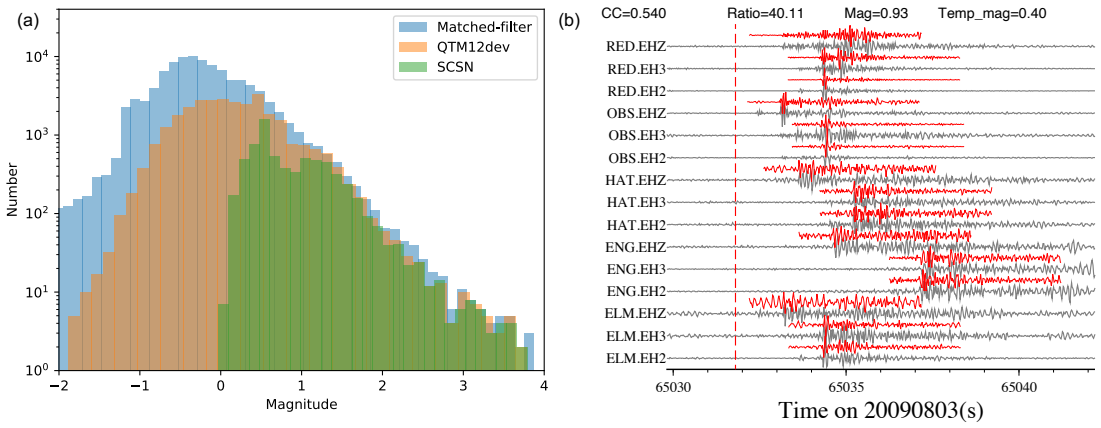

Figure 3.2. (a) Magnitude distribution for three catalogs. Three catalogs are: matched-filter detected catalog in this study, the QTM catalog from Ross et al. (2019) and the relocated catalog from Hauksson et al. (2013). (b) Example of a detected event on 08/03/2009 with cross-correlation coefficient 0.54.

3.4 Seismicity change analysis

3.4.1 Search for triggered seismicity increase

To search for dynamically triggered seismicity increase, we first select moderate to large earthquakes (M>5.5) during 2008-2014 with predicted dynamic stresses larger than 1 kPa on station RED in the SSGF. We follow the equations for computing far-field dynamic stresses in van der Elst and Brodsky (2010):

$$\log_{10} A_{20} = M_s - 1.66 \log_{10} \Delta - 2 \tag{6}$$

where A_{20} (micrometers) is the peak dynamic strain of long-period (20s) surface waves, and Δ is in epicentral distance in degrees. Then the displacement A_{20} is converted to velocity for the 20s waves by the approximation $V \approx \frac{2\pi A_{20}}{T}$ (van der Elst and Brodsky, 2010; Aki and Richards, 2002).

After selecting 40 target earthquakes, we compare the seismicity rate in SSGF before and after their original time (Table 1). We compute β-statistic values (i.e. Matthews and Reasenberg, 1988; Aron and Hardebeck, 2009) as an indicator of dynamic triggering. The β-statistic value above 2 indicates a significant seismicity rate increase (Hill and Prejean, 2015; Aiken and Peng, 2014).

Table 1. Information of all the target earthquakes.

Date	Magnitude	Longitude	Latitude	Depth(km)	Distance (km)
2010-04-04	7.2	-115.30	32.29	10.00	103
2010-06-15	5.7	-115.92	32.70	5.41	60
2009-12-30	5.8	-115.19	32.46	6.00	88
2012-04-12	7.0	-113.10	28.70	13.00	551
2009-08-03	6.9	-112.90	29.04	10.00	526
2010-04-04	5.7	-115.05	32.10	10.00	130
2012-12-14	6.4	-119.56	31.21	11.30	431
2012-12-14	6.3	-119.56	31.21	11.00	431
2009-08-03	6.2	-113.73	29.31	10.00	464
2011-03-11	9.1	142.37	38.30	29.00	8732
2012-04-12	6.0	-113.03	28.84	9.00	540
2009-08-05	5.8	-113.79	29.61	10.00	431
2010-02-27	8.8	-72.90	-36.12	22.90	8859
2012-10-28	7.8	-132.10	52.79	14.00	2547
2012-10-28	7.7	-131.93	52.77	5.00	2538
2009-08-03	5.5	-113.00	28.90	10.00	535
2014-04-01	8.2	-70.78	-19.61	25.00	7531
2013-01-05	7.5	-134.65	55.39	10.00	2879
2012-03-20	7.4	-98.23	16.49	20.00	2540
2014-03-10	6.8	-125.13	40.83	16.64	1198
2013-10-19	6.6	-110.32	26.09	9.45	937
2012-04-11	8.6	93.06	2.33	20.00	15066
2010-10-21	6.7	-109.16	24.70	13.00	1130
2014-04-18	7.2	-100.96	17.40	24.00	2280
2012-09-05	7.6	-85.31	10.10	35.00	4015
2009-09-29	8.1	-172.09	-15.49	18.00	8053
2012-11-07	7.4	-91.85	13.96	24.00	3209
2012-08-27	7.4	-88.59	12.14	28.00	3601
2009-05-28	7.3	-86.22	16.73	19.00	3461
2010-01-10	6.5	-124.69	40.65	29.33	1157
2013-02-06	8.0	165.14	-10.74	28.70	9670

2011-03-11	7.9	141.11	36.28	42.60	8949
2012-09-25	6.3	-110.17	24.67	10.00	1081
2012-04-11	8.2	92.46	0.80	25.10	15242
2014-04-03	7.7	-70.47	-20.57	35.00	7633
2012-04-11	6.7	-102.69	18.23	20.00	2098
2009-10-07	7.8	166.38	-12.52	35.00	9670
2011-06-24	7.3	-171.84	52.05	52.00	4920
2011-03-11	7.7	144.59	38.06	18.60	8583
2008-05-12	7.9	103.32	31.00	19.00	11822

For delayed triggering, we investigate two triggering windows: short-term (1 day) and long-term (30 days). In addition to computing β-statistic values for both time windows, we also apply a recently developed empirical statistical method (Pankow and Kilb, 2020) to further confirm the triggering effect. Specifically, we apply a sliding time window of 0.1 day from 2008-01-01 to 2013-12-31, resulting in 21902 1-day time windows. Next, the number of earthquakes N in each window is counted. Following Pankow and Kilb (2020), we use 90th percentile of all Ns as the threshold N_{thres} for triggering. If the number of events in the 1-day window after a target mainshock is higher than N_{thres} and the number of events before the mainshock N_{pre}, this mainshock is considered as potentially triggering seismicity for the 1-day time window.

3.4.1.1 Instantaneous triggering

Seismicity triggered during surface waves of the target earthquakes are known as instantaneous triggering (e.g., Prejean et al., 2004; Hill and Prejean, 2015). Here we define the triggering window as the time period corresponding to an apparent phase velocity of 2-5 km/s plus 100 s to the end. Because some events are less than 100 km away from the SSGF (and hence have a relatively short time window of < 33 s), we add 100s to the triggering window to ensure that the time window is long enough for any statistical significance. The time window before target earthquake is set to be 1 day.

Out of the 40 events analyzed, two regional earthquakes showed clear evidence of instantaneous triggering: the 2009/08/03 Mw 6.9 earthquake in Baja California, and the 2010/04/04 Mw 7.2 El Mayor-Cucapah earthquake (Figure 3.3). The corresponding β-values (with events larger than the Mc=0) are 2.05 and 25.96 for the 2009/08/03 Mw 6.9 and the 2010/04/04 Mw 7.2 earthquakes, respectively. On the other hand, large distant earthquakes such as the 2010/02/27 Mw8.8 Maule, Chile earthquake and the 2011/03/11 Mw9.1 Tohoku-Oki, Japan earthquake likely triggered a few earthquakes with M<0 (Figure 3.4). When the Mc is set as -0.5, the 2009/12/30 Mw 5.8 Baja California, 2010 Chile and 2011 Tohoku earthquakes have β values of 6.1, 2.7, and 3.8, respectively. We consider the events that showed dynamic triggering by both methods with Mc=-0.5 as possible triggering. For all the events with possible dynamic triggering, we estimate the seismicity rate during surface wave by number of events per hour, and the 2009/08/03 M6.9, 2009/12/30 M5.8 and 2010/04/04 earthquakes have much higher seismicity rates than those for other events (Table 2).

Table 2. Seismicity rate during surface waves of earthquakes with instantaneous triggering. Other earthquakes with no event during surface waves (rate=0) are not displayed in the table.

Event time	Seismicity rate during surface waves (number/hour)
2009-08-03 M6.9	55.91
2009-12-30 M5.8	21.20
2010-01-10 M6.5	0
2010-02-27 M8.8	5.22
2010-04-04 M7.2	55.12
2011-03-11 M9.1	3.97
1999-10-16 M7.1	23.9
2003-12-22 M6.5	39.6
2019-07-04 M6.4	0
2019-07-05 M7.1	17.8

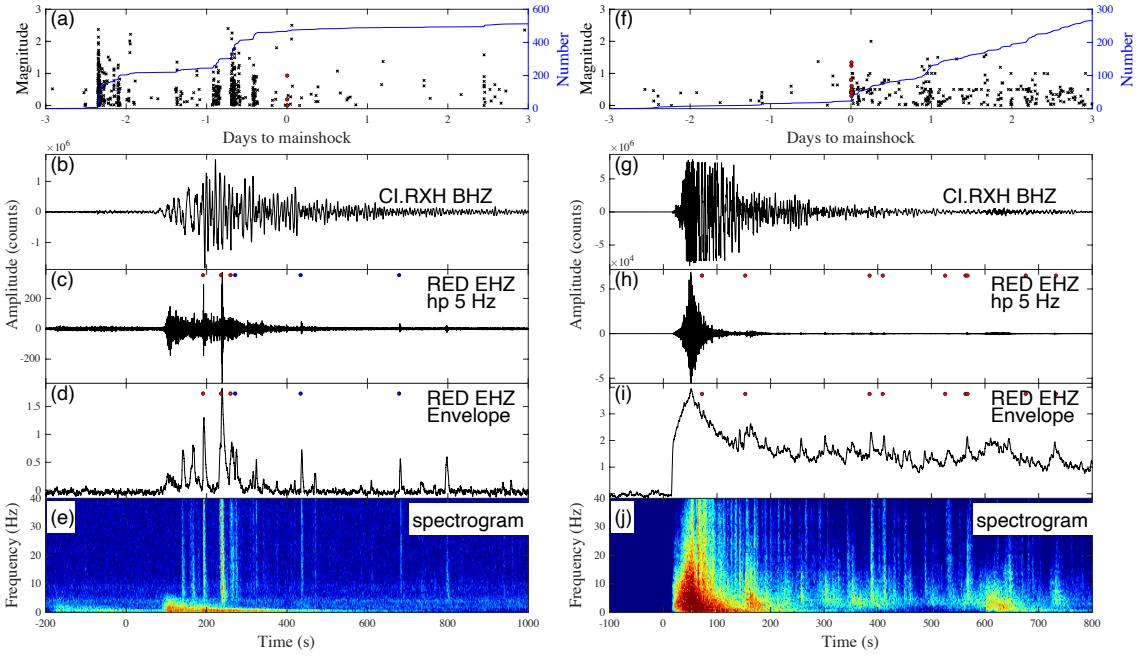

Figure 3.3. (a) Detected events 3 days before/after the 08/03/2009 M6.9 Baja California Earthquake, red circles are events within 600s of the mainshock, blue circles are events with M<0. (b) Waveform in broadband station RXH. (c) High-pass 5 Hz waveform on station RED, (d) envelope of (c), (e) spectrogram of (c). (f)-(j) Same from (a)-(e) for the 04/04/2010 M7.2 El Mayor-Cucapah Earthquake.

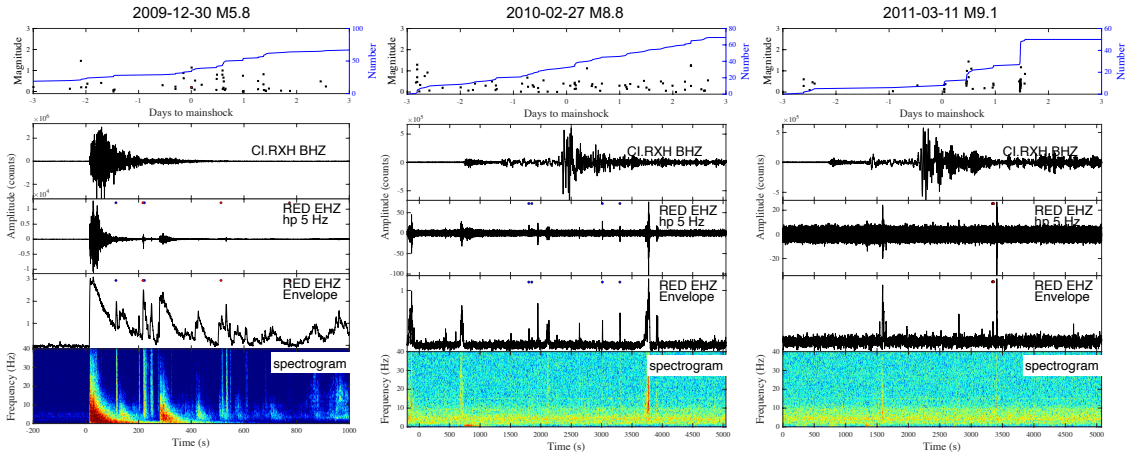

Figure 3.4. Waveform and spectrogram of earthquakes with possible dynamic triggering during surface waves.

3.4.1.2 Short-term and long-term delayed triggering

As mentioned before, we consider triggered seismicity 1 day after target earthquakes as short-term delayed triggering, and 30 days after as long-term triggering. In addition to the β-statistic, we apply the empirical statistical method (Pankow and Kilb, 2020) to the 6-year catalog and select time windows that are above the 90% of entire distribution. The earthquakes that are considered to trigger seismicity after 1 day in Salton Sea by both β-statistic and the empirical statistical method are shown in Table 3. There are 7 triggering earthquakes detected by the β-statistic threshold ($\beta>2$) and 3 out of them are also detected by empirical statistical method. The cumulative numbers of earthquakes in Salton Sea after some of the events in Table 3 are shown Figure 3.5. The 04/04/2010 M7.2 El Mayor-Cucapah Earthquake triggered a clear instantaneous increase of local seismicity, while the local seismicity after 01/10/2010 M6.5 and 02/06/2013 M8.0 earthquake showed step-wise increase with a few hours of time delay.

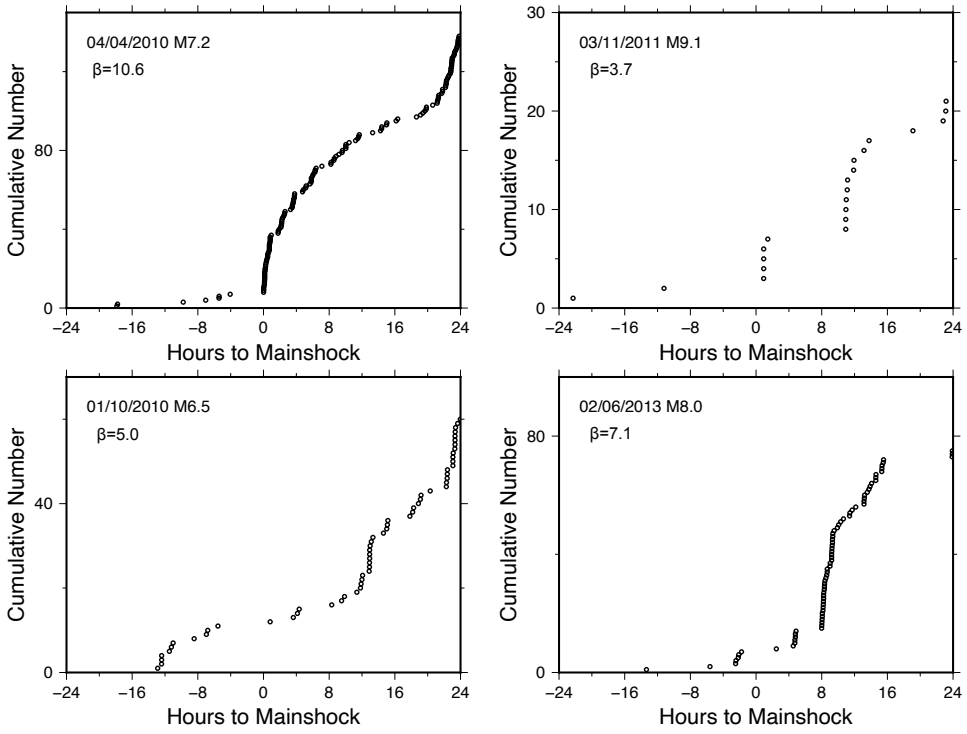

Figure 3.5. Cumulative number of earthquakes of M>0 in Salton Sea after four earthquakes in Table 3.

We apply both the β-statistic and the empirical statistical method to the 30-day windows for long-term delayed triggering. For the empirical statistical method, the sliding window length is 3-day and the total number of 30-day time window is 7205. There are 11 possible triggering earthquakes detected by the β-statistic and 3 out of them are also detected by empirical statistical method (Table 3). Table S3 shows the results from the same analysis if we use Mc=–0.5. The 2010-02-27 M8.8 Maule earthquake is considered as a triggering event for 1-day window, and the 2011-03-11 M9.1 Tohoku earthquake for 30-day window if the Mc=–0.5.

Table 3. Information of the events that triggers seismicity indicated by β-statistic and empirical method. The triggering confirmed by both methods are marked with bold text. Only the events that are either above β-value or empirical event number threshold are displayed in the table.

Event time	1 day		30 day	
	β-statistic	Empirical Method	β-statistic	Empirical Method
2008-02-21 M5.9	Yes	No	No	Yes
2008-05-12 M7.9	No	No	Yes	No
2009-10-07 M7.8	No	Yes	No	No
2009-08-05 M5.8	Yes	No	No	No
2009-09-29 M8.1	No	No	Yes	No
2009-12-30 M5.8	Yes	No	**Yes**	**Yes**
2010-01-10 M6.5	**Yes**	**Yes**	**Yes**	**Yes**
2010-04-04 M7.2	**Yes**	**Yes**	**Yes**	**Yes**
2011-03-11 M9.1	Yes	No	Yes	No
2011-06-24 M7.3	No	No	Yes	No
2012-08-27 M7.4	No	Yes	Yes	No
2012-10-28 M7.8	No	No	Yes	No
2012-11-07 M7.4	No	No	Yes	No
2013-02-06 M8.0	Yes	Yes	Yes	No

Table 4. Results when Mc=-0.5.

Event time	1 day		30 day	
	β-statistic	Empirical Method	β-statistic	Empirical Method
2008-02-21 M5.9	Yes	No	No	No
2008-05-12 M7.9	No	No	Yes	No
2009-08-05 M5.8	Yes	No	No	No
2009-09-29 M8.1	No	No	Yes	No
2009-10-07 M7.8	No	Yes	No	No
2009-12-30 M5.8	Yes	No	Yes	Yes
2010-01-10 M6.5	**Yes**	**Yes**	Yes	Yes
2010-02-27 M8.8	**Yes**	**Yes**	No	No
2010-04-04 M7.2	**Yes**	**Yes**	Yes	No
2011-03-11 M9.1	Yes	No	**Yes**	**Yes**
2011-06-24 M7.3	Yes	No	No	No
2012-04-11 M8.6	Yes	No	No	No
2012-08-27 M7.4	No	No	Yes	No
2012-11-07 M7.4	No	No	Yes	No
2013-02-06 M8.0	**Yes**	**Yes**	Yes	No

3.4.1.3 Background seismicity increase

To further remove the influence of aftershocks and earthquake swarms, we apply a stochastic declustering method based on space-time epidemic-type aftershock sequence (ETAS) model to the catalog (Ogata 1998; Zhuang et al, 2002; Zhuang et al, 2004; Zhuang 2005). In the ETAS model, the seismicity rate of event at time *t*, with location (*x*, *y*) and magnitude *M* is,

$$\lambda(t,x,y) = \nu u(x,y) + \sum_{i:t_i<t} \kappa(M_i) g(t-t_i) f(x-x_i, y-y_i, M_i) \tag{7}$$

where $\nu u(x,y)$ is background seismicity rate, $\kappa(M) = Ae^{\alpha(M-M_C)}$ (for $M>Mc$) is the expected number of aftershocks from a mainshock with magnitude M. *g(t)* is the probability density function form of the modified Omori's law:

$$g(t) = \frac{p-1}{c}(1+\frac{t}{c})^{-p}, \quad t>0 \tag{8}$$

where *p* is the aftershock decay rate, *c* is a time constant, and *t* is time since mainshock. $f(x,y,M)$ is model of the spatial probability density function from Zhuang et al. [2005]:

$$f(x,y,M) = \frac{q-1}{\pi D^2 e^{\gamma(M-M_C)}}(1+\frac{X^2+y^2}{D^2 e^{\gamma(M-M_C)}})^{-q} \tag{9}$$

The parameter set $\theta = (\nu, A, \alpha, c, p, D, q, \gamma)$ in the ETAS model are estimated by maximum likelihood in the etas8p program (open available at http://bemlar.ism.ac.jp/zhuang/software.html), and the output also contains background probability, background rate of each event. The probability of event j being a background event is

$$\varphi_j = 1 - \frac{\kappa(M_i) g(t-t_i) f(x-x_i, y-y_i, M_i)}{\lambda(t_j, x_j, y_j)} \tag{10}$$

Here we use 3-month window and higher cutoff magnitude *Mc*=0 to make sure that the catalog is complete and the algorithm could converge well. If we set the *Mc*=–0.5,

the algorithm does not converge. Then we calculate the cumulative background seismicity as: $S(t) = \sum_{t<t_i} \varphi_i$, where φ_i is the background probability of the i_{th} event in the catalog (Meng and Peng, 2014).

As shown in Table 3, the 12/30/2009 M5.8 earthquake likely triggered seismicity increase in the 30-day window, but the cumulative number and background seismicity in Figure 3.6c indicates that the increase of seismicity is not significant until 10 days after this earthquake. Similarly, the 02/21/2008 M5.9, 03/11/2011 M9.1, and 03/06/2013 M8.1 earthquakes were not followed by a significant increase in the background seismicity. In contrast, the 01/10/2010 M6.5 and 04/04/2010 M7.2 earthquakes both have significant increase in background seismicity (Figure 3.6d,e) up to 30 days. For the 08/03/2009 M6.9 Baja California Earthquake, there is a long-term elevation of background seismicity after the declustering procedure (Figure 3.6b), which is likely masked by the swarm activity 1~2 days before the mainshock. Combining results for dynamic triggering (Table 3) and cumulative background seismicity (Figure 3.6), we confirm that the 2009/08/03 M6.9, 2010/01/10 M6.5 and 2010/04/04 M7.2 earthquakes trigger long-term seismicity increases in SSGF.

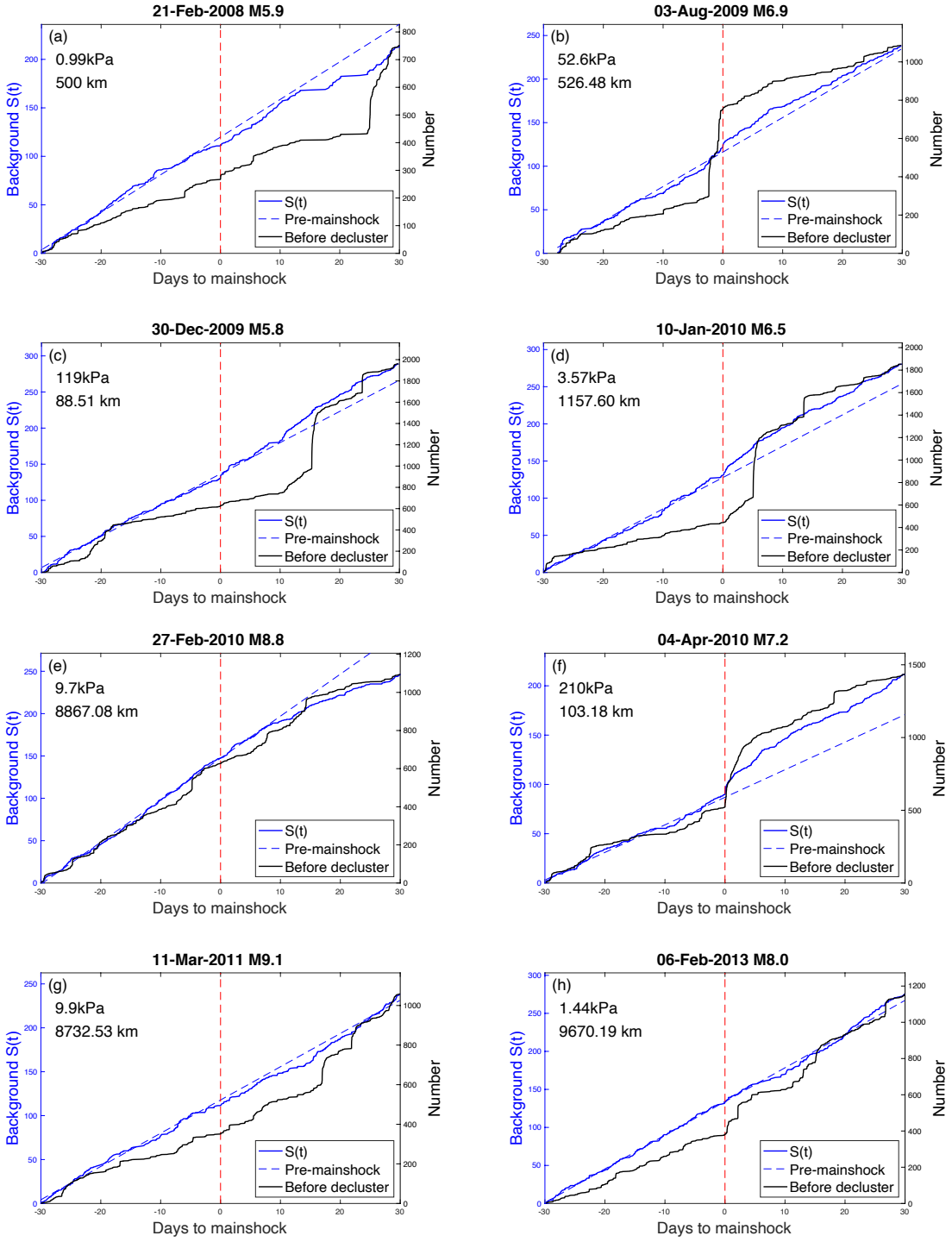

Figure 3.6. Cumulative background seismicity (black line) and cumulative number of earthquakes before decluster (blue line) around the potential triggering earthquakes.

3.4.1.4 Additional evidence for instantaneous triggering

To further augment our database of triggering mainshocks, we examine high-frequency waveforms of additional M>5.5 earthquakes between 1992 and 2008 and 2014-2020 with distances from 100 km to 1000 km, and a few remote M>8.0 earthquakes in Sumatra and Chile (Table 5). During these time periods, the waveforms of EN network are not open to public so we analyze broadband and short-period stations around the SSGF. Before 2004, the nearest broadband station is CI.SSW. During 2008-2014 and 2014-2019, we analyze the broadband station CI.RXH. In addition, the QTM catalog (Ross et al., 2019) lasts from 2008-2017 and the corresponding β-statistic can be used as additional evidence. We found more regional earthquakes that triggered seismicity in SSGF: the 2003 M6.5 San Simeon earthquake (210 km) and 2019 M7.1 Ridgecrest earthquake (320km) and its M6.4 foreshock (Figure 3.7, Figure 3.8). For the 2004 M6.1 Parkfield and 2014 M6.0 Napa earthquake, there is no clear evidence of dynamic triggering on the waveform, and the β-statistic computed from QTM catalog doesn't have increase of seismicity, likely because the triggered dynamic stress changes are small for them. The 2007 M8.4 Sumatra earthquake and M>8 earthquakes during 2014-2016 in Chile did not trigger any local seismicity in SSGF either.

Table 5. Information of M>5.5 earthquakes examined before 2008 and after 2014.

Time	Magnitude	Distance (km)	β-value	Location
1999-10-16	**7.1**	**168**	**31**	**Hector Mine, California**
2002-11-03	7.9	4029	-0.7	Denali, Alaska
2003-12-22	**6.5**	**210**	**10**	**San Simeon, California**
2004-09-28	6.1	525	-0.2	Parkfield, California
2007-09-12	8.4	15035	-0.3	Nias, Indian Ocean
2014-04-01	8.2	7539	-0.5	Iquique, Chile
2014-08-24	6.0	823	-0.2	Napa, California
2015-09-16	8.3	8526	-0.5	Illapel, Chile
2016-03-28	5.5	342	-0.2	Gulf of California

2016-12-25	7.6	9481	-0.3	Chile
2016-12-28	5.6	655	-0.3	Hawthorne, Nevada
2019-07-04	**6.4**	**329**	**3**	**Ridgecrest, California**
2019-07-05	**7.1**	**340**	**17**	**Ridgecrest, California**

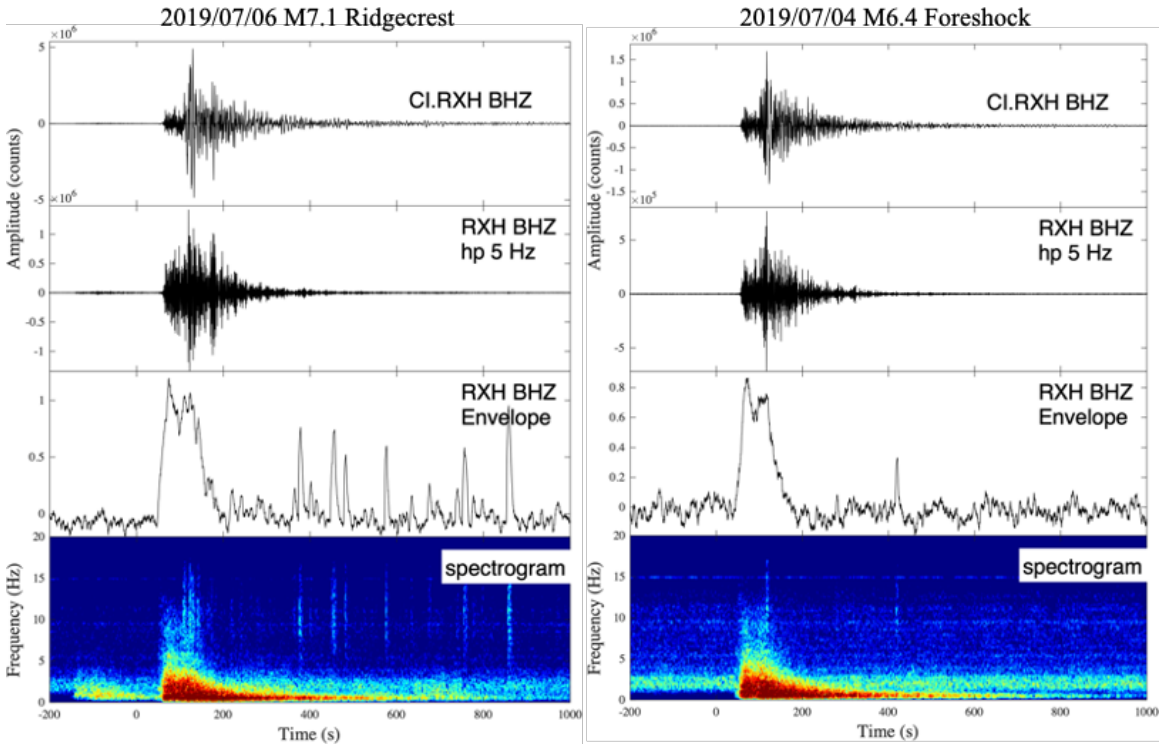

Figure 3.7. Waveform and spectrogram of (a) M7.1 July-06-2019 Rigecrest earthquake and (b) the M6.4 July-04-2019 foreshock.

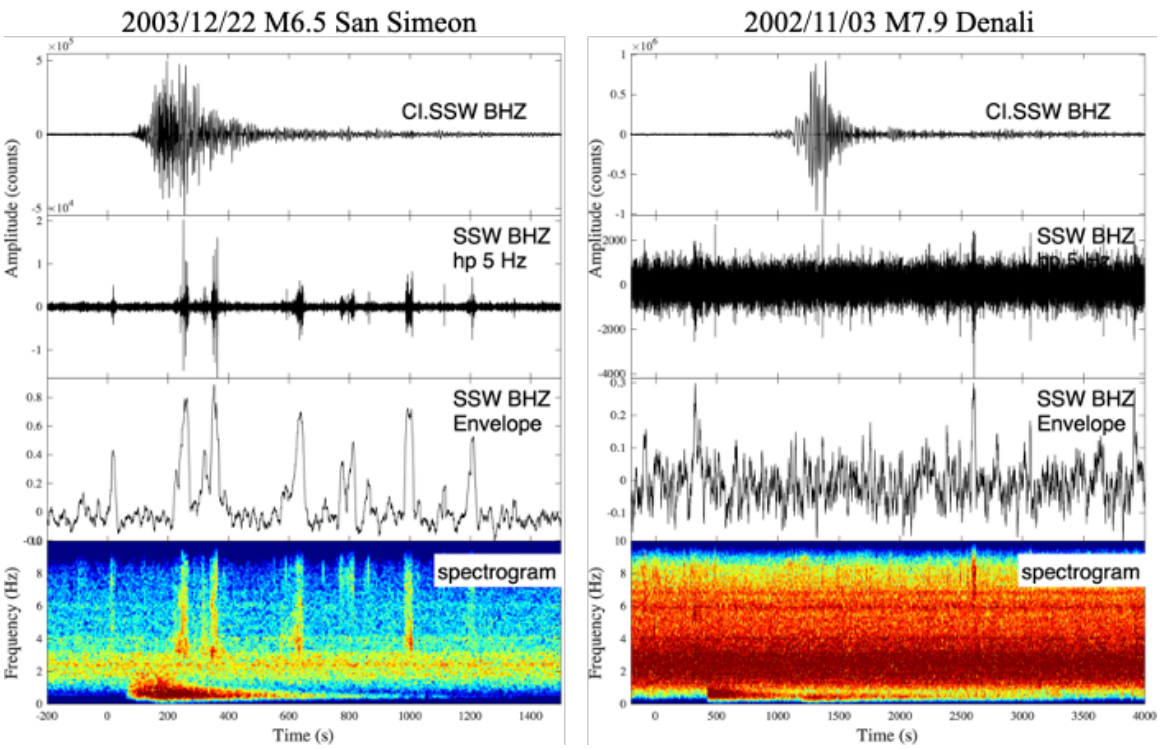

Figure 3.8. Waveform and spectrogram of the M6.5 Dec-22-2003 San Simeon, and M7.9 Nov-03-2002 Denali earthquakes.

3.4.2 Relationship between seismicity and geothermal activities

3.4.2.1 Temporal variation of seismicity

Brodsky and Lajoie (2013) analyzed the seismicity in SSGF from 1987 to 2013, and found that the monthly background seismicity rate is regulated by the geothermal net production rate and injection rate. In this study, we compare the monthly cumulative background seismicity of our stochastic declustered catalog with the production/injection rates from 2008 to 2014. There is no correlation between cumulative background seismicity of event with M>0 and net production rate (R=0.092, Figure 3.9a), while there is significant correlation between background seismicity of M>1.5 events and net production (R=0.604, Figure 3.9d). Based on Figure 3.9, we also observe an increasing trend for background seismicity with M>0 and decreasing trend for M>1.5.

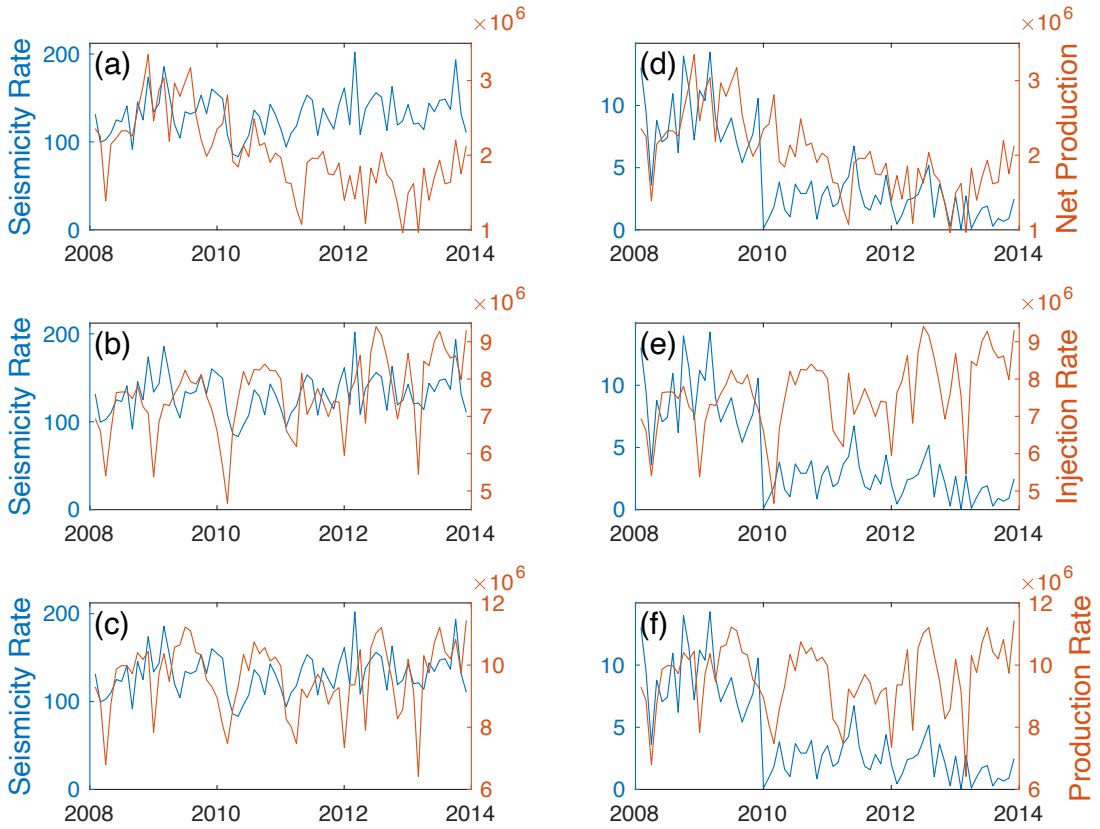

Figure 3.9. Monthly cumulative background seismicity of events with M>0 in Salton Sea compared with (a) net production rate, (b) injection rate and (c) production rate. (d) (e) (f) Same for events with M>1.5.

The cumulative density function (CDF) of all seismicity and background seismicity for events inside and outside SSGF are displayed in Figure 3.10. The events that have nearest lateral distance to injection/production wells less than 3 km are considered inside the geothermal field, and others are considered outside (Cheng and Chen 2017). The seismicity outside SSGF shows step-wise increase for all M>0.5, M>1.5 and M>3.0 events, while only M>3 seismicity inside SSGF have similar increase compared with outside SSGF. The cumulative of background seismicity demonstrates similar gradual increase trends for M>0.5 and M>1.5 both inside and outside SSGF.

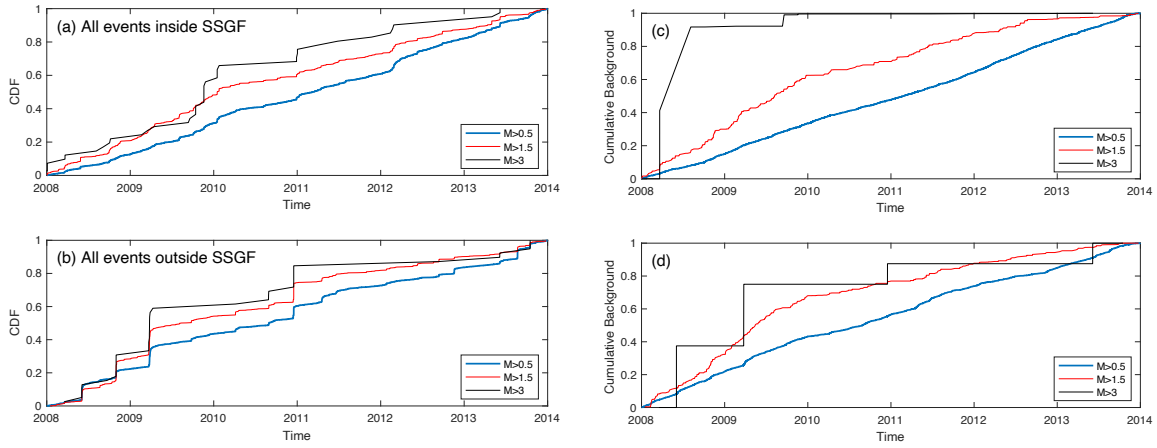

Figure 3.10. Normalized CDF of all the events with M>0.5, M>1.5 and M>3 for (a) inside SSGF and (b) outside SSGF. (c) and (d) normalized CDF of background seismicity for inside and outside SSGF.

3.4.2.2 Spatial and Temporal variation of b-value

The b-value in Gutenberg-Richter's law could be used to investigate the distribution of event magnitudes and the stress state of surrounding regions (Tormann et al., 2015; Nishikawa and Ide, 2014). Previous studies have found that b-value for events inside SSGF is higher than events outside the geothermal field (Cheng and Chen, 2017). The Gutenberg-Richter relationship for events inside and outside SSGF for both matched-filter and SCSN catalogs are in Figure 3.11. It is clear that seismicity inside SSGF has higher b-value than outside for both catalogs. Time-series of b-value inside and outside SSGF region from 2008 to 2013 are in Figure 3.12. There is an increasing trend of b-value inside SSGF, and the b-values are higher than outside of SSGF in general. The spatial distribution of b-value is shown in Figure 3.13. The cluster events with high b-value is close to the center of AB, and is also close to the high density of injection and production wells around the area.

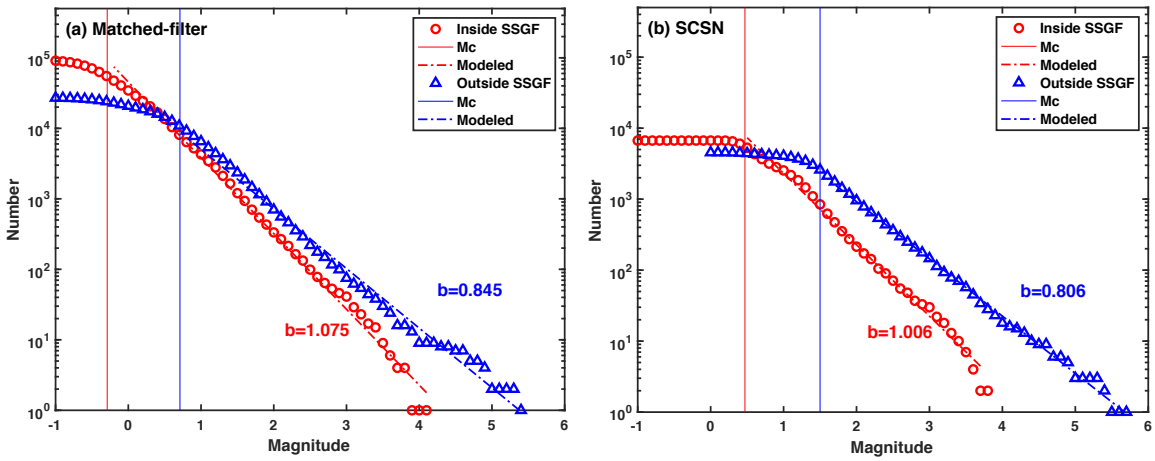

Figure 3.11. Gutenberg-Richter relationship for events inside and outside SSGF for (a) matched-filter detected catalog in this study, (b) SCSN catalog from Hauksson et al. 2013.

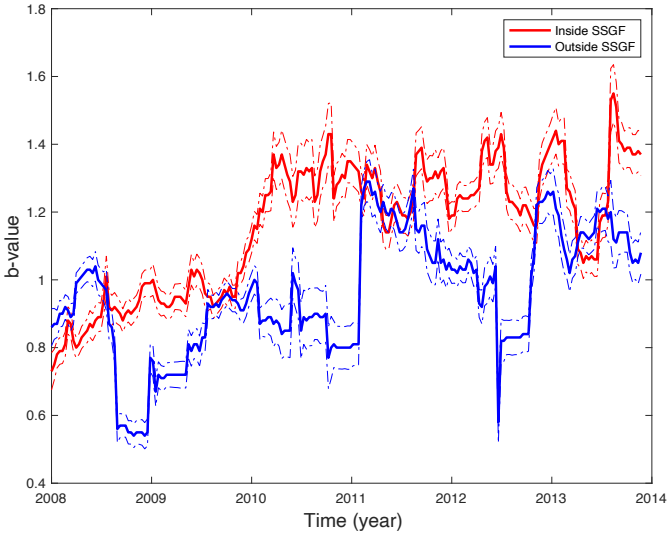

Figure 3.12. The b-value time series from 2008 to 2013.

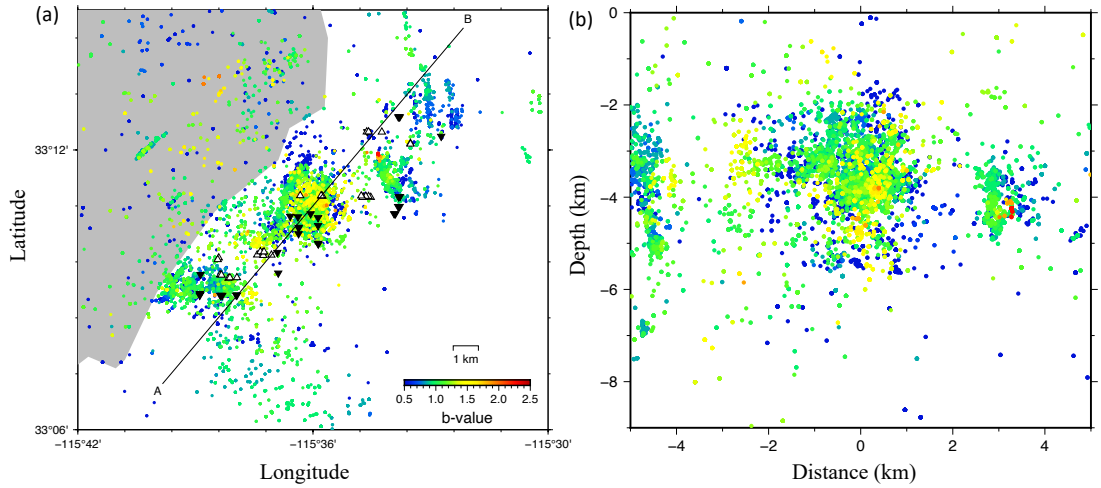

Figure 3.13. The distribution of b-value in (a) map view (b) depth projection along direction AB.

3.5 Discussion

Based on the previous analysis, the 08/03/2009 M6.9 and 04/04/2010 M7.2 earthquakes have both instantaneous and delayed triggering, and the 01/10/2010 M6.5 and 02/06/2013 M8.0 earthquakes have only delayed triggering. The 12/30/2009 M5.8, 02/27/2010 M8.8 and 03/11/2011 M9.1 earthquakes have possible triggering with a lower Mc=-0.5. All the three positive triggering events are within 1000 km away from SSGF, while none of the M>8 distant earthquakes trigger any clear seismicity increase. We estimate the peak dynamic stress change of all the earthquakes with Peak Ground Velocity (PGV) of the low-pass filtered 1 Hz waveforms, and three of the triggering events have dynamic stress changes above 20 kPa (Figure 3.14). However, the dynamic stress change of the 01/10/2010 M6.5 and 02/06/2013 M8.0 earthquakes are smaller than many other earthquakes, and it is not followed by instantaneous triggering, which indicates that their triggering process is likely controlled by other factors. The seismicity after 1 day of the triggering mainshocks are displayed in Figure 3.15. The local events

after the two magnitude 6 events are more concentrated in space, and the ones after the 04/04/2010 M7.2 earthquake have both concentrated and diffused spatial patterns.

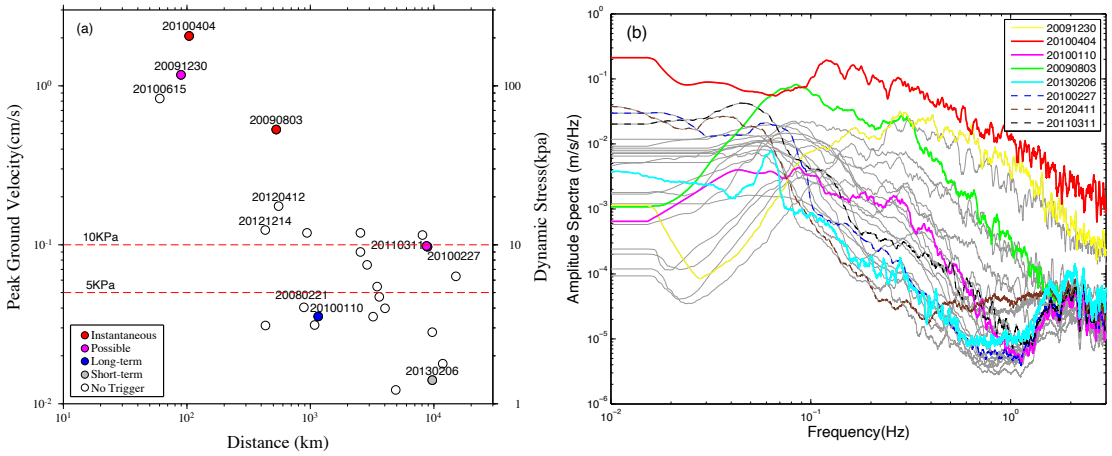

Figure 3.14. (a) Peak ground velocity vs distance of all the earthquakes studied, and the corresponding estimated dynamic stress change is labeled on the right. (b) Amplitude spectra of the all the events during surface waves.

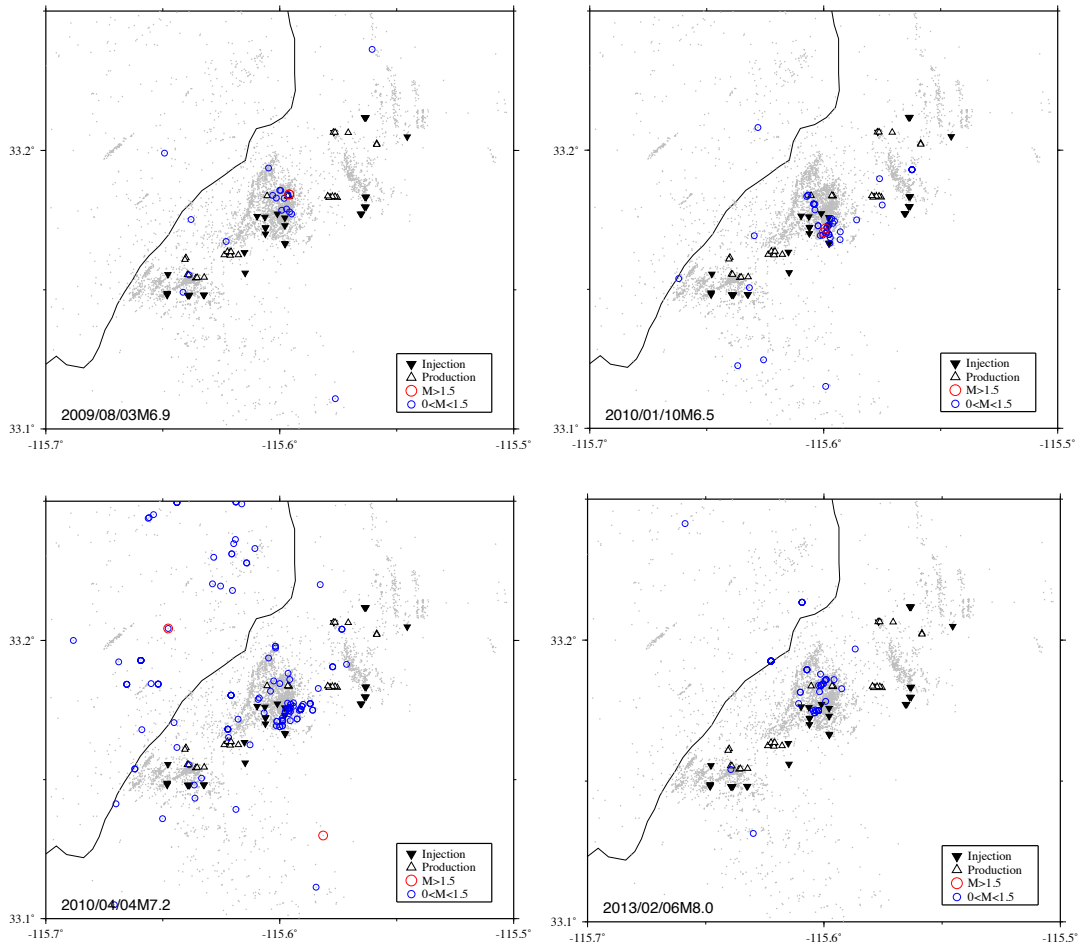

Figure 3.15. The triggered events in SSGF after 1 day of the four triggering earthquakes.

Both earthquakes within 2008-2014 and outside the study period showed that moderate size earthquakes with regional distance from SSGF are more likely to trigger seismicity instantaneously in SSGF. Based on Figure 3.16, the amplitudes of the events that have instantaneous triggering are systematically higher in frequency ranges above 0.1 Hz, which follows the threshold function in frequency domain in the Geysers geothermal field: $\varepsilon_T(f) = K/f$, where f is the frequency and K is an empirical value from observations (Gomberg and Davis, 1996). We then compare the PGV and the maximum high-pass 5 Hz filtered amplitude of triggered events during surface waves, and find that the PGV and maximum amplitude are correlated with Pearson's correlation

R=0.87 (Figure 3.17). Meanwhile, the seismicity rate during surface waves (Table 2) are not well correlated with PGV of the triggering earthquakes. Our result is similar to the study of Aiken et al. (2016), which found that the maximum magnitude of triggered events in the Geysers geothermal field is related to the peak dynamic stress change of mainshocks. Here we use maximum amplitude of waveforms rather than their magnitudes, because we do not have the catalog and magnitude information of triggered seismicity outside our study period. We note that while the peak amplitude is a consistent estimation of event magnitude, we cannot take into account the source-receiver distance. However, since most of the triggered events occurred within the SSGF, the distance factor should not dominate the pattern observed in Figure 3.17.

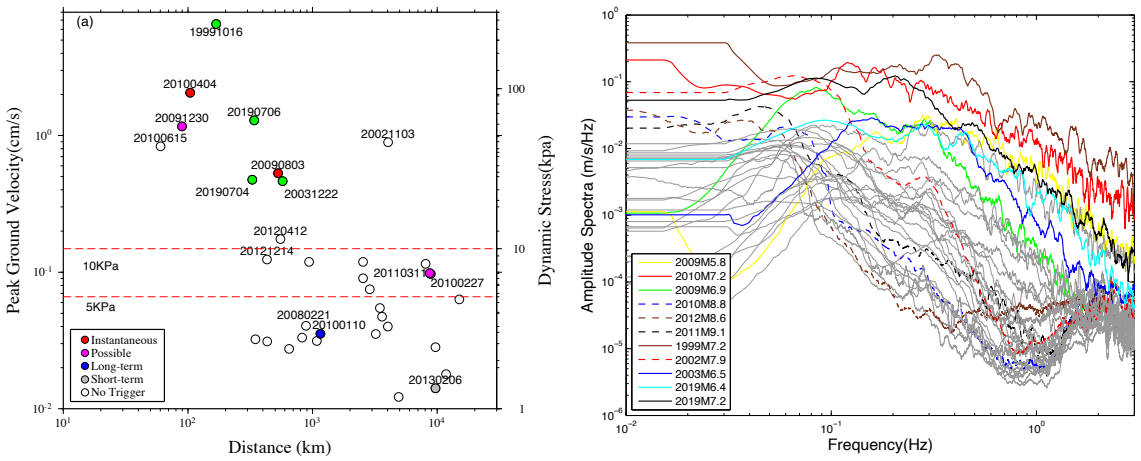

Figure 3.16. (a) Peak ground velocity vs distance of all the earthquakes and the events outside the study period. (b) Amplitude spectra of the all the events and events outside the study period during surface waves.

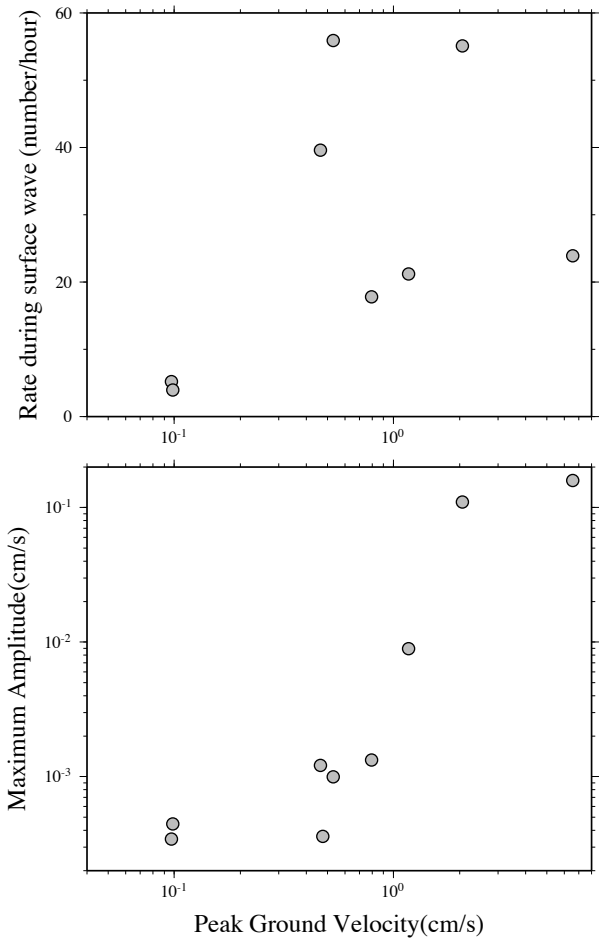

Figure 3.17. (a) Seismicity rate during surface wave and (b) Maximum amplitude of triggered events versus PGV for all the positive and clear triggering earthquakes.

Aiken et al. (2016) compared the b-value of triggered and non-triggered sites, but did not find any difference in the mean b-value. They concluded that the b-value may not be the proper 'stressmeter' for Geysers. One possible reason that the b-value is not showing any different stress state is they were using catalog events. We investigate whether the b-value reveal stress state difference between triggered or non-triggered sites with the new catalog. We divide the region with latitude and longitude range of [33.1°, 33.4°] and [-115.7°, -115.5°] to $0.01° \times 0.01°$ nodes, and compute the b-value of pre-mainshock events that are in a $0.015° \times 0.015°$ square from the center of the node. We require there are at least 200 events in each node before the mainshock to calculate Mc,

and at least 100 events above Mc to calculate b-value. The nodes that contains events one day after the triggering mainshocks are considered triggering nodes. The mean b-value of triggered nodes are 0.87, and 0.82 for non-triggered nodes. We then compare the mean b-value with student's test, and get $p = 0.0047$, indicating the mean b-value of them are different at 95% confidence. The higher b-value in triggered nodes indicates they are in a relative low stress state, and hence more sensitive to external stress changes.

3.6 Conclusion

In this study, we systematically analyze dynamic triggering and long-term seismicity change in the SSGF with a matched-filter detected (MFD) catalog from 2008 to 2013. This study finds that earthquakes with M6-7.5 from regional distance are prone to trigger small magnitude events inside SSGF than large M>8 events at teleseismic distances. The long-term seismicity shows that M>1.5 events are likely correlated with net production rates, while smaller events are not regulated by the geothermal production/injection rates. The b-values inside SSGF are higher than outside SSGF, and there is an increase of b-value, which is consistent with the long-term poroelastic contraction due to geothermal production (Taira et al., 2018).

CHAPTER 4. DETECTING AFTERSHOCK SEQUENCE OF THE 2015 MW7.5 HINDU KUSH INTERMEDIATE-DEPTH EARTHQUAKE

This chapter is a study on detection and analysis of aftershock sequence following the 2015 Mw 7.5 Hindu Kush intermediate-depth earthquake. Here we use the waveform matching technique to systematically detect earthquakes around the 2015 mainshock. The results presented in this chapter are from Li et al. (2018a, GJI).

4.1 Summary

The 2015 Mw7.5 Hindu Kush earthquake occurred at a depth of 212.5 km beneath the Hindu Kush region of Afghanistan. While many early aftershocks were missing from the global earthquake catalogs, this sequence were recorded continuously by 8 broadband stations within 500 km. Here we use a waveform matching technique to systematically detect earthquakes around the mainshock. More than 3,000 events are detected within 35 days after the mainshock, as compared with 42 listed in the ANSS catalog (or 196 in the ISC catalog). The aftershock sequence generally follows the Omori's law with a decay constant p=0.92. We also apply the recently developed double-pair double-difference technique to relocate all detected aftershocks. Most of them are located to the west of the mainshock's hypocenter, consistent with the westward propagation of the mainshock rupture. The aftershocks outline a nearly vertical southward dipping plane, which matches well with one of the mainshock's nodal plane. We conclude that the aftershock sequence of this intermediate-depth earthquake shares

many similarities with those for shallow earthquakes and infer that there are some common mechanisms responsible for shallow and intermediate-depth earthquakes.

4.2 Introduction

Detailed observations of deep earthquake sequences can be used to constrain their physical models (e.g., Zhan, 2017). For example, earlier studies demonstrated that deep earthquakes typically have lower aftershock productivity than shallow earthquakes, suggesting different nucleation/rupture processes (Kagan and Knopoff, 1980; Prozorov and Dziewonski, 1982; Frohlich 1987; Persh & Houston, 2004; Poli et al., 2016a, 2016b). However, at least some deep earthquakes were followed by abundant aftershock sequences decaying with the Omori's Law, such as the March 1994 Tonga deep earthquake (Wiens et al., 1994; Nyffeneger and Frohlich, 2000). The 1994 Tonga sequence could be a rare case, because it was well recorded by an 8-broadband station array around the epicenter, while most deep earthquakes remain poorly covered by regional or global seismic networks. Hence, it is still not clear whether the relative lack of aftershocks is real, or due to the paucity of near-field recordings.

It is well known that global/regional earthquake catalogs are incomplete immediately after a large shallow earthquake, mainly due to overlapping events with high seismicity rate or the masking of coda wave from the mainshock and large aftershocks (Kagan, 2004; Peng et al., 2007; Iwata, 2008). Although no detailed investigation of early aftershock completeness following large deep earthquakes was performed before, we expect that at least some deep aftershocks could be missing for the same reason. It is important to detect those missing early aftershocks for deep earthquakes, because they

not only help to define mainshock rupture plane, but also provide important clues on possible physical mechanisms (Wiens et al., 1994; Houston, 2015).

In this study, we apply the WMFT to the 2015 Mw7.5 intermediate-depth earthquake sequence in the Hindu Kush region of Afghanistan. We choose this sequence, mostly because several broadband stations are located within 500 km distances in Afghanistan and neighboring countries. In addition, the mainshock slip distribution (http://earthquake.usgs.gov/earthquakes/eventpage/us10003re5#finite-fault, USGS, last accessed 06/2016), its sub-event characteristics and rupture process (Poli et al., 2016a; Zhan and Kanamori, 2016) are available, allowing us to compare our detection results with the mainshock behaviors to better understand this sequence and general behaviors of intermediate-depth earthquake sequences.

4.3 Study Region

The Pamir-Hindu Kush seismic zone is located in the western syntaxis of Himalayas, a region with abundant intermediate-depth earthquakes. The seismicity beneath Hindu Kush mostly occurs in the depth range of 70 - 250 km, and is slightly deeper than the Pamir region (Figure 4.1). Relocated seismicity in both regions generally outlines a steeply northward dipping structure beneath Hindu Kush, and a southward dipping under Pamir (Pegler and Das, 1998; Negredo et al. 2007; Sippl et al., 2013). It is still under debate whether there is a single contorted slab or two subducting slabs under the Pamir and Hindu Kush (Billington et al., 1977; Vinnik et al., 1977; Roecker et al., 1980; Chatelain et al., 1980; Hamburger et al., 1992; Negredo et al., 2007; Sippl et al., 2013; Kufner et al., 2016; Kufner et al., 2017). Pavlis and Hamburger (1991) showed that there were a small percentage (3 out of 40) of moderate-to-large (M>5.6) intermediate-

depth earthquakes having clear aftershock sequences in Hindu Kush. For some large events without clear aftershock sequences, they suggested that their aftershocks might be too small to be detected.

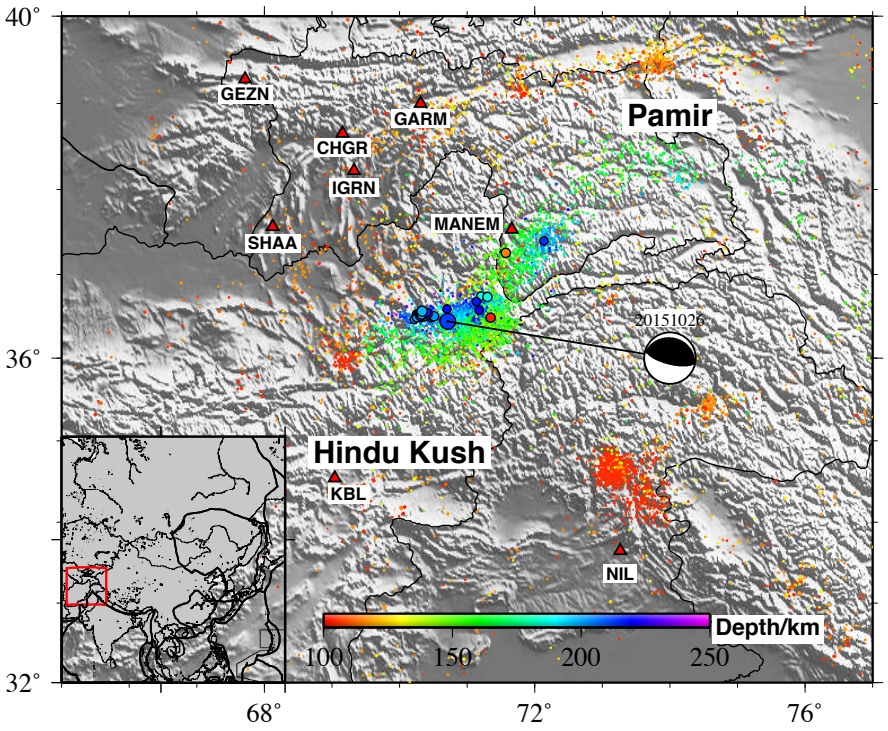

Figure 4.1 - Map showing the study region around Hindu Kush. Earthquakes are sized according to their magnitudes. Colored dots are background seismicity since 2000 and their hypocentral depths are indicated by the color. The red triangles are stations used in this study. Inset shows the location of Pamir-Hindu Kush region, and black thick line indicates plate boundaries.

On October 26th, 2015, a Mw 7.5 earthquake occurred at the depth of 213 km in the Hindu Kush region of Afghanistan, causing significant damages and casualties. There are recurring Mw >7 intermediate depth earthquakes in the Hindu Kush region every 10-15 years, and the previous one was a Mw7.4 earthquake on March 2002 with a close hypocentral location (Zhan and Kanamori, 2016; Poli et al., 2016a). The USGS and Global CMT focal mechanism solutions for the 2015 event showed either a nearly

vertical reverse or shallowly dipping thrust fault. Poli et al. (2016a) found that the mainshock has two rupture stages: a ~10 s precursory event with small P wave amplitude, and a larger P wave onset. These two stages indicated clear changes in rupture direction and energy radiation. Zhan and Kanamori (2016) determined four sub-events for this mainshock: the second and third sub-events are to the west of epicenter, while the forth one is to the east. They also mentioned that the surface tectonic loading (~1 cm/yr) cannot explain the short occurrence intervals for Mw>7 earthquakes in Hindu Kush (~10 cm/yr). Instead, these large earthquakes could be loaded by slab internal deformation (Lister et al., 2008).

4.4 Data and Analysis Procedure

We download continuous waveform 3 days before and 35 days after the 2015 Mw7.5 Hindu Kush earthquake recorded by eight nearby broadband stations with a distance ranging from 80 km to 500 km of networks IU and TJ from the IRIS Data Management Center (DMC). Two of the eight broadband stations (Figure 4.1) record continuously with a sampling rate of 40 Hz (BH), while the rest record with 100 Hz (HH). A visual inspection of high-pass filtered waveforms and spectrogram reveals numerous aftershocks within the first hour after the mainshock (Figure 4.2). The earliest aftershock listed in the Advanced National Seismic System (ANSS) catalog is a M4.8 event around 40 minutes after the mainshock, indicating that many early aftershocks were not listed in this global catalog.

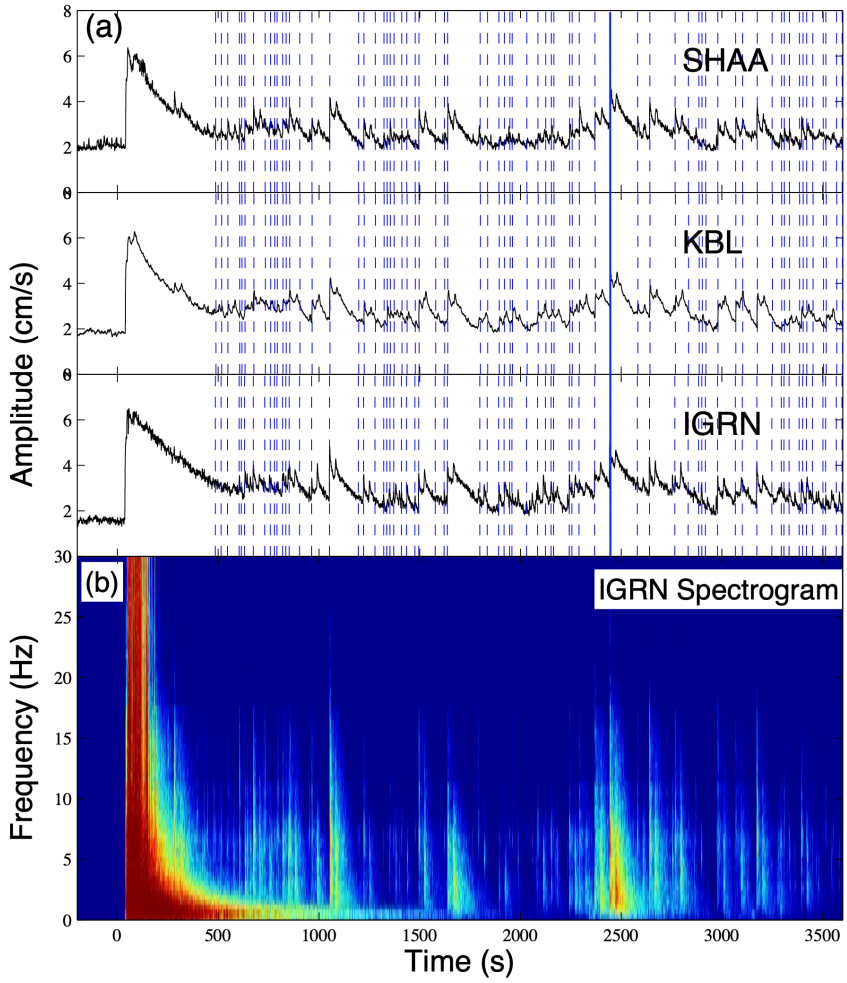

Figure 4.2 - (a) Envelope function of 2-8Hz band-pass filtered waveform of station SHAA, KBL and IGRN, respectively. Solid blue line represents the M4.8 event on the ANSS catalog, and dashed blue lines are all detected events with 9MAD by the WMFT within the first hour. (b) Spectrogram of station IGRN.

The analysis procedure of the WMFT generally follows Meng et al. (2013) and is briefly described here. We select 132 events between 05/20/2015 and 12/31/2015 listed in the ANSS catalog as templates with inter-event distances less than 10 degrees relative to the Mw7.5 mainshock, and depth between 70 km and 400 km. Both template and continuous waveforms are band-pass filtered at 2-8 Hz, because this frequency range has relatively good signal-to-noise ratios (SNRs) and is capable of suppressing most of the mainshock coda after a few hundred seconds (Figure 4.2b). We manually pick the P/S

phase arrivals for each template and compute the SNR for each trace, which is defined as the ratio between the cumulative energy for the signal (template) window (either P or S wave) and noise window (same length as the signal window ending 1s before P wave). Following Li et al. (2016), the template windows are set to be 1 s before and 5 s after P wave arrival, and 1 s before and 11 s after arrival of S wave for three components of each station. Only template events containing at least 3 windows with SNR above 5 are used in further detection. We also down-sample the band-pass filtered waveforms to 0.05 s (20 Hz) to reduce the computational cost, and calculate the cross-correlation (CC) functions for selected *P* and *S* windows. Then we stack all CC functions after shifting them to the origin time of the template event, and output positive detections above a certain threshold. This is defined as the median CC value plus 9 times median absolute deviation (MAD) of the stacked daily trace (Peng and Zhao, 2009). Duplicated detections from multiple templates within a short time window are removed by keeping only the highest detection in every 12s. The location of the newly detected event is initially assigned as the location of the best-matched template, and the magnitude is calibrated by the median peak amplitude ratio (Peng and Zhao, 2009). Figure 4.3 shows a positive detection (with inferred magnitude of 4.57) occurred 1184 s after the mainshock with a mean CC value of 0.626 (~33 times the MAD), and the corresponding template occurred on 2015/10/26 16:47:21 UTC, with a magnitude of 4.50.

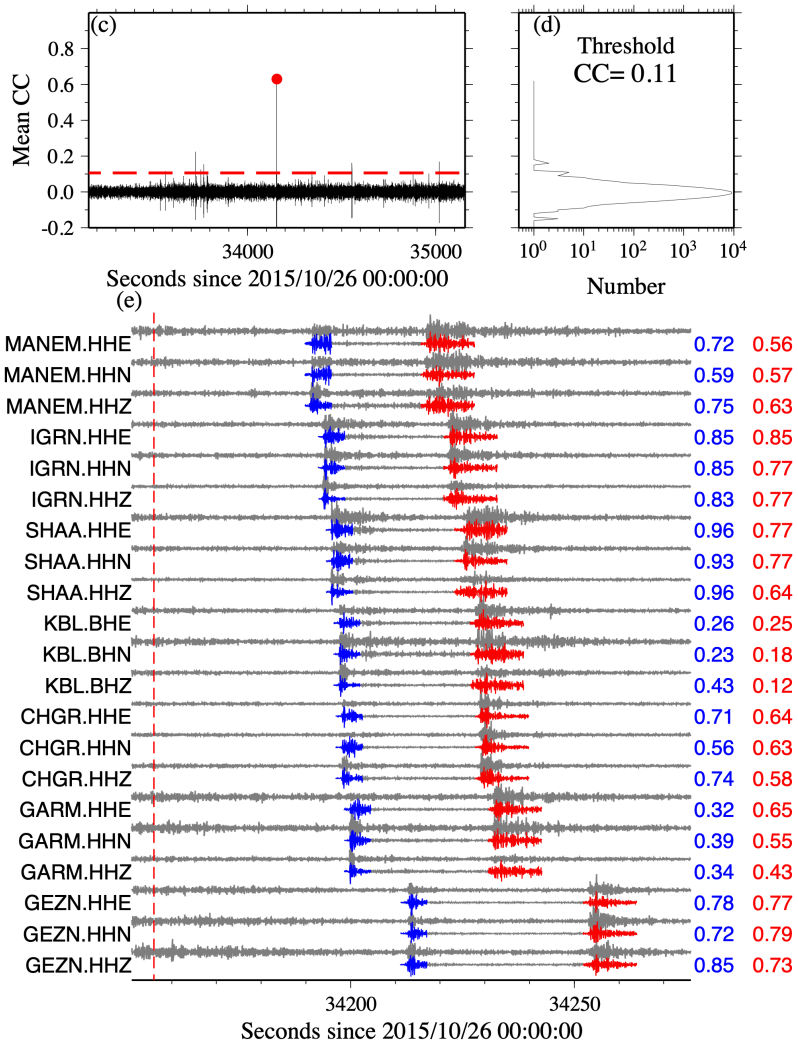

Figure 4.3 - Example of a positive detection by a M4.5 template occurred on 2015/10/26 16:47:21. (a) Mean cross-correlation coefficient (CC) trace since 2015/10/26 00:00:00, the red dot represents the detected event plotted in (c), and the red dashed line is threshold of detected events (9MAD). (b) Histogram of the mean CC trace. (c) Comparison of continuous data and template in the matched time, blue traces are P wave windows, red traces are S wave windows of the template event, STATION.CHANNEL and CC values are labeled on left and right side, respectively.

In previous studies (e.g., Meng et al., 2013; Li et al., 2016; Wu et al., 2017; Ruan et al. 2017, etc.), the location of the best-matching template are assigned to the newly detected event. This is valid to some degree since only nearby events could match the templates with high CCs. However, unless the mean CC value is 1, there are always

minor time differences between the highest CC value of each trace and the stacked CC trace (i.e., the origin time of detected event), indicating small spatial offsets between the template and detected events (Figure S 4.1). Such time shifts in turn can be used to relocate newly detected events with respect to the template events (e.g., Shelly et al. 2013; Zhang and Wen 2015).

Here we apply the newly developed double-pair double difference (DD) location algorithm (Guo and Zhang 2017; Guo et al. 2017) to relocate all detected earthquakes and template events. By making use of both station-pair and double-pair differential times with a hybrid strategy, this location method can improve both absolute and relative earthquake locations at the same time, as compared to the traditional event-pair DD relative location method (i.e., hypoDD) (Waldhauser & Ellsworth, 2000). Here we cut waveforms of all detected events, and compute cross-correlation (CC) differential times between pairs of events using a 3s window (1-s before and 2-s after) around the P and S arrival time for each event. We only use event pairs containing at least 4 differential times with CC coefficients higher than 0.75. Example of two events with 4 differential times is shown in Figure S 4.1.

As mentioned before, the initial locations of the detected events are assigned as the best-matched templates. We then construct double-pair data for all events using the aforementioned computed CC differential times. In order to better constrain the absolute locations, we also include the station-pair differential times from P and S arrivals for selected 550 events with SNR>50, and relocate all events in the double-pair DD algorithm. The P wave velocity model is modified from a 1D layered model (Sippl et al.,

2013) and converted to a 1D gradient model, with a Vp/Vs ratio of 1.74 to estimate the S-wave velocity.

4.5 Results

4.5.1 Event Detection

By scanning through continuous waveforms 3 days before and 35 days after the 2015 Hindu Kush mainshock with 132 templates, we detect 3,120 events, including 1,752 events in the first 3 days after the mainshock above the threshold of $9 \times$MAD. In comparison, only 7 events are detected 3 days before the mainshock, and only 42 and 196 aftershocks are listed in the ANSS and the International Seismological Centre (ISC) catalog, respectively. After double-pair DD relocation, we obtained 1,911 events with relative location uncertainties smaller than 5 km in three dimensions (

Table 6).

Table 6. Detailed information of detected and relocated events.

Number of Events Detected	Event Magnitude		Number of Events Relocated	Relative Location Uncertainty	
	>2.5	>3.1		< 10 km	< 5 km
3120	1391	519	2234	2086	1911

In the newly detected catalog, a M=5.32 event occurred on 10/26/2015, ~2400 s after the mainshock, which was not listed in the ANSS catalog. The template event had a magnitude of 4.1 and occurred on 2015/11/12. The mean CC value is 0.115, just above 10 times the MAD. It is clear from the continuous waveform that one event did occur at the detection time (Figure S 4.2). To evaluate the accuracy of magnitude calibration, we compare the magnitudes of template events detected from other templates (after removing self-detection) and those listed in the ANSS catalog (Peng and Zhao, 2009). As shown in Figure S 4.2b, the magnitude differences generally follow the tenfold

relationship with median amplitude ratios, indicating that the magnitudes of template events are consistent.

4.5.2 Aftershock Statistics

Figure 4.4 shows the magnitudes versus logarithmic times following the mainshock for the detected catalog. It is evident that our detection capability increases with time, likely due to masking effect by the mainshock coda and large aftershocks at earlier times. We use the ZMAP software (Wiemer, 2001) to perform statistical analysis of the detected catalog. The maximum curvature method (Woessner and Wiemer, 2005) yields a magnitude of completeness *Mc* of 2.7 for the entire sequence, and b=0.73 for the Gutenberg-Ritcher frequency-magnitude distribution (Figure 4.4 a, b). We also apply a rate-dependent algorithm (Hainzl, 2016) to estimate a varying *Mc*, and find that the *Mc* starts as 4.6 at ~0.03 days (~2600 s) after the mainshock, and decreases to 2.7 around 1 day after mainshock. If we use a constant *Mc*=2.7, the aftershock rate would obey the Omori's law with a decaying constant p=0.92 (Figure 4.4c). To verify the robustness of our result, we also analyze the sequence using 12×MAD as the cutoff threshold. It ends up with the same *Mc* of 2.7, and the corresponding p value is *0.95* (Figure S 4.3).

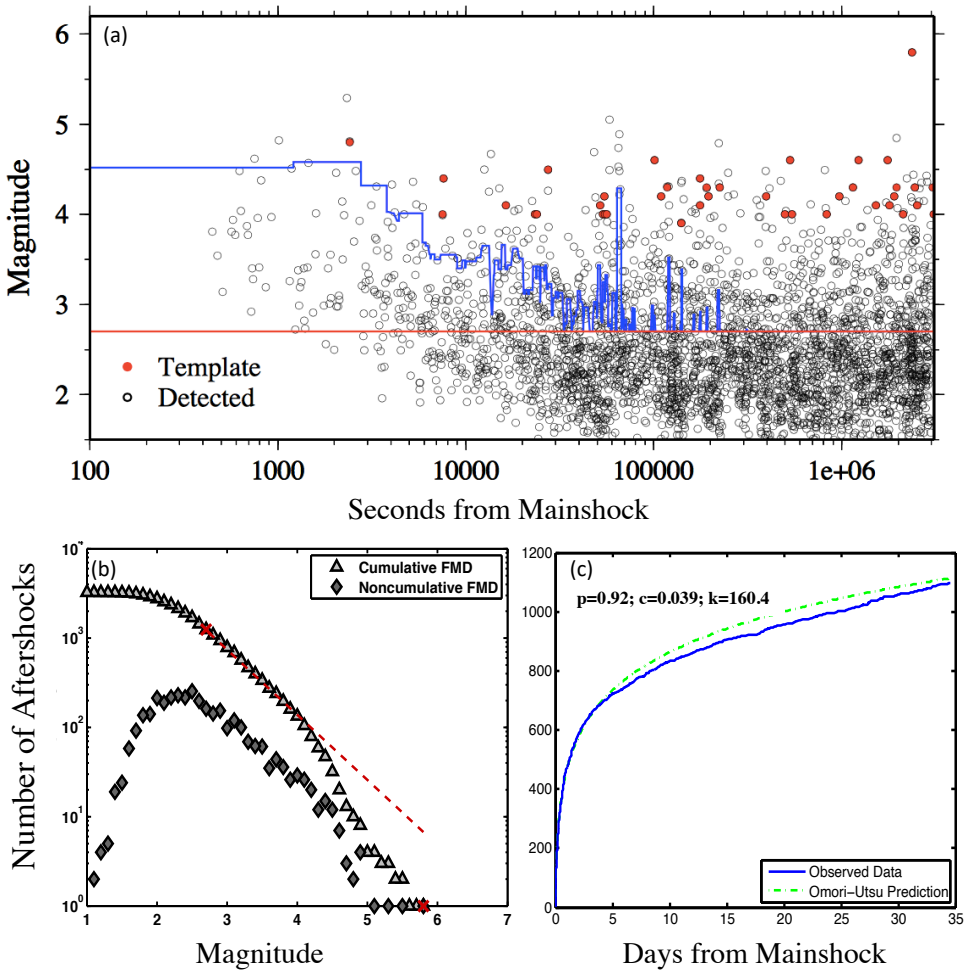

Figure 4.4 - (a) Magnitude versus logarithmic time of detected events. Red dots and black circles are templates and detected events, respectively. The red solid line marks the Mc=2.7, while blue solid line marks changing Mc after mainshock. (b) Frequency-magnitude dependence for detected aftershocks generated by ZMAP, and the red dashed line indicates the result of "Best Combination". (c) Cumulative number of aftershocks in 35 days after the mainshock, compared with the Omori-Utsu prediction.

4.5.3 Event Relocation

Figure 4.5 shows the spatial distribution of all relocated events and templates. It is clear that most aftershocks occurred to the west of mainshock hypocenter, near the edge of the large mainshock slip (Figure 4.5a, c). The aftershocks occurred in a near-vertical plane from 180 km to 230 km (Figure 4.5b, d). The cross-sections of seismicity are shown in Figure 4.5e, which delineate a near-vertical southward dipping plane. This is

consistent with the general trend of south-dipping seismicity deeper than 180 km (Kufner et al., 2017; Zhan and Kanamori, 2016; Poli et al., 2016a).

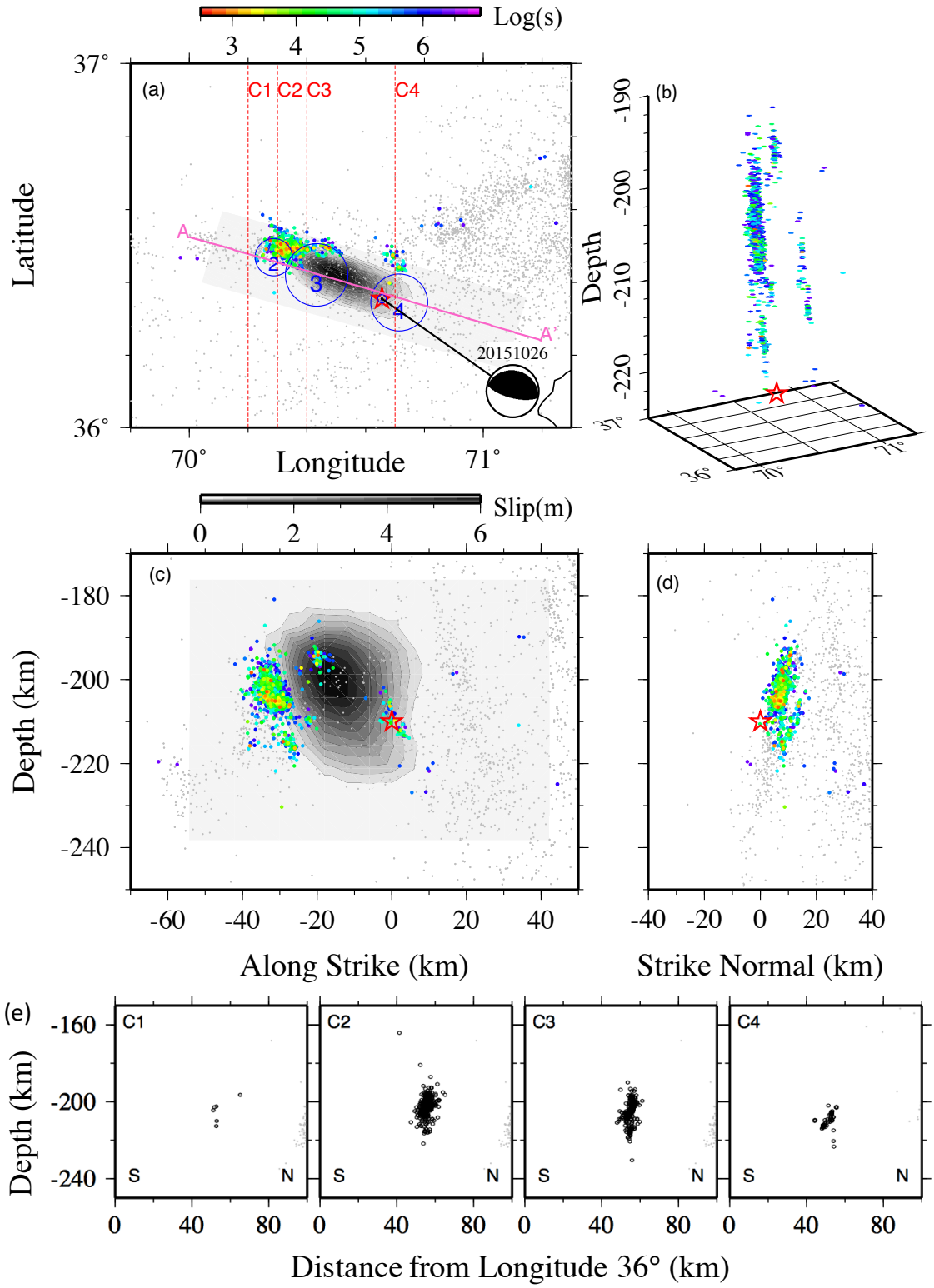

Figure 4.5 - (a) Map view of detected aftershocks after relocation. The color of aftershocks is their relative time to the mainshock. The gray area and contours are slip distribution from finite fault model (USGS), after shifting the epicenter to the subevent 1 in Zhan & Kanamori (2016). Background seismicity between 2008-2010 and 2012-2014 are marked as gray dots (Kufner et al 2017), and blue circles mark subevents from Zhan & Kanamori (2016). Dashed red lines are cross-section profiles, AA' marks strike direction in figure (c) and (d). (b) Three-dimensional view of aftershocks. Depth distribution of aftershocks (c) along and (d) perpendicular to strike. (e) Cross-sections of seismicity in (a) starting from longitude of 36°, seismicity within 5 km are projected.

We find a moderate expansion of aftershocks with along-strike distances (Figure 4.6). To better quantify this, we compute the activation time when the number of earthquakes within a small bin reaches to a certain threshold N (Kato and Obara, 2014; Yao et al., 2017; Wu et al., 2017). Here we set the bin size as 5 km, and a sliding window of 1 km and $N = 20$. Figure 4.6 shows that the activation time is at its minimum around 35 km west of the epicenter, and are migrating to two sides, with some smaller patches eastward being activated around 10^5 s after the mainshock.

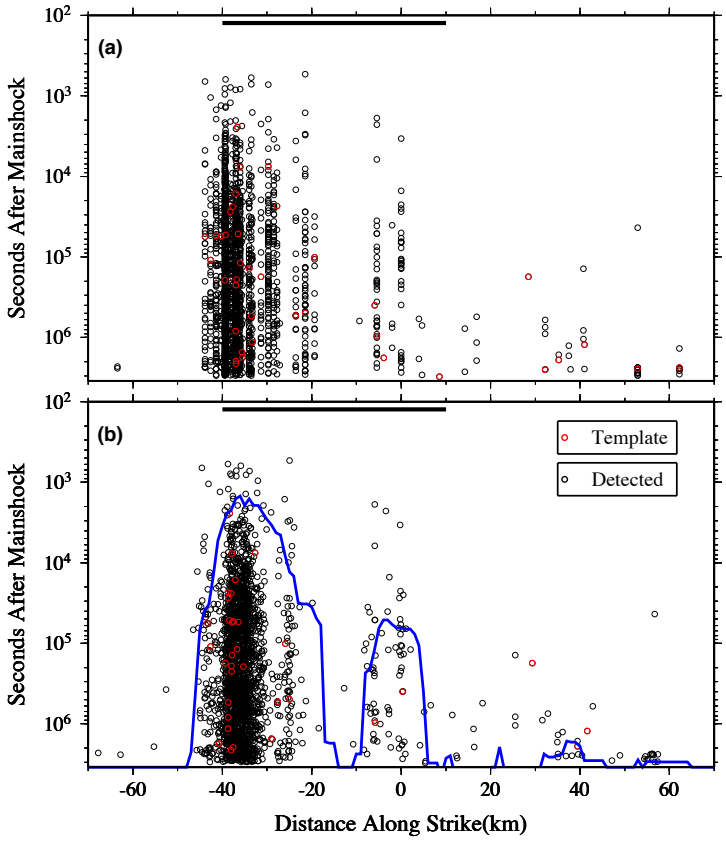

Figure 4.6 - Distribution of aftershock along strike evolving with time before (a) and after relocation (b). The red circles are template events and black circles are detected events, the thick black line represents the rupture region of mainshock according to finite fault model, and the blue line marks activation time.

We use the bootstrapping method (Efron and Gong, 1983; Efron and Tibshirani, 1991) to quantify the relative location uncertainties of relocated seismicity for the target sequence from the double-pair DD location method (Guo and Zhang, 2017; Guo et al., 2017). Both station-pair and double-pair differential times are randomly resampled in the bootstrapping method and are then used for the inversion with the same inversion procedure as for the real data. We repeat the process 50 times to obtain the standard deviation for each event. We calculate the median of the bootstrapping relative location uncertainties for all events, which help to suppress the effect of the outliers (Table 7). In

general, the median relative location uncertainties are less than 0.2 and 0.6 km in horizontal and depth, respectively.

Table 7. The median values of relative location uncertainties in three directions of all relocated events of the real data inversion, the noise-free synthetic test and the noisy synthetic test.

Location Uncertainty		X (km)	Y (km)	Z (km)
Relative location	Real data inversion	0.182	0.116	0.549
	Noise-free synthetic test	0.005	0.004	0.021
	Noisy synthetic test	0.229	0.166	0.731
	Initial error	2.052	1.144	2.810
Absolute location	Noise-free synthetic test	0.390	0.912	1.808
	Noisy synthetic test	0.500	0.967	2.200
	Initial error	3.1356	2.5114	5.3850

4.5.4 Comparisons with other catalogs

We compare our detection results with the ISC catalog, and find 150 out of the 196 aftershocks within 35 days of the mainshock from the ISC catalog have time difference less than 6 s (Figure S 4.4). The magnitudes of the detected catalogs are different when comparing with those listed in the ISC catalog (Figure S 4.4a,b). To investigate this further, we compare the magnitudes of events listed in both ANSS and ISC catalogs. There are some differences in magnitudes between the common events in the ANSS and ISC catalogs (Figure S 4.4c,d). Thus, we believe the discrepancy of magnitudes mostly comes from the different magnitude sources in the ISC catalog.

Kufner et al. (2017) relocated some aftershocks of the 2015 Hindu Kush earthquake from the manually revisited quakeML files received from GEOFON earthquake bulletins with a master event method. We compare our relocated events with 20 aftershocks listed in Kufner el al. (2017) (Figure S 4.5). In both catalogs, aftershocks were mainly distributed to the west of mainshock, while aftershocks in Kufner et al.

(2017) were systematically ~10 km shallower than our results. The discrepancy in depths might come from different initial locations and different location methods as well as velocity models between this study and Kufner et al. (2017) and will be further discussed in section 4.5.1 and 4.5.2.

Relocated aftershocks in this study, Poli et al. (2016a) and Kufner et al., (2017) all show that most aftershocks are located to the west of mainshock and delineated a near-vertical south-dipping plane. A large portion of aftershocks located in this study were close to the second and third subevent from Zhan and Kanamori (2016), and concentrated in near-vertical south-dipping plane with width less than 20 km (Figure 4.5). Due to the challenges of constraining the depths of these events, we did not directly compare the absolute location and depth of mainshock subevents and aftershocks in our study and others (Poli et al., 2016a; Zhan and Kanamori, 2016; Kufner et al., 2017).

4.5.5 Aftershock Productivity

As mentioned before, for many large deep earthquakes with well-recorded aftershock sequences, the numbers of aftershocks are small, generally less than 500 (Frohlich, 2006; Prieto et al., 2012; Houston, 2015). In this study we have detected more than 3,000 aftershocks in the first 35 days following the 2015 Hindu Kush earthquake. To further quantify its aftershock productivity, we compare with shallow earthquakes and other deep earthquakes.

We first estimate the aftershock number from empirical equations given in Yamanake and Shimazaki (1990),

$$logN = \frac{2}{3}\, logM_0 - 17.05 \tag{11}$$

for shallow interplate earthquakes, and

$$logN = \frac{1}{2}\, logM_0 - 12.08 \quad (12)$$

for shallow intraplate earthquakes. The estimated aftershock numbers are 8.92 and 26.30 for interplate and intraplate earthquakes respectively. We count our number of aftershocks with magnitudes larger than 4.5 in 30 days, and obtain N=16. The above estimation suggests the aftershock productivity of 2015 Hindu Kush earthquake is comparable with that of shallow earthquakes.

We also compare the aftershock productivity with other deep earthquake sequences following a different approach. Persh and Houston (2004) defined a normalized number of aftershocks for deep earthquakes,

$$\log N_{norm} = \log N_{obs} + 8.2 - Mw \quad (13)$$

where N_{obs} is the number of observed aftershocks with M_b>4.5 within 20 days of mainshock, and N_{norm} is the number of normalized aftershocks. With N_{obs} = 13, we obtain N_{norm} =*65.2*, which is larger than the mean value of 47.5 for deep earthquakes between 100 km and 350 km in the study of Persh and Houston (2004). In contrast, only 6 aftershocks with M_b>4.5 were listed in the ANSS catalog. If we set N_{obs} = 6, the corresponding N_{norm} is 30, lower than the mean value.

We also compare the results by calibrating the magnitudes of templates with the ISC catalog. The corresponding statistical parameters are M_c = 2.5, b = 0.82, and the Omori's decay rate p = 0.9 (Figure S 4.6). However, the aftershock productivity becomes much lower with N = 7 in the first method, and N_{norm} = 30 in the second method.

4.5.6 Repeating aftershocks

Because several recent studies have found evidence of repeating earthquakes (i.e., events occurred at virtually the same location with nearly identical waveforms) at

intermediate-depth or deep-focus regions (Wiens and Snider, 2001; Yu and Wen, 2012; Prieto et al., 2012), we also conduct an initial search for possible repeating events based on waveforms of the detected events (including all templates). In detail, we search for event pairs with CC>0.95 (computed with a 16s time window starting 1s before the *P* arrival) in vertical components and CC>0.9 around *S* arrival in horizontal components on at least three stations. We end up getting 15 event pairs, and the total number of repeating earthquakes is about 0.46% of the aftershock sequence. Their recurrence times range from 2 to 15 days. An example of two events with high CC values is shown in Figure 4.7. Their hypocenters are ~0.4 km apart, within our estimated relative location uncertainty.

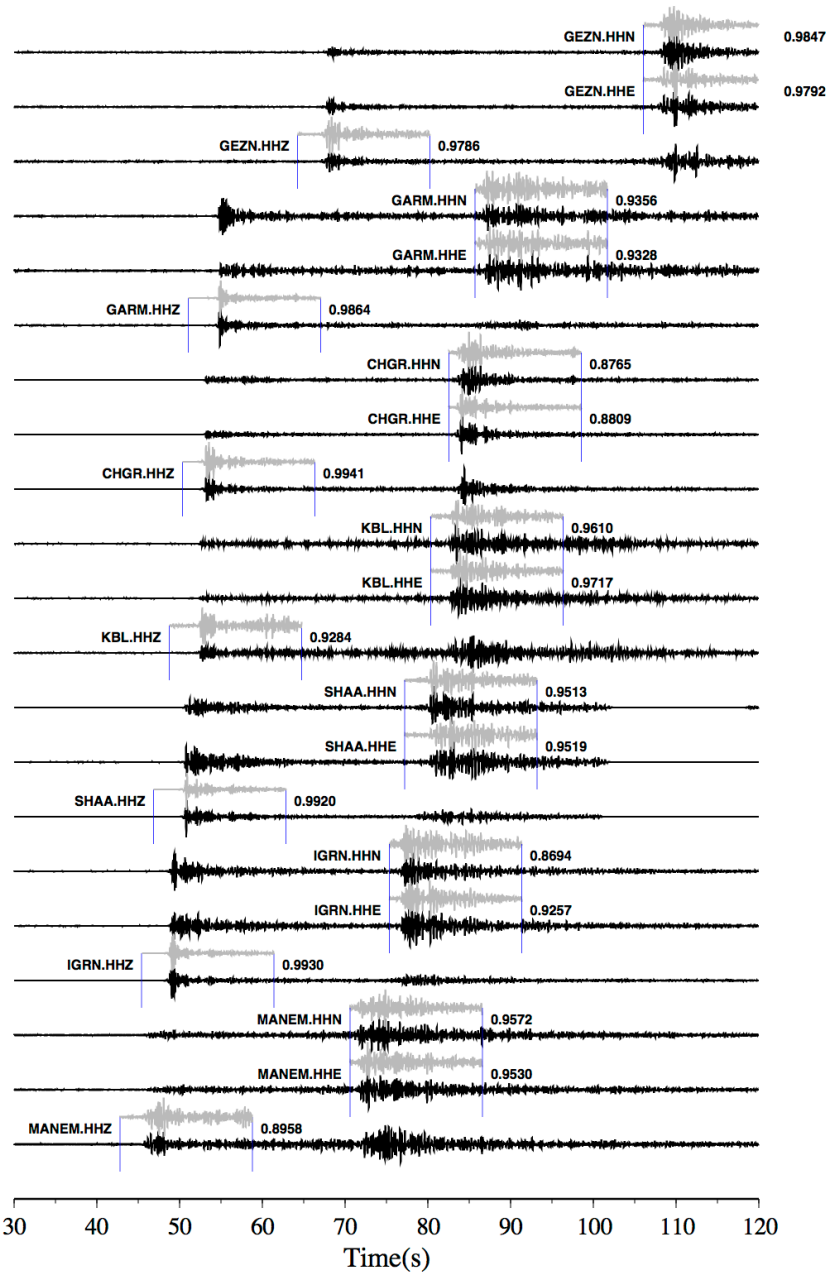

Figure 4.7 - Waveforms of two repeating earthquakes, their origin time are 10/27/2015 03:09:02 and 10/29/2015 06:18:14, respectively. Their inferred magnitudes are 4.74 and 4.46. The cross-correlation values of P and S windows are marked to the right.

4.6 Discussion

4.6.1 Synthetic tests on earthquake locations

To further test the robustness of our relocation process, we perform two synthetic tests with noise-free and noisy data. The synthetic tests are included in the source code of double-pair DD algorithm (Guo and Zhang, 2017). We set the relocated events as "true" locations, and then calculate the synthetic absolute times with the same 1-D gradient velocity model. Then the synthetic station-pair and double-pair differential times are constructed from the synthetic absolute times. For the noisy synthetic test, Gaussian distributed random noise with zero mean and a standard deviation of 0.6s is added to the synthetic data, which is estimated from the final residual of the real data inversion and should represent the level of the Gaussian random error in the real data. We then apply the double-pair DD method to the noise-free and noisy data with the same inversion procedure as the real data inversion described above. The median absolute and relative location errors of the synthetic tests are shown in Table 7. Compared to the initial locations with absolute location error of ~5 km and relative location error of ~3 km, both absolute and relative locations are much better resolved (Table 7). The relative location uncertainties from the noise-free synthetic test are ~0.005 km in horizontal and ~0.02 km in depth, implying double-pair DD location method can achieve high-resolution relative locations with our current event distribution and station coverage. The relative location uncertainties from the noisy synthetic test are ~0.2 km in horizontal and ~0.7 km in depth, and have the same order of magnitude as the relative location uncertainties from the bootstrapping analysis for the real data inversion (Table 7), suggesting that our bootstrapping relative location uncertainty estimation for the real data is reliable. The comparable relative location errors from the real data inversion and this noisy synthetic test (Table 7) indicate that relatively large relative location uncertainty for relocated

aftershocks, on the order of 0.6 km as compared to ~0.1 km for the upper-crustal earthquakes in California (Guo and Zhang, 2017) is probably due to the large data error, which could come from relatively poor station coverage and large hypocentral depth. The absolute location errors (error between "true locations" and relocations) from both of the noise-free and noisy test are ~1 km in horizontal and ~2 km in depth, which approximately reflect absolute location uncertainties of the real data inversion.

4.6.2 Precision of absolute locations

For many earthquake location methods, absolute earthquake locations are difficult to be resolved and rely on the precisions of initial locations. Guo and Zhang (2017) have shown that double-pair DD location method can determine much better absolute locations due to high sensitivity of station-pair data on absolute locations. Their results also showed that the effect from different initial locations are very small for the well-recorded crustal earthquakes in San Andreas Fault. In this study, one primary conclusion is that aftershocks occurred to the west of the mainshock. Hence, the precision of absolute locations from double-pair DD location method is very important. To evaluate the sensitivity of double-pair DD location method on absolute locations and the influence of initial locations, we perform two additional tests with different sets of initial locations. The first test is to move the initial locations 0.15º to the east, 0.10º to the south and 5km shallower, which moves the initial locations in the mainshock slip area. Figure S 4.7 shows that the relocations moved to the northwest of initial locations. The second test is to move the initial locations further away from the mainshock slip area by 0.15º to the west and 0.15º to the north. The relocations then move to southeast (Figure S 4.8). Hence,

both relocations inverted from two different initial locations tend to move towards our preferred relocations shown in Figure 4.5.

Although relocations from different initial locations (Figure 4.5, Figure S 4.7 and Figure S 4.8) are not exactly the same, the majority of aftershocks are to the west of the largest mainshock slip, and delineate a near-vertical south-dipping plane. Similarly, when we shift the initial locations in the noisy synthetic tests, the relocations also tend to move back to the "true" locations (Figure S 4.9, Figure S 4.10). Based on these tests, we argue that the double-pair DD location method is sensitive to absolute locations and that the absolute locations of our preferred relocations (Figure 4.5) are reliable.

4.6.3 Aftershock Sequence and Physical Mechanism

The Hindu Kush seismic zone is one of the three regions in the world with intensive intermediate-depth earthquake activity in a concentrated volume (Prieto et al., 2012; Zarifi and Havskov, 2013), also known as the "earthquake nest". Pavlis el al. (1991) found that the 1983 M 6.7 intermediate-depth earthquake produced more than 89 aftershocks with $M \geq 3.1$ in 34 days, and the aftershock with largest magnitude is smaller than the mainshock by 2.6. Our WMFT detected 519 aftershocks with $M \geq 3.1$ within the same time period for the 2015 event, and the largest magnitude of aftershocks is 5.8, which is 1.7 smaller than the mainshock magnitude. The 2002 Mw7.4 intermediate-depth earthquake in the Hindu Kush nest have 30 $M \geq 3.1$ aftershocks listed in the ANSS catalog, with largest aftershock 2.9 smaller than mainshock in magnitude. All three earthquakes with clear aftershock sequences found by Pavlis et al. (1991) were located very close to the 2015 Hindu Kush earthquake, and with similar focal mechanisms. Because of close locations and similar focal mechanisms to other large intermediate-

depth earthquakes, the 2002 Mw7.4 earthquake (and other previous M6-7 events) may also have missing aftershocks. Therefore, we suspect that some large intermediate-depth earthquakes in the Hindu Kush nest might also have abundant aftershock sequences, which can be verified with the same WMFT method in a further study.

As shown in Section 4.5, the aftershock productivity of the 2015 mainshock is above the average of deep earthquakes if we use the ANSS magnitudes for the templates, and is below average if the template magnitude is from the ISC catalog. This shows that the template magnitudes would affect the productivity estimation of detected aftershocks. In this study we mainly focused on results with ANSS catalog, because the preferred magnitudes in the ISC catalog are from various resources. Further magnitude calibration could be helpful to produce a catalog with a unified magnitude scale (Shelly et al., 2016), but this is beyond the scope of this paper.

There are several physical models on aftershock generation, such as static and dynamic stresses caused by the mainshock, viscoelastic relaxation or fluid diffusion, and afterslip (e.g., Das and Scholz, 1981; Freed, 2005). Viscoelastic response and fluid diffusion are more plausible to aftershocks at longer time span of months to years (e.g., Freed, 2007; Peng and Zhao, 2009; Wu et al., 2017). Static and dynamic triggering mechanism could be evaluated by comparing the resulting stress changes and aftershock distributions (King and Deves, 2015). Although we did not compute static/dynamic stress changes from the mainshock, we found that most aftershocks to the west in the mainshock rupture propagation direction (Figure 4.5). This is qualitatively consistent with similar aftershock observations following some large shallow earthquakes (e.g., 1992 M7.3 Landers earthquakes), suggesting that dynamic stress changes likely

contribute to triggering aftershocks in the rupture propagation direction.

Many recent studies also invoked postseismic deformation as the mechanism for driving early aftershocks (Perfettini and Avouac, 2004; Peng and Zhao, 2009). The direct evidence for afterslip driving aftershocks include consistence of aftershock locations and inverted afterslip from geodetic observations, and aftershock migration following numerical simulation expansion of afterslip (e.g., Kato, 2007; Peng and Zhao, 2009). Some other observations are considered as supporting evidences of afterslip, including slip deficit of mainshock, spatial expansion of aftershocks, and repeating aftershocks (e.g., Yao et al., 2017; Wu et al., 2017). However, given the large hypocentral depth, it's challenging to detect any postseismic signals for intermediate-depth earthquakes using ground-based GPS recordings (Boschi et al., 2010). As shown in Figure 4.5, most aftershocks occurred around the edge of mainshock main slip patch, similar with observations for many large megathrust events (e.g., Hsu et al., 2006; Yao et al., 2017) or strike-slip events such as the 2004 Parkfield earthquake (Bennington et al., 2011). Based on the moderate expansion of aftershock activity with time, together with initial observations of repeaters with high similarities, we hypothesize that afterslip occurred following the 2015 Hindu Kush earthquake and may play a role for driving the aftershock sequence. Further analysis of recurrence times and locations of repeating aftershocks at longer times and stress changes induced by the mainshock could shed light on the driving mechanism of the 2015 Hindu Kush aftershocks.

4.6.4 Implication for Mainshock Physical Mechanisms

Currently there are two widely-accepted candidates for the physical mechanism of intermediate-depth earthquakes: dehydration embrittlement and thermal shear runaway

instability (Prieto et al., 2012). For dehydration embrittlement, an increase of pore pressure due to existence of fluid would reduce the effective normal stress in depth, resulting in brittle failure events (Green and Houston, 1995; Frohlich, 2006; Houston, 2015). Fluids in subduction zones mainly come from dehydration of subducted sediments or metamorphic phase transition (Houston, 2015). Pore fluids also play an important role in aftershock generation following large shallow earthquakes (Nur and Booker, 1972; Bosl and Nur, 2002). In this study, we found that the expansion mostly occurred immediately following the mainshock (Figure 4.6). The relatively slow diffusion of water may suggest that other triggering mechanisms are needed to trigger large amount and rapid expansion of aftershocks shortly after the mainshock.

In the thermal shear runaway instability model, shear deformation in a strain-weakening shear zone generates ductile creep or melting, thus promoting slip on pre-existing faults (Wiens, 2001). Viscous melting has been proposed in some large deep earthquakes such as the 1994 M8.2 Bolivia Earthquake, the second largest deep earthquake ever recorded (Houston, 2015; Zhan and Shearer, 2014). The energy balance of the initial phase of the 2015 Hindu Kush earthquake is similar to the 1994 Bolivia earthquake, likely indicating occurrence of frictional melting (Houston, 2015; Poli et al., 2016a). The thermal shear instability model is also compatible with abundant aftershocks (Frohlich 2006) and possible repeating aftershocks (Wiens and Snider, 2001; Prieto et al., 2012). The short repeating rate of repeaters could be explained by thermal conductive cooling (Wiens and Snider, 2001; Yu and Wen, 2010). Therefore, thermal instability model might be the cause of the mainshock and some aftershocks.

Previous studies showed that the seismicity zone beneath Hindu Kush is dipping

to the north between 60-180 km and to different directions below 180 km (Sippl et al., 2013; Kufner et al., 2017). Kufner et al (2017) suggested that the overturned seismicity zone beneath Hindu Kush is related to the ongoing India slab break-off, which splits the slab and seismicity into two different depth domains. Our aftershock distribution is also consistent with the hypothesis that the 2015 Hindu Kush earthquake and other large earthquakes occur in a thin necking shear zone where the slab breaks off (Lister et al., 2008; Poli et al., 2016a; Kufner et al., 2016; Zhan and Kanamori, 2016). Further study of other aftershock sequences and distributions, as well as detection of smaller earthquakes during interseismic period would provide more information on physical mechanisms of intermediate-depth earthquakes in this region.

4.7 Conclusion

In this study we used the WMFT to detect 3,120 aftershocks within 35 days of the 2015 Mw7.5 Hindu Kush intermediate-depth earthquake, which are more than 15 times the number of events listed in the ANSS catalog. We found that the aftershock behaviors of the 2015 Hindu Kush event are similar to shallow earthquakes in many aspects, such as relatively high aftershock productivity and a rate decay following the Omori's law. Furthermore, the relocated aftershocks are consistent with the westward propagation of the mainshock rupture (Zhan and Kanamori, 2016; Poli et al., 2016a), and general observations that most aftershocks occur in the propagation direction of shallow mainshock ruptures (Kilb et al., 2003).

4.8 Supplementary figures

This section includes supplementary figures Figure S 4.1 - Figure S 4.10 that are mentioned in section 4.2-4.7.

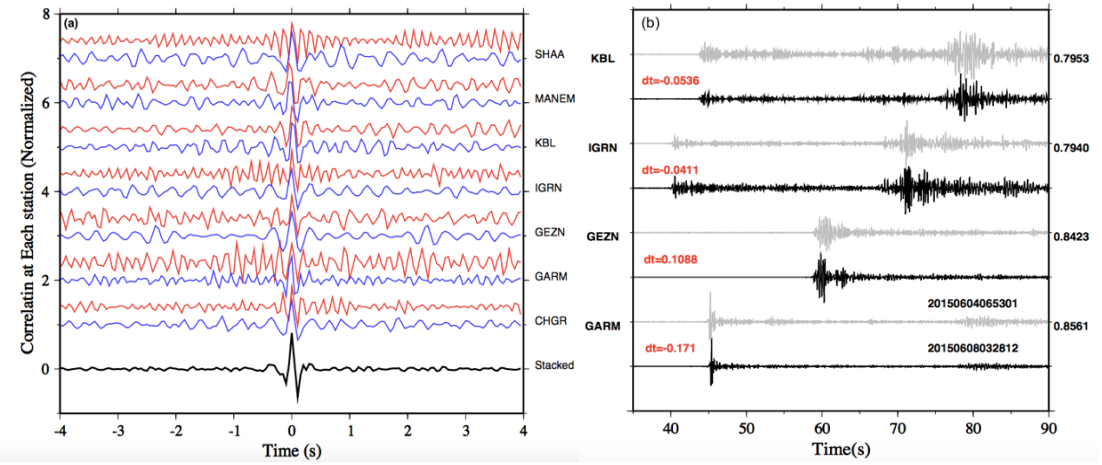

Figure S 4.1 - (a) Cross-correlation peaks of a detected event 20151026113055 at vertical component of each station and the stacked trace, red traces are P wave windows, and blue traces are S wave windows. (b) Waveforms of two events 20150604065301 and 20150608032812 with cross-correlation higher than 0.75 in a time window of [-1 2] s around P arrival, differential times are marked as dt, and the cross-correlation values are on the right.

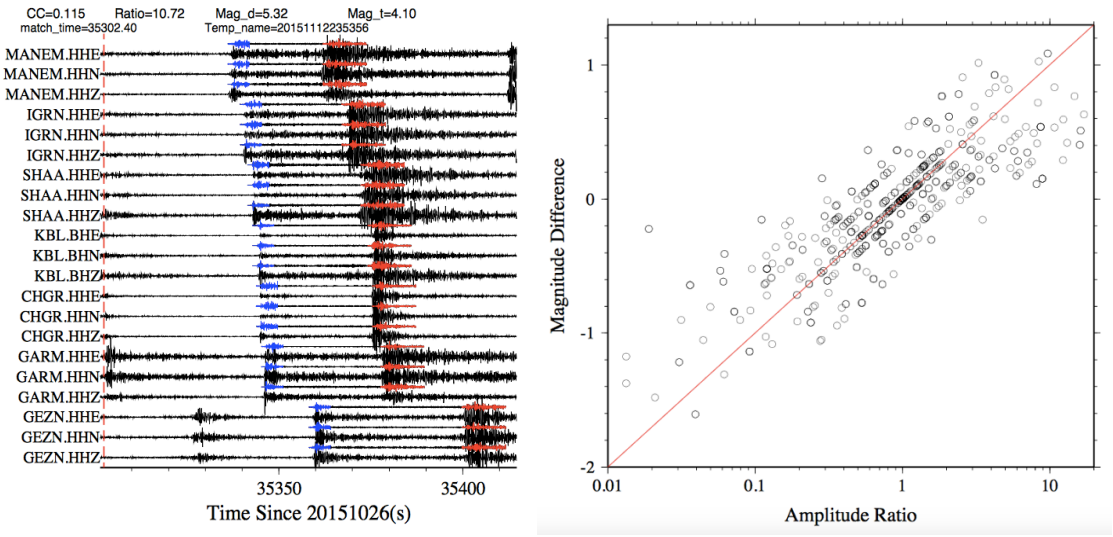

Figure S 4.2 - (a) M5.32 event detected on 10/26/2015, the template is 20151112235356. (b) Magnitude difference versus the median amplitude ratios between the templates and detected events that are also listed in the ANSS catalog.

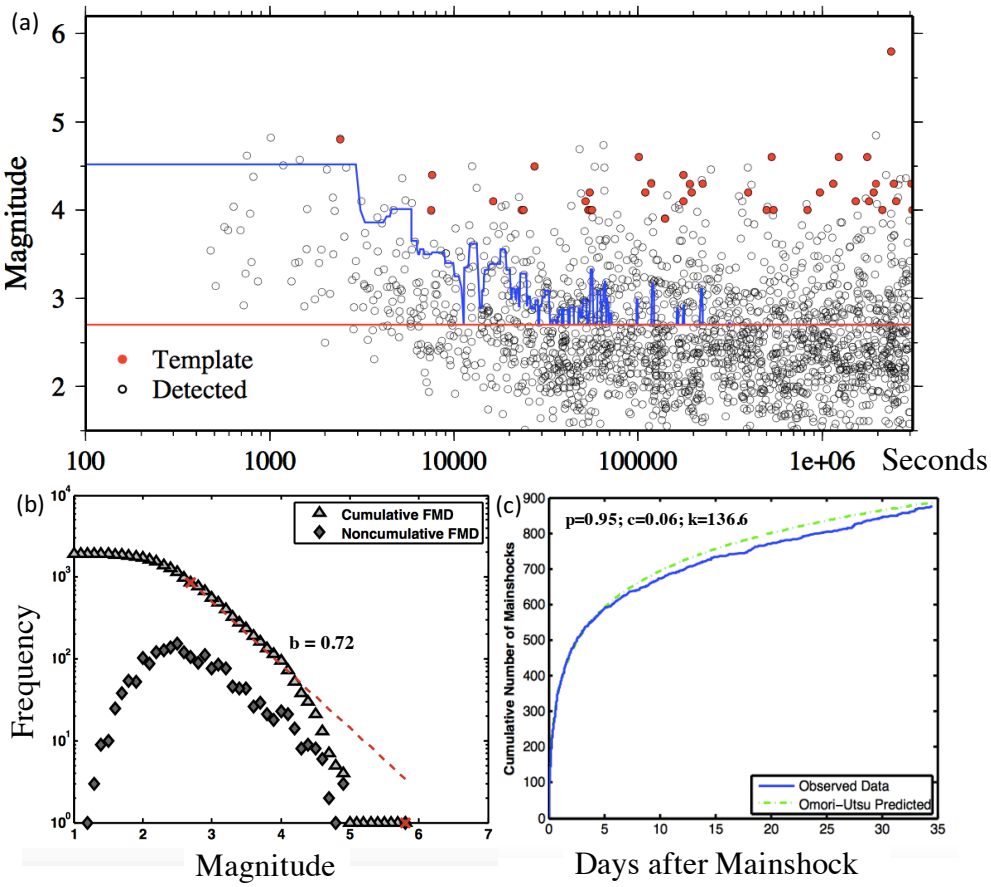

Figure S 4.3 - (a) Magnitude versus logarithmic time of detected events using threshold 12×MAD, red dots are templates, black circles are detected events, and the red solid line marks the Mc=2.7. (b) Frequency-magnitude dependence for detected aftershocks generated by ZMAP, and the red dashed line indicates the result of "Best Combination". (c) Cumulative number of aftershocks in 35 days after the mainshock, compared with the Omori-Utsu prediction.

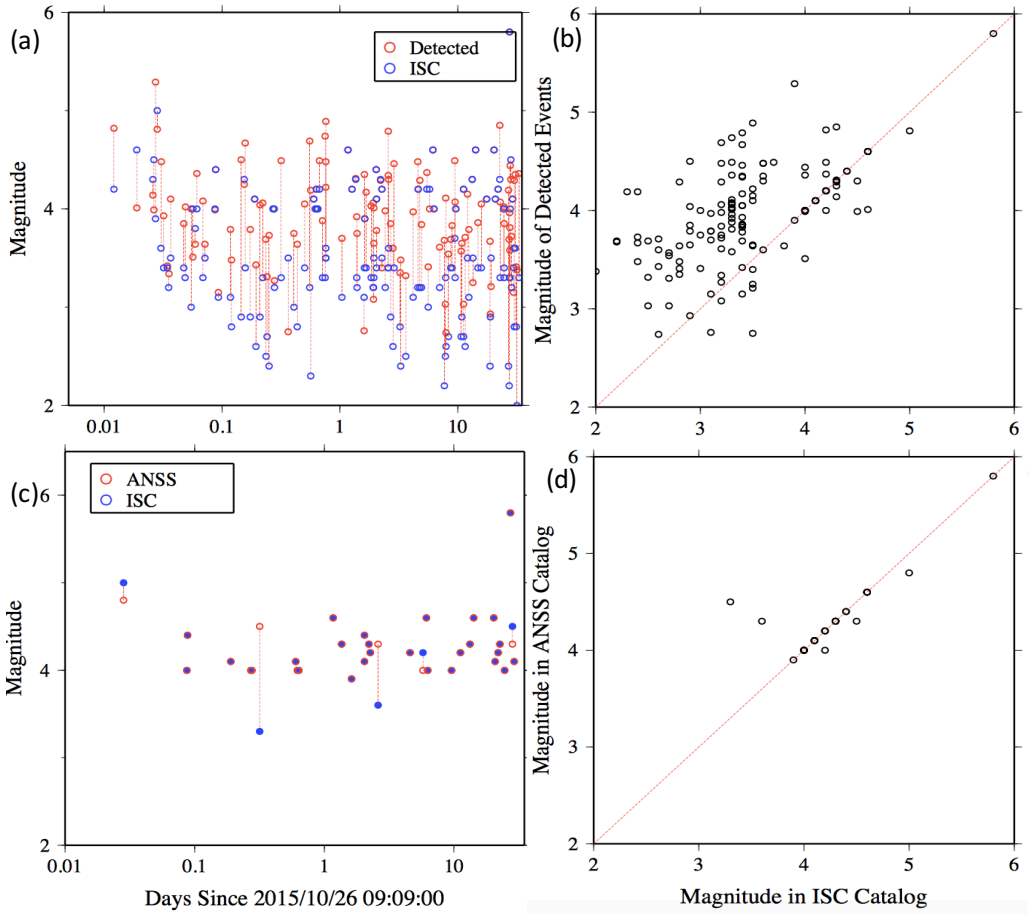

Figure S 4.4 - (a) Time-magnitude for the detected aftershock and corresponding event within 6 s on the ISC catalog, the event-pairs are connected by red dashed lines. All the aftershocks within 35 days of mainshock on ISC catalog are plotted here. (b) Magnitude difference of the same event detected and in ISC catalog. (c) the common events in ANSS and ISC catalog and their magnitude within 35 days of mainshock. (d) Magnitude difference of the same event in ANSS and ISC catalog.

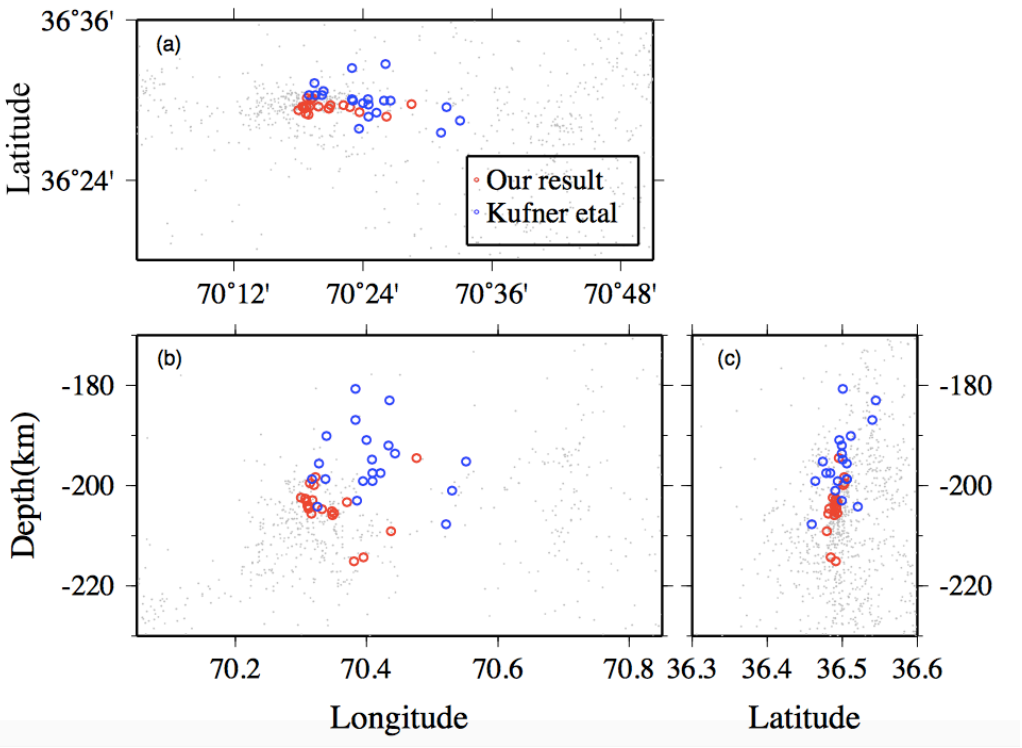

Figure S 4.5 - Relocated aftershocks in our study and Kufner et al. (2017) in (a) map view, (b) depth-longitude view, (c) depth-latitude view. Gray dots are background seismicity from Kufner et al. (2017).

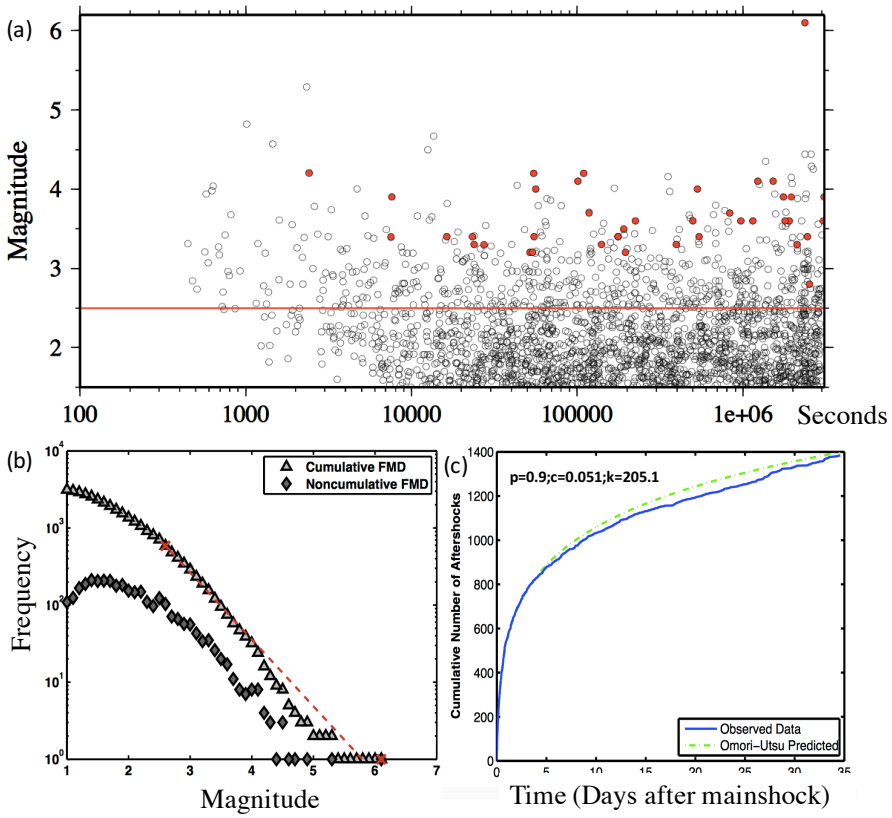

Figure S 4.6 - (a) Magnitude versus logarithmic time of detected events according to the ISC catalog, red dots are templates, black circles are detected events, and the red solid line marks the Mc=2.5. (b) Frequency-magnitude dependence for detected aftershocks generated by ZMAP, and the red dashed line indicates the result of "Best Combination". (c) Cumulative number of aftershocks in 35 days after the mainshock, compared with the Omori-Utsu prediction.

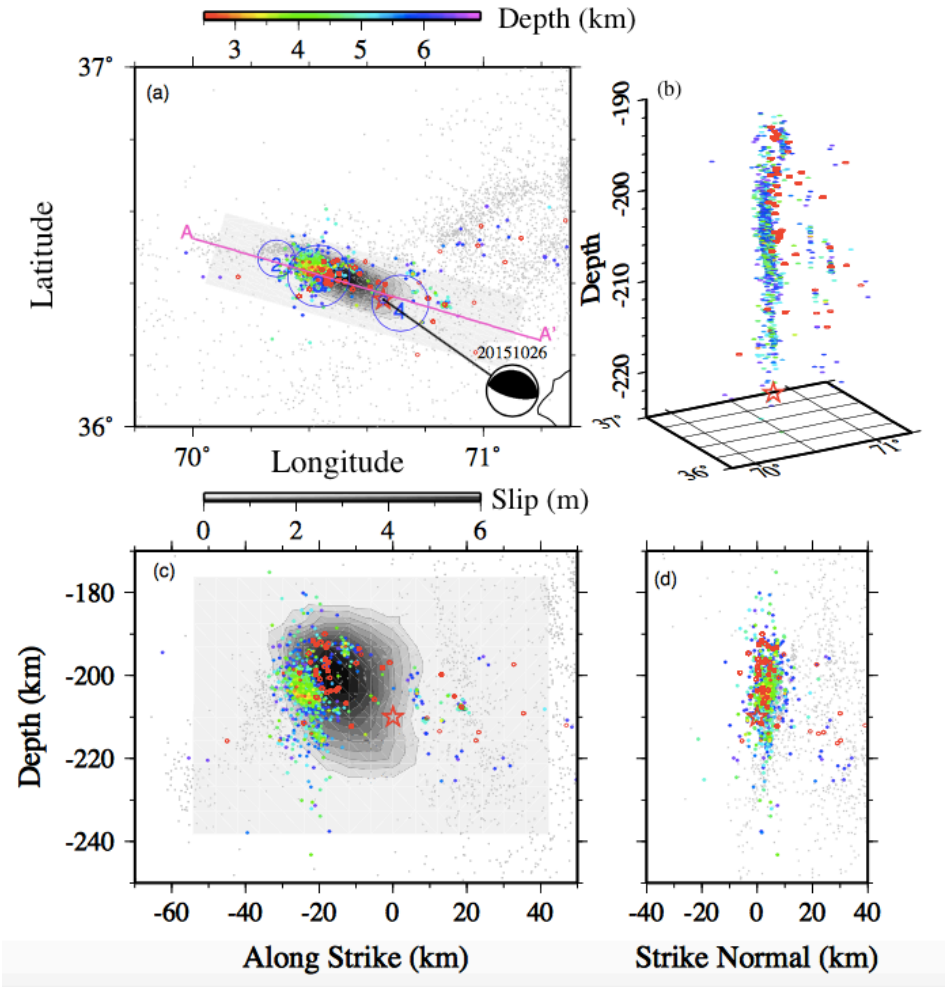

Figure S 4.7 - Same as Figure 5 (a) – (d) in main text for relocated aftershocks after shifting the initial locations 0.15º to the east, 0.1 º to the south and 5km shallower. Red circles are initial locations.

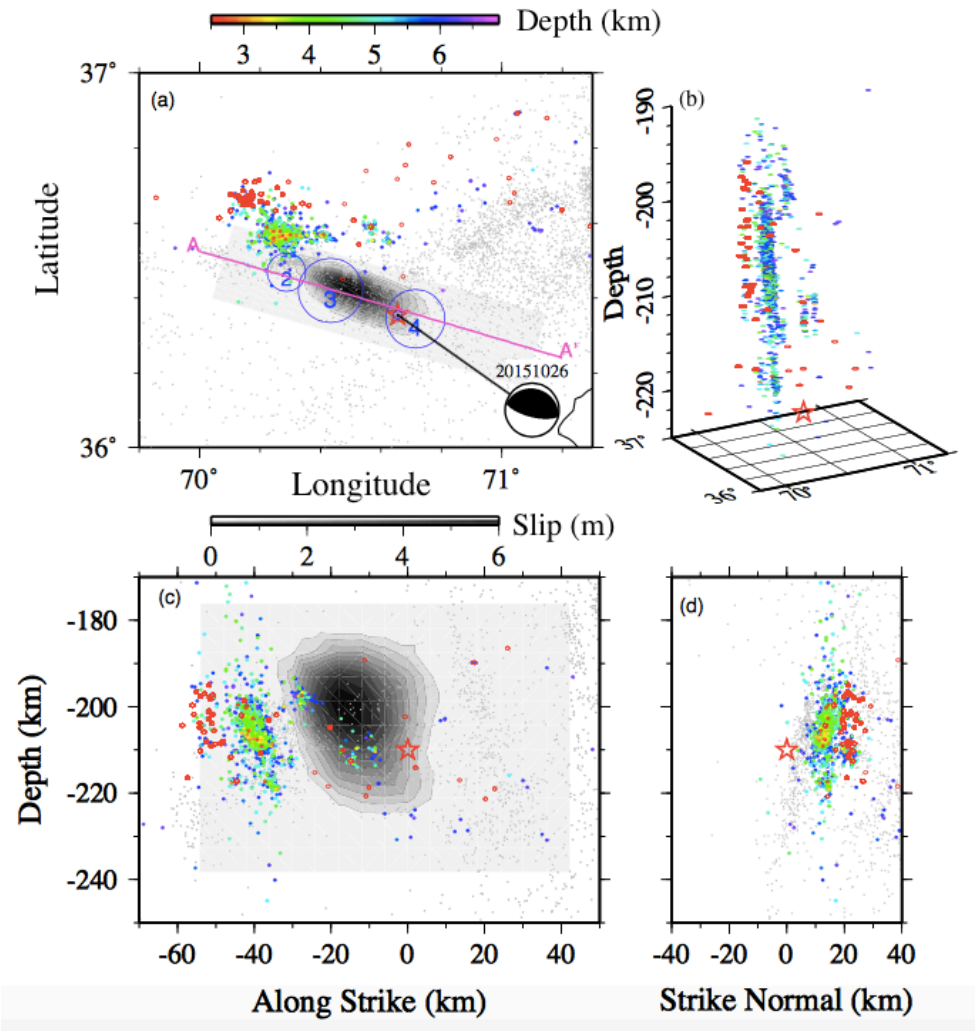

Figure S 4.8 - Same as Figure 5 (a)-(d) in main text for relocated aftershocks after shifting the initial locations 0.15º to the west and 0.15º to the north. Red circles are initial locations.

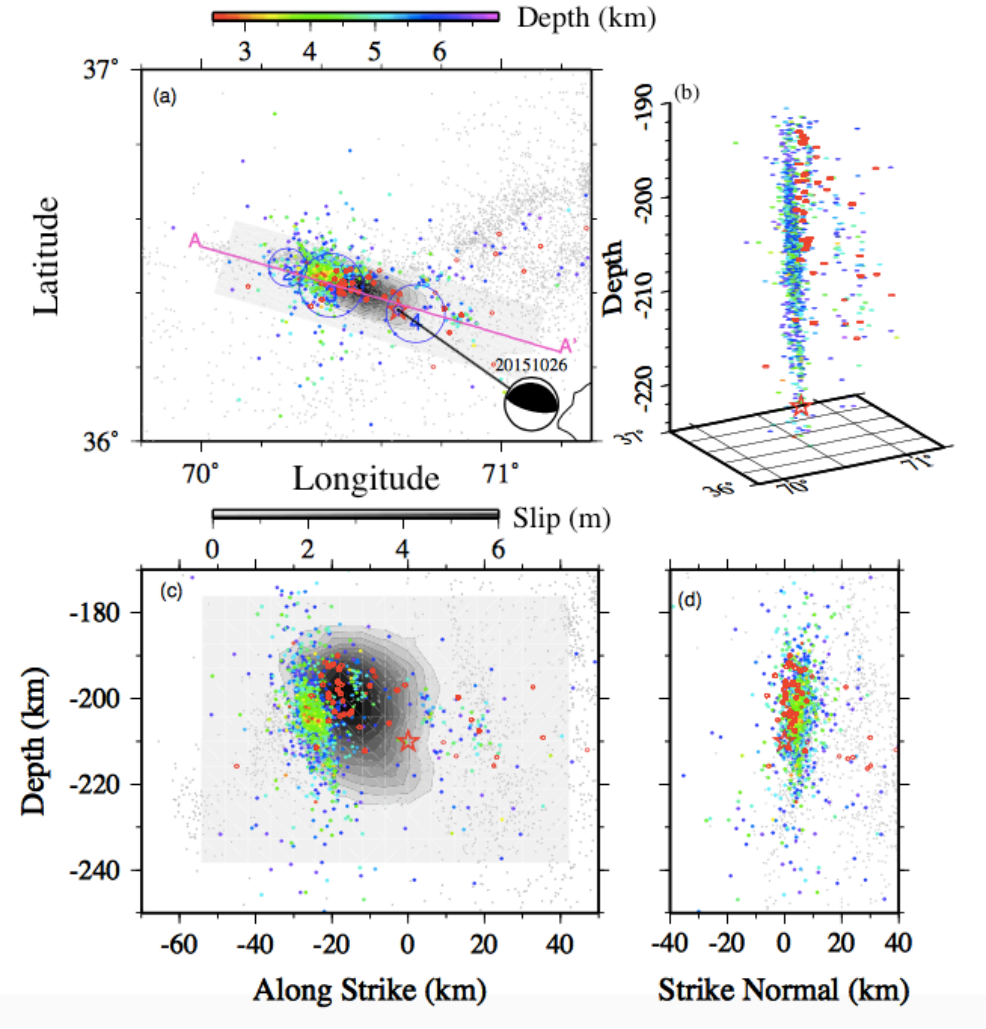

Figure S 4.9 - Noisy synthetic test after shifting the initial locations 0.15º to the east, 0.1 º to the south and 5km shallower. Red circles are initial locations.

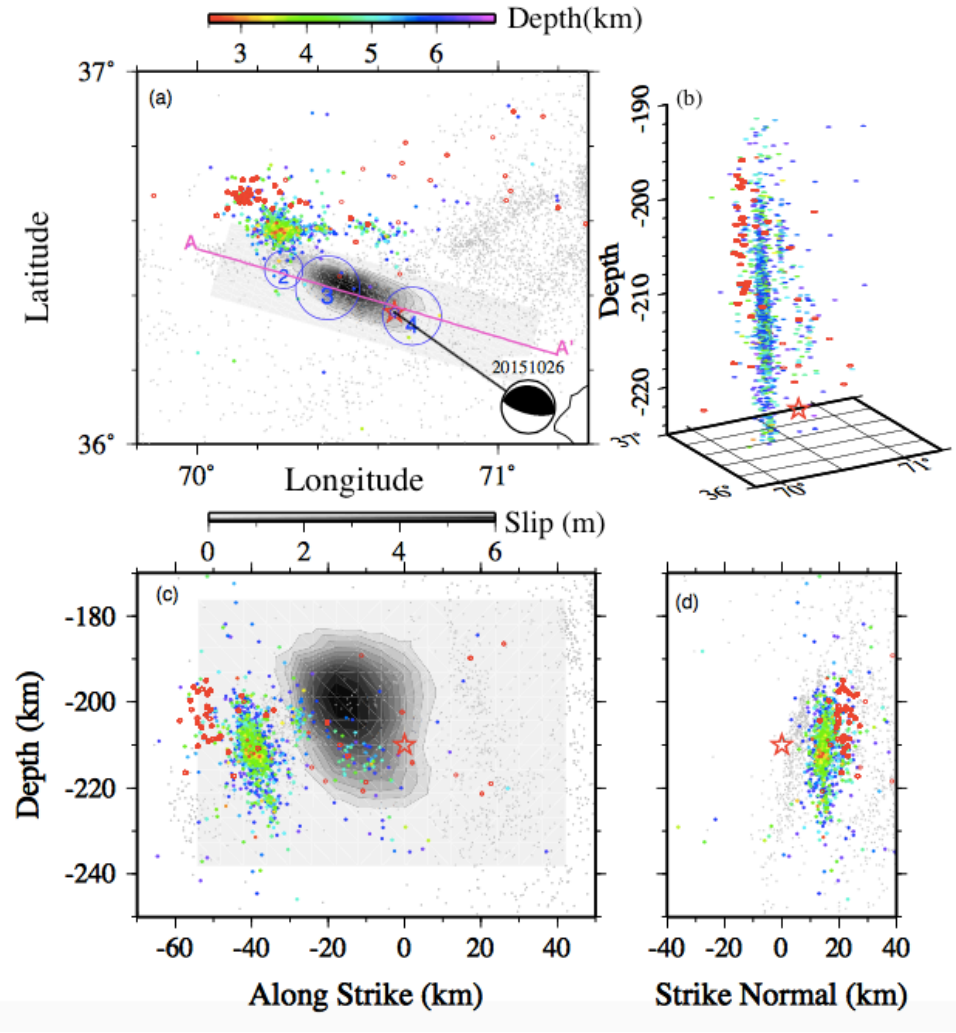

Figure S 4.10 - Noisy synthetic test after shifting the initial locations 00.15º to the west and 0.15º to the north. Red circles are initial locations.

CHAPTER 5. DETECTION OF MICROSEISMICITY AND LONG-PERIOD LONG-DURATIN EVENTS WITH LOCAL SIMILARITY METHOD IN OKLAHOMA

In this chapter I introduce a case study of using array-technique to detect seismic events in northern Oklahoma. Section 5.1-5.2 are background introduction and description of the dataset and the local-similarity seismic event detection method. Section 5.3 is focused on detection of long-duration tremor-like events, and the results are published in Li et al (2018b, SRL). Section 5.4 describes the procedure of detecting micro-earthquakes.

5.1 Summary

We examine continuous waveforms recorded by the dense seismic array deployed during IRIS Community Wavefield Demonstration Experiment, with the local similarity detection method, which is a measure of cross-correlation of waveform at each station with its nearby stations. We detected more than 1000 microearthquakes from 06/22/2016 to 07/20/2016, and majority of them are not listed on the Oklahoma regional catalog or USGS national catalogs, indicating that they are local events. We also identify 21 potential tremor-like LPLD events, some of them lasting for more than 300 s. Such events have been found at major plate-boundary faults (also known as deep tectonic tremor), as well as during hydraulic fracturing, slow-moving landslides and glaciers. However, with beamforming analysis, we find that the source locations and waveform characteristics of these events are consistent with train-generated seismic signals from the nearby Union Pacific railway. Additional evidence includes amplitude decay away from

the railway track, and similarities in frequency-time contents with other confirmed train-generated seismic signals. This case study highlights the need of dense-array observations to distinguish between natural and anthropogenic long-period long-duration seismic signals.

5.2 Introduction

Oklahoma has experienced abrupt increase of induced seismicity in the last decade. An important way to fully understand seismic activities in Oklahoma is to obtain more complete earthquake catalogs and detect different types of seismic events. The IRIS Community Wavefield Demonstration Experiment was deployed near Enid, Oklahoma in Summer of 2016. The dataset from this ultra-dense array provides an excellent opportunity for detecting microseismicity in that region with wavefield approaches.

The IRIS Community Wavefield Demonstration Experiment was deployed near the town of Lamont in North-Central Oklahoma, and the ultra-dense seismic array was recording from June 22 to July 20, 2016 (Figure 5.1). This array includes 361 three-component nodal sensors deployed as 3 lines and a 7-layer nested gradiometer sub-array, and 18 broadband stations co-located with some infrasound stations. A near North-South strike railway track is located about 10 km to the west of the dense array (Figure 5.1). We use all nodal stations for the initial event detection and broadband stations for subsequent analysis of the detected signals.

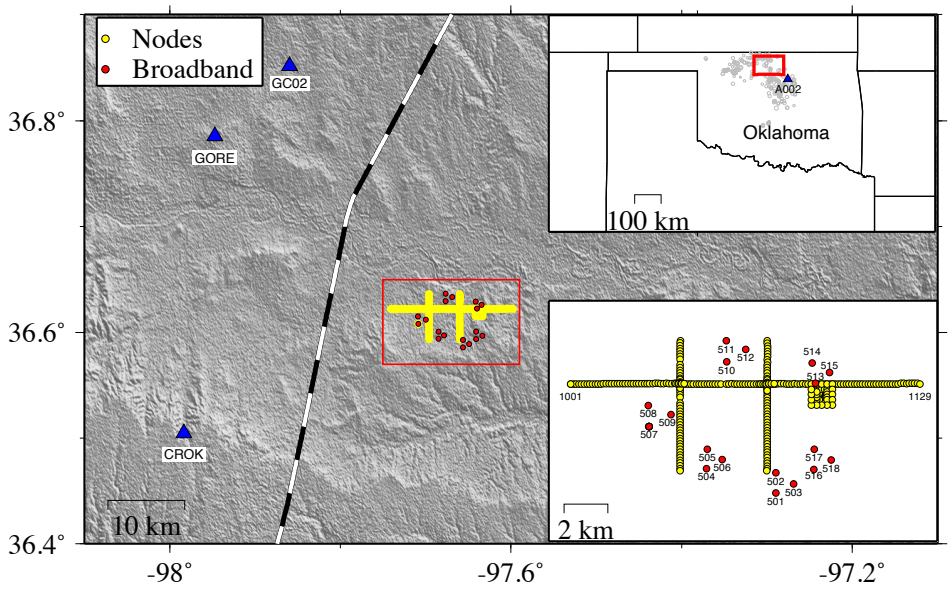

Figure 5.1 - (a) Map of the study region in North Central Oklahoma. Stations in the small box are the IRIS Community Wavefields Demonstration Experiment (YW network). The thick black-white line is the railway nearby, and triangles are broadband stations operated by Oklahoma Geologic Survey (OGS). (b) Location of the study region in the larger map of Oklahoma and nearby states. Gray dots are OGS catalog events during the study period. Station A002 is deployed by Oklahoma State University and is ~3km from a different railway. (c) A zoom-in map showing the detailed station geometry of the YW network.

We use the local similarity method (Li et al., 2018d) to detect seismic events recorded by this large-N array. The local similarity of a single station is defined as the stacked cross correlation (CC) between the record of this station and those of its 4 nearest neighboring stations. This is based on the simple fact that interstation spacing in this array is so small that the waveforms on nearby stations are very similar. After calculating the local similarities for all stations, we stack them to obtain a mean local similarity trace. For short-aperture arrays (e.g., < 20 km), the maximum time shift across the array is so small (e.g., less than a few seconds) that direct stacking of local similarity traces can be still constructive. Later we will apply grid-search and shift-and-stack for the local similarity traces for better locations of micro-earthquakes. After cross-correlating nearby

waveforms and stacking of local similarity traces, incoherent noise is suppressed and coherent signals are enhanced. Because this method does not require any prior information about the target signals, it can be used to detect unknown types of events.

Our detailed analysis procedure is described below. We first download all the waveforms recorded by the nodal stations in the Wavefield Experiment (network code YW) from the IRIS Data Management Center (DMC). We filter the data in 5-10 Hz and down-sample by a factor of 10 (from 250 Hz to 25 Hz), this frequency range is chosen to suppress regional and teleseismic signals and higher-frequency local noises (Li et al., 2018d). Next, we apply the local similarity method to the preprocessed data. We use a 1-s time window with moving step of 3 resampled data points to calculate sliding-window normalized cross-correlation (CC) between two stations. Note that the CC at a given time step is the searched maximum value over a time window length corresponding to the arrival time difference between the two stations. We then average the CC traces of one master station with its 4 nearest neighbors to obtain a single local similarity trace for the master station, and followed by stacking the local similarity traces for all the stations. With the obtained local similarity traces, we are able to detect both long-period long-duration (LPLD) and regular seismic events, and the details and results will be presented in the following sections.

5.3 Detection of Long-period Long-duration (LPLD) seismic events

5.3.1 Introduction

Deep tectonic tremors (also known as non-volcanic tremors) and low-frequency earthquakes (LFEs) are seismic events with low amplitudes, long periods and long durations, as compared to regular earthquakes of similar sizes (Obara, 2002). They have

been observed at major subduction zones and strike-slip fault systems around the Pacific Rim (Peng and Gomberg, 2010; Beroza and Ide, 2011; Schwartz, 2015, and references therein). Tectonic tremors and LFEs generally occur below the seismogenic zones where regular earthquakes occur, sometimes accompanied by geodetically observable slow-slip events (Rogers and Dragert, 2003; Obara et al., 2004). Because they are extremely stress sensitive, they are essential for understanding deep fault structures and earthquake nucleation process (e.g., Obara and Kato, 2016; Chao et al., 2017).

At shallower depth above the seismogenic zone, very low-frequency earthquakes with characteristic periods of 10-50 s have been observed along several subduction zones (e.g., Ito and Obara, 2006; Walter et al., 2011; Hutchison and Ghosh, 2016). Recent studies with ocean bottom seismometers and absolute pressure gauges also revealed long-duration tremor signals and slow-slip events in the shallow subduction-zone environments (Matsuzawa et al., 2015; Wallace et al., 2016; Araki et al., 2017). Shallow long-period long-duration (LPLD) tremor-like events have not been widely observed at major faults in continental settings, although episodic creep and slow-slip events have long been reported along several plate-boundary faults that creep at shallow depths (Linde et al., 1996; Wei et al., 2013; Schwartz, 2015; Harris, 2017). On the other hand, similar LPLD events at shallower depths have been observed during slow-moving landslides and glaciers (Gomberg et al., 2011; Helmstetter and Garambois, 2010; Winberry et al., 2013), as well as during hydraulic fracturing operations in oil fields (Kanamori and Hauksson, 1992; Das and Zoback, 2013 a, b; Hu et al., 2017).

The detection and analysis of LPLD events at shallow depths could be affected by seismic signals generated by other natural or anthropogenic sources. For example,

regional moderate-size earthquakes could be mistakenly identified as LPLD events (Caffagni et al., 2015; Zecevic et al., 2016; Chen et al., 2018). Another source of contamination is human activities, such as injection operations, nearby road traffics, trains or even air traffics (Riahi and Gerstoft, 2015; Li et al., 2018; Meng and Ben-Zion, 2018). Certain types of sources are relatively easy to identify. For example, helicopters and airplanes typically produce seismic signals with clear Doppler effects, mimicking gliding harmonic tremors during or preceding volcanic eruptions (Hotovec et al., 2013; Eibl et al., 2015; Meng and Ben-Zion, 2018). However, it is difficult to distinguish between seismic signals generated by trains and tectonic tremors during slow-slip events in several aspects: 1) they both have long durations, lasting several to several tens of minutes; 2) their dominant frequencies are in the relatively long period of 1-10 Hz (when comparing with microearthquakes of similar amplitudes); 3) sometimes they have harmonic frequency bands; 4) their sources move at a speed of several tens of kilometers per hour (e.g., Fuchs et al., 2017; Shelly et al., 2011; Hutchison and Ghosh, 2017). Hence, in search of LPLD tremor-like events, it is important to rule out potential contaminations of train-generated signals and other anthropogenic sources.

In this work, we present a case study of possible train-related LPLD tremor-like events recorded by the Oklahoma Wavefield Experiment nodal array (Sweet et al., 2018). The significant increase in small- to moderate-size earthquakes in Oklahoma since 2009 was mostly attributed to waste water injections following shale-gas developments in that region (Ellsworth, 2013; Keranen et al., 2014). Motivated by recent laboratory and field observations of tremor-type events during aseismic slip induced by fluid injections (Zigone et al., 2011; Guglielmi et al., 2015; Hu et al., 2017), our initial target was to

identify potential tremor-like signals recorded by the dense nodal array in Oklahoma (Li et al., 2017). In the following sections, we first apply a recently developed local similarity method (Li et al., 2018) to identify LPLD tremor-like signals, and then analyze their frequency content, wave speed and direction. We find that these LPLD signals are likely seismic footprints of the travelling train to the west of the array. We also present a catalog of possible train-related events during the one-month recording, which can be used as a reference for other studies with similar targets or the same dataset.

5.3.2 Data and method

In this study, we apply the local similarity event detection method to the continuous data of nodal stations in the Oklahoma Wavefield Experiment nodal array. The initial steps of data processing, waveform cross-correlation and stacking local similarity traces are described in section 5.2. With the obtained daily stacked local similarity traces for all the stations, we visually inspect the mean local similarity traces and identify long-duration events that are clearly above background noises. After identifying these LPLD events, we apply a beamforming technique to the 7-layer nested gradiometer sub-array to obtain the back-azimuths and incidence angles of these events (Rost and Thomas, 2002; Helffrich et al., 2013; Sun et al., 2015). We use this gradiometer sub-array for the beamforming analysis, as its small aperture (< 2 km) can satisfy the plane-wave assumption. Following Sun et al. (2015), we compute the Broadband Frequency-Wavenumber (BBFK) spectra of band-pass 2-8 Hz filtered waveforms using the BBFK command in Seismic Analysis Code (SAC), and obtain the wavenumber and back-azimuth with a 120-s time moving window with 50% overlap (i.e., shifting 60 s each time).

5.3.3 Results

During the one-month recording period, we visually identify 21 tremor-like events. Figure 2 shows an example of mean and individual local similarity traces on 06:00-07:00 29 June 2016 UTC (Julian day 181). We can clearly observe several sharp spikes that are local earthquakes, most of which matched with events listed in both the Oklahoma Geological Survey (OGS) catalog and newly detected micro-earthquakes with the same dataset (Nakata, 2017). In addition, there is a ~1000-s LPLD event with local similarity slightly higher than the background level (Figure 5.2a). The individual local similarity traces (Figure 5.2b) also show such long-duration event in the first half-hour. A total of 4 LPLD events have been identified on that day (Figure 5.2c), together with many earthquake-like signals.

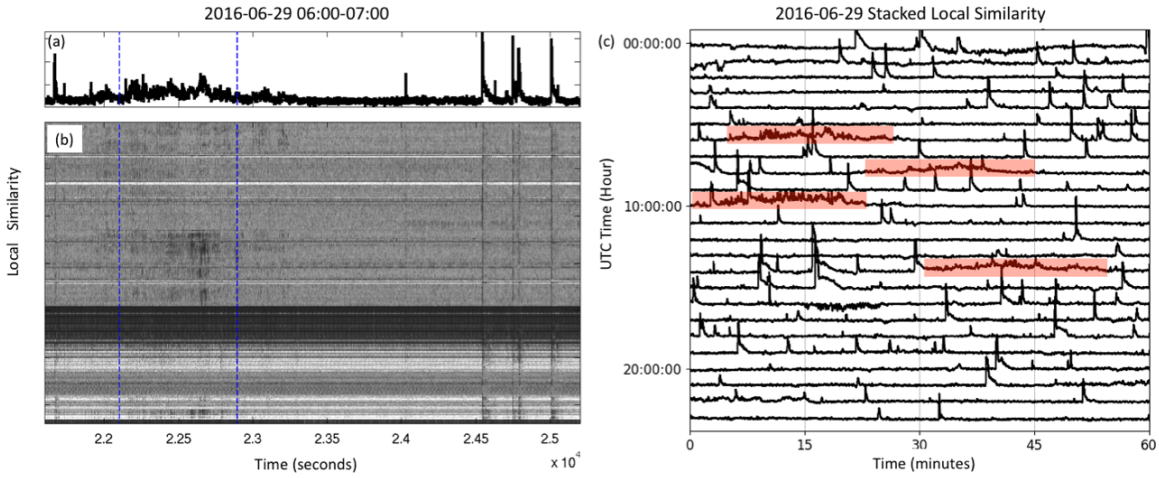

Figure 5.2 - (a) 1-hour mean local similarity trace of all the nodal stations during 06:00-07:00, 06/29/2016. The visually-identified long-period long-duration (LPLD) event is marked within two dashed lines. The vertical spikes mark local microearthquakes. (b) local similarity trace at individual station. (c) Hourly mean local similarity traces on 06/29/2016. Four visually identified LPLD events are marked in small boxes.

Next, we compute the spectrogram of the same LPLD event recorded by the broadband station 508. In addition to a few vertical stripes, the majority of the tremor-like

signals show clear harmonic frequency contents (Figure 5.3). We observe a gradual increase and decrease in frequency over time, which is also shown for other events, and recorded by the nodal station for the same event (Figure 5.4). Such harmonic frequency contents and temporal variations are similar to other confirmed cases of train-generated signals (Fuchs et al., 2017; Quiros et al., 2016; Chen et al., 2004), and a broadband seismic station deployed ~3 km of a different railway track in Morrison, Oklahoma (Figure 5.4).

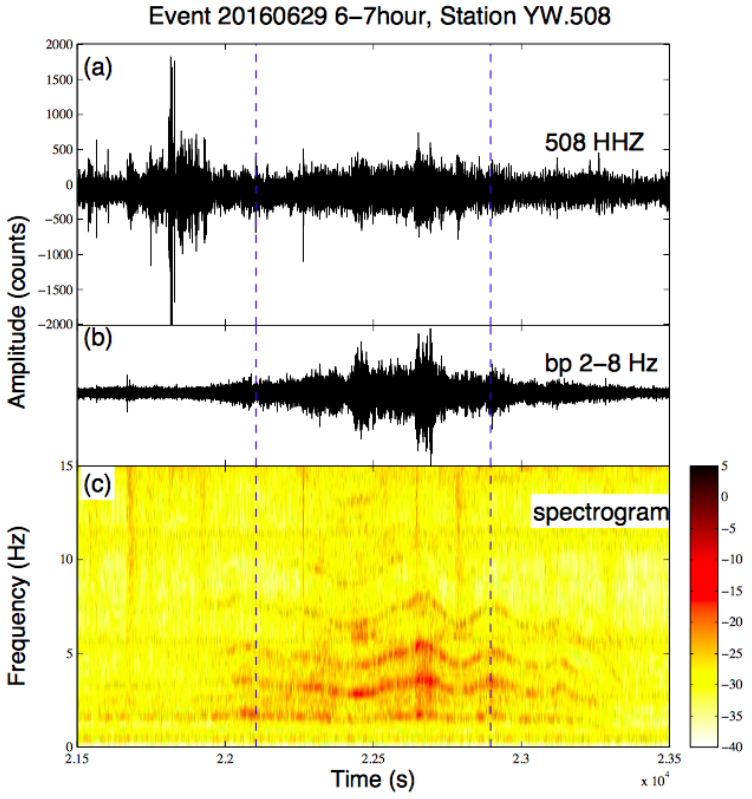

Figure 5.3 - (a) Raw waveform, (b) 2-8 Hz band-pass filtered, (c) spectrogram of the same LPLD event shown in Figure 5.2 and recorded by the broadband station 508.

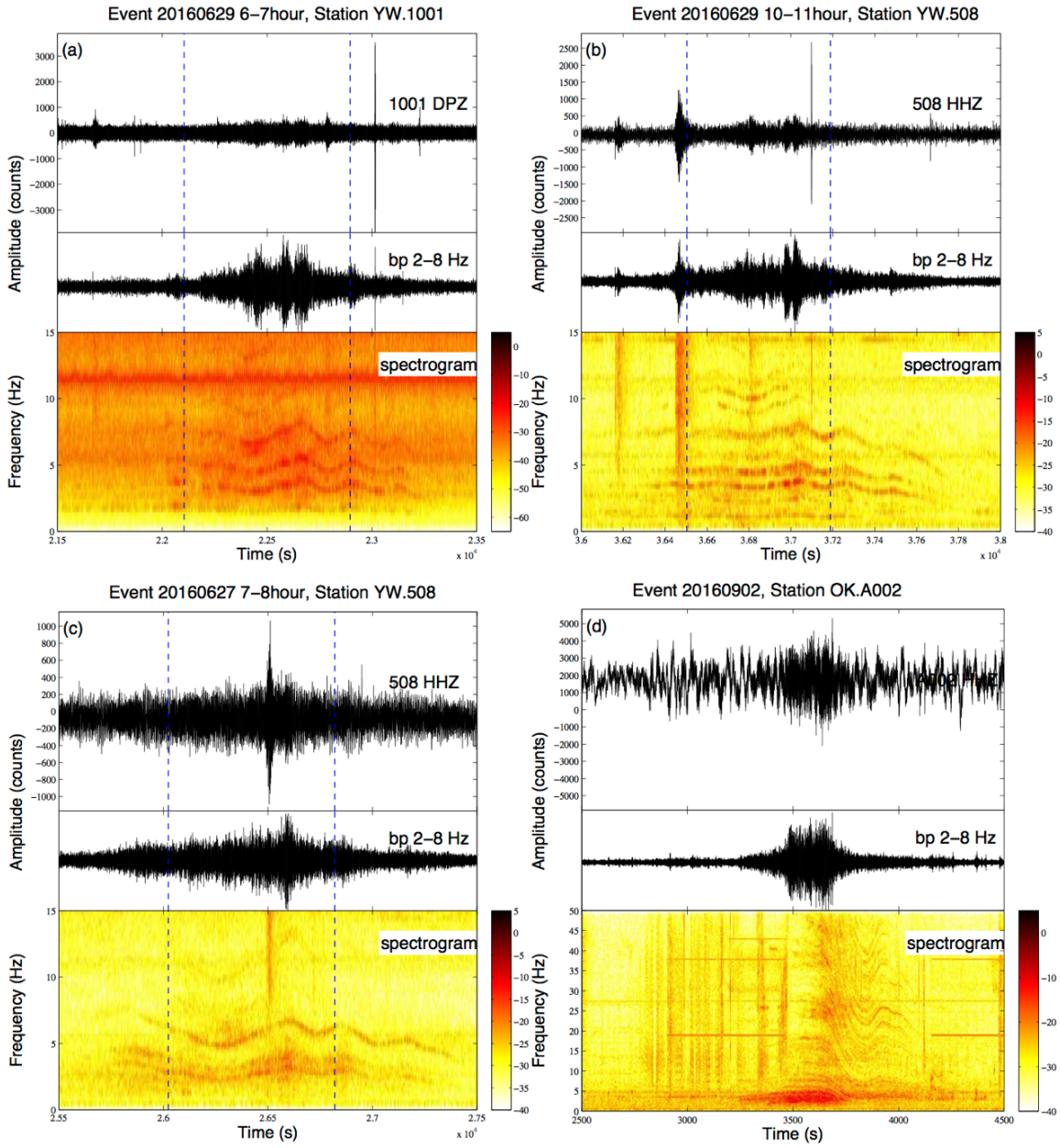

Figure 5.4 - More examples of possible train-generated seismic signals. (a) Same event as in Figure 5.3 recorded by a nodal station 1001. (b) An event on 2016/06/27 recorded at the broadband station 508. (c) An event on 2016/06/29 recorded by the broadband station 508, (d) Known train-generated seismic signals recorded at a station A002 within 3 km of another railway in Morrison, Oklahoma.

We then obtain the back-azimuth and wavenumbers from the beamforming analysis on 05:00-07:00, 29 June 2016 (Figure 5.5). The time window corresponding to the LPLD event delineates a moving source with back-azimuth changing from 305° to

250°. The frequency–wavenumber (f-k) amplitude (beam power) contour of several time-windows during the LPLD event can be found in Figure 5.6. Based on the relationship between wavenumber k and horizontal slowness p, we estimate the apparent velocity $c_{app} = \frac{f}{k} = 1.36\ km/s$, where $f = 3.5\ Hz$ is the dominant frequency, and $k = 2.58\ cycle/km$is the wavenumber obtained from peak BBFK spectra (Helffrich et al., 2013). Furthermore, we estimate the incident angle $\theta = 61.92°$ by $c_{app} = c/sin\theta$, here we assume $c = 1.2\ km/s$, an average surface shear-wave velocity in Oklahoma (Fletcher et al., 2006). The relatively large incident angle suggests that this LPLD event is likely from a shallow source.

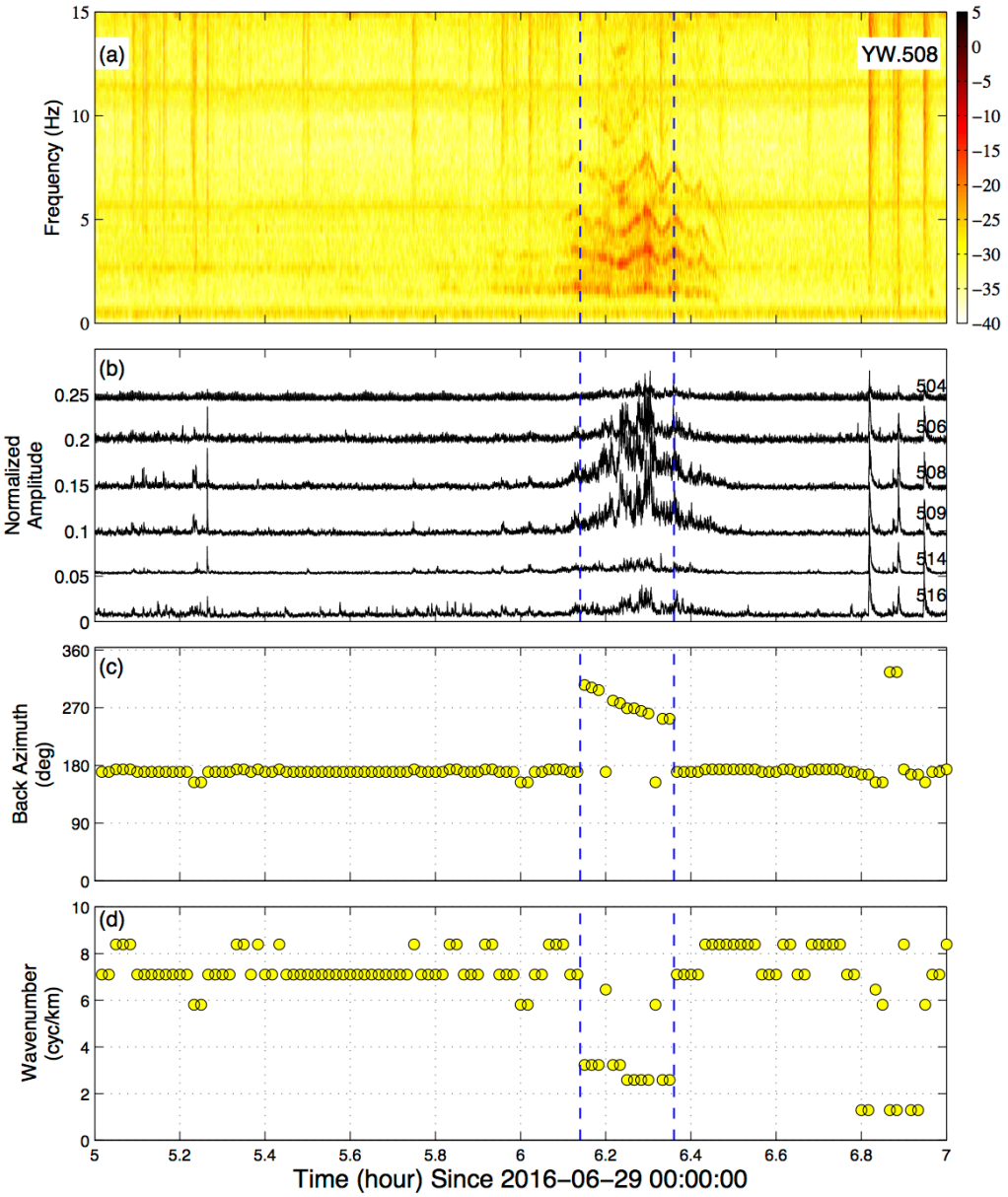

Figure 5.5 - An example showing the BBFK array analysis for the same LPLD event as shown in Figure 5.2. (a) Spectrogram, (b) 2-8 Hz band-pass-filtered envelope function, (c) back-azimuth, (d) wavenumber of waveforms during 05:00-07:00, 06/29/2016. The approximate time window of LPLD event is marked as vertical dashed lines.

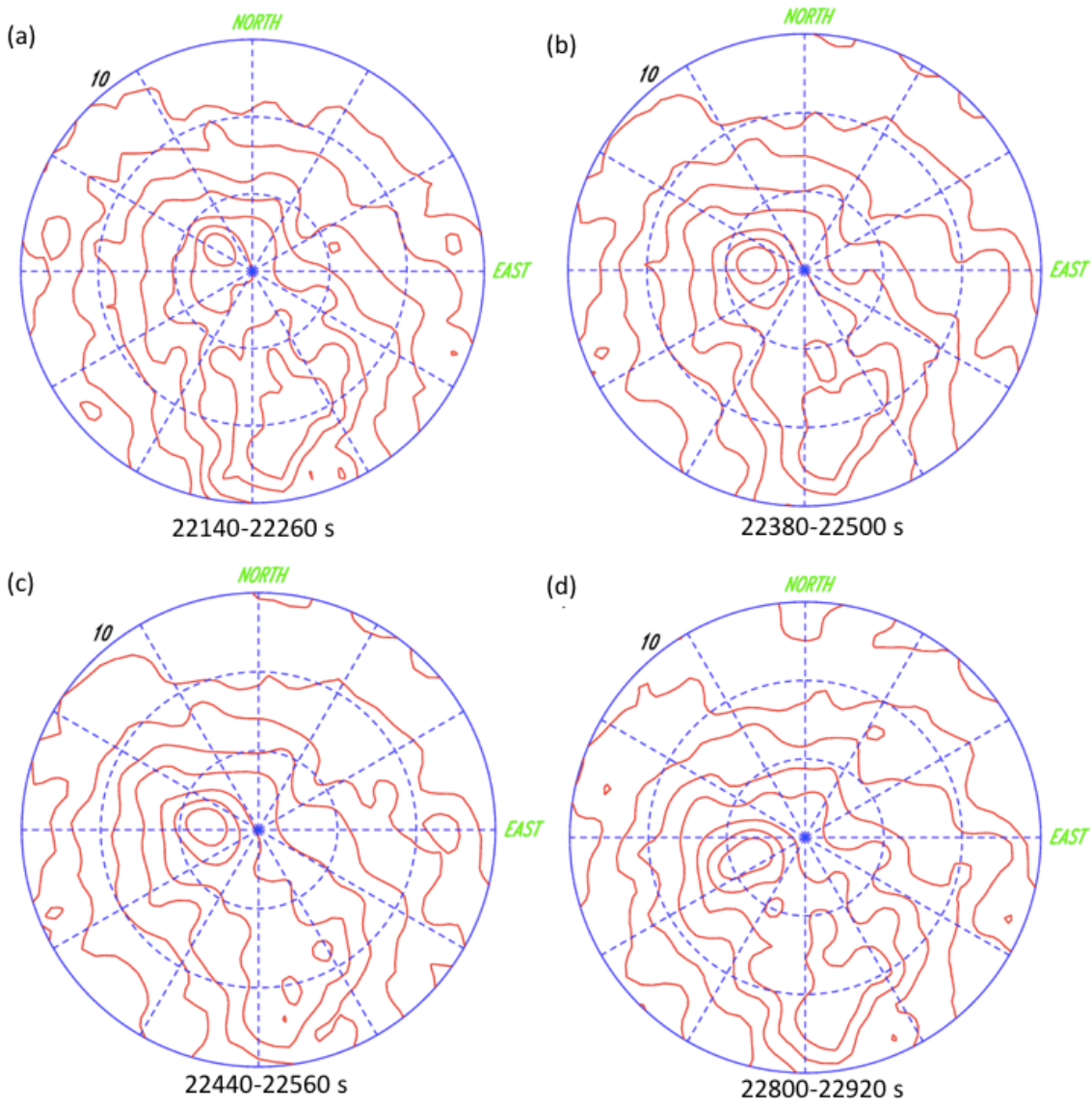

Figure 5.6 - The contour plot denoting the distribution of frequency–wavenumber (f-k) amplitude (beam power) as a function of back azimuth (angle) and wavenumber (radius) for different time windows.

Figure 5.7a shows the 2-8 Hz band-pass filtered waveform of the LPLD event recorded by selected stations from the horizontal seismic line with a constant spatial interval. The amplitudes of the tremor-like signals decay systematically from west to east. To better quantify whether the signals are originated from passing trains on the nearby railway, we compute the sum of the squared velocity between 22140 and 22980 s relative

to 06/29/2016 00:00:00 (06:09:00–06:23:00, 29 June 2016), which are the starting and ending time obtained from beamforming analysis, and use it as a proxy for radiated seismic energy. As shown in Figure 5.7b, the squared velocity sum decay roughly follows a log-linear relationship with d, where d is the shortest distance from the railway track. We compare the decay rate with body wave decays of surface sources following the decay rate of $A = d^{-3/2}\exp\left(-\frac{\pi f d}{Qv}\right)$, where we assume $f = 5Hz$, $v = 1.2\ km/s$, and the term $\exp\left(-\frac{\pi f d}{Qv}\right)$ is a result of attenuation. We find that the attenuation factor Q between 50-150 provides a good fit to the curve (Figure 5.7b).

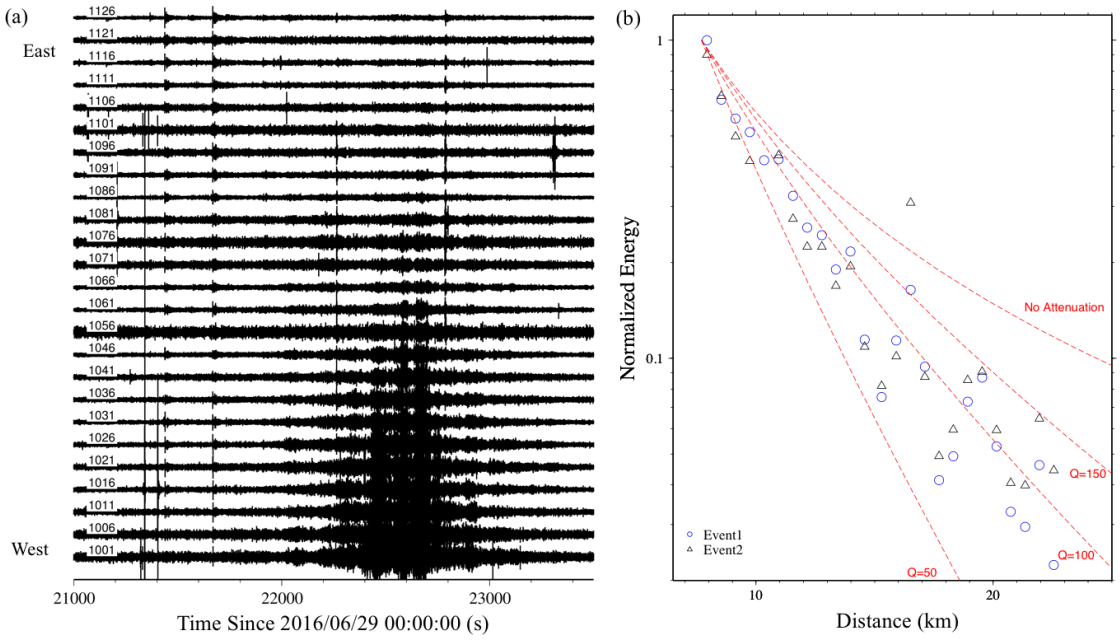

Figure 5.7 - (a) Band-pass 2-8 Hz waveform of same event as in Figure 2a recorded by some nodal stations in the horizontal seismic line with an equal station spacing. (b) Normalized energy versus distance from the train track for two LD events showing similar decay across the array.

The cumulative energies of two events at all nodal stations are shown in Figure 5.8. Figure 5.7 and Figure 5.8 indicate that stations in the western side have generally higher energy than the eastern side, consistent with westward location of the railway.

Generally the signals become visually undetectable on stations with distances larger than ~15 km from the railway. To demonstrate the moving source has little effect on the decaying of energy, we use a smaller time window of 120 s (with 60 s overlap) and re-calculate the normalized energy with distances. As shown in Figure 5.9, we do not observe any clear change in the decay rate with time, suggesting that the moving source did not affect this calculation.

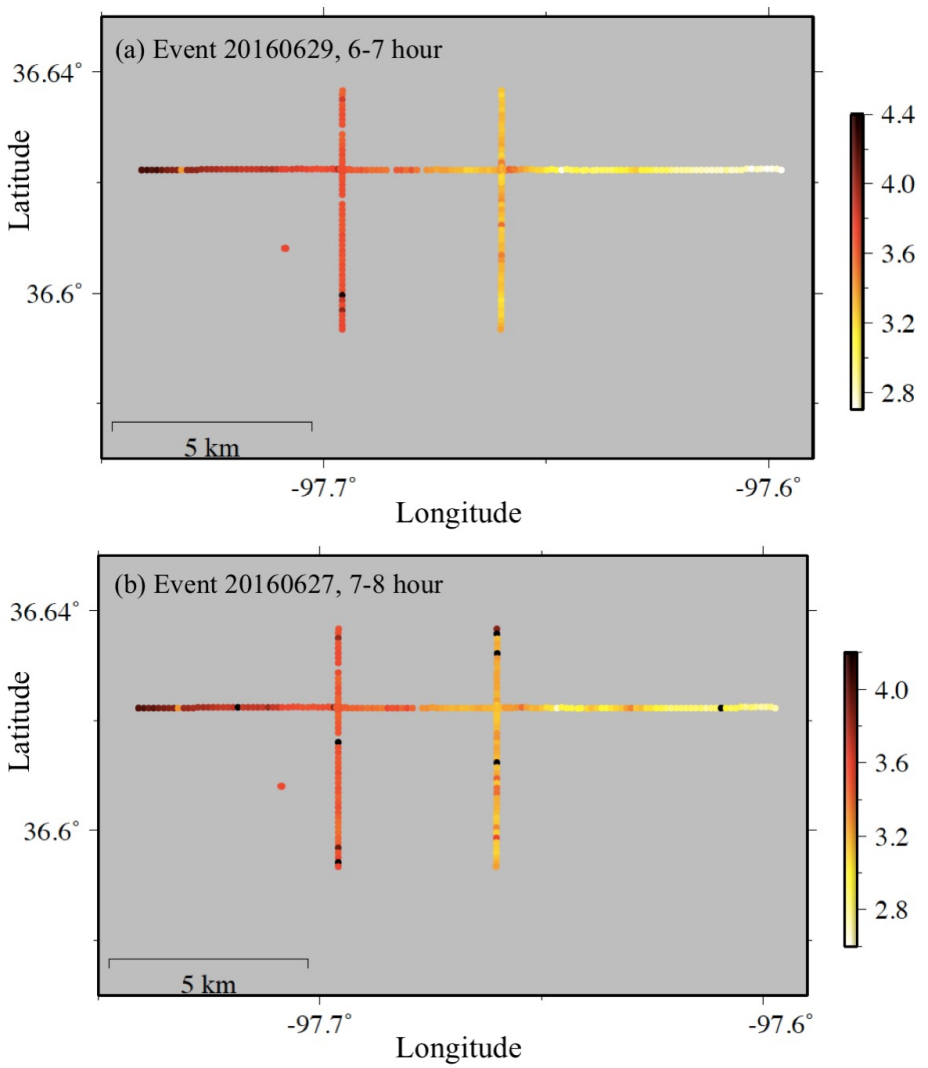

Figure 5.8 - Calculated energy across the array for LPLD events on (a) 2016/06/29, 06:00-07:00, and (b) 2016/06/27, 07:00-08:00.

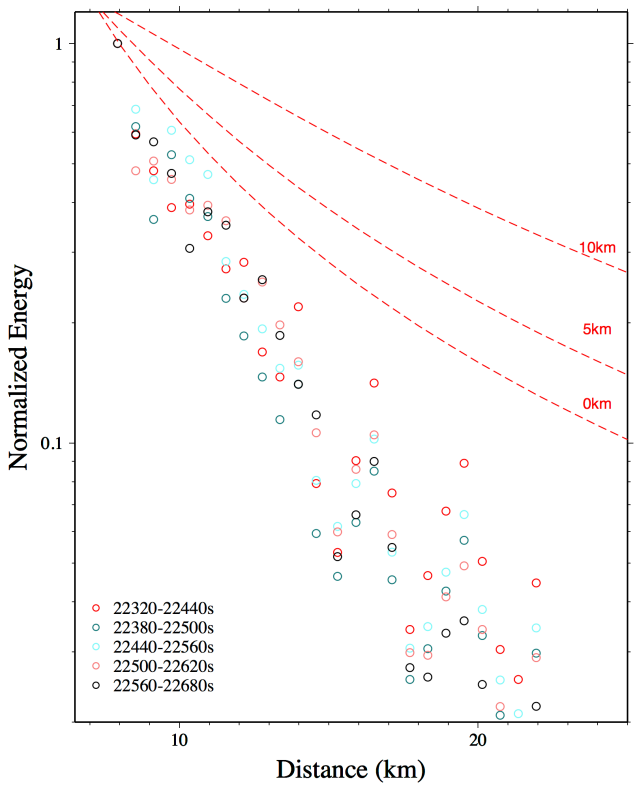

Figure 5.9 - Decay of cumulative energy in different 120s windows from 22320s to 22680s, with overlap of 60s.

5.3.4 Discussion

Recent studies have shown that hydraulic-fracture operations could induce LPLD tremor-like events (Das and Zoback, 2013a, b; Hu et al., 2017). Although some LPLD events in their studies might be small regional earthquakes (Caffagni et al., 2015; Chen et al., 2018), the characteristics of the LPLD events observed in this study are different from any of them. For example, the duration of our detected LPLD events are more than 300s, much longer than the typical duration of 30-60s for the LPLDs in the other studies. Furthermore, the dominant frequency of our LPLD events is less than 10 Hz, whereas the LPLD events during hydraulic fracturing can reach up to 60-100 Hz (Das and Zoback, 2013a, b; Hu et al., 2017; Chen et al., 2018). These differences suggest that the source

mechanisms of LPLD events observed in this study are different from those recent observations near hydraulic fracturing sites.

Detailed analysis of the waveforms and spectrograms of these LPLD events revealed they are seismic footprints of traveling trains along a Union Pacific (UP) railway 10-20 km to the west of the array. The first supporting evidence is that the spectrogram of the LPLD event shows harmonic frequency bands and the Doppler effect, which is a typical feature for train signals (Quiros et al., 2016; Chen et al., 2004). We note that the harmonic frequency bands in other studies are much higher, which is likely due to the much longer source-receiver distance (~10 km) in this work than the distances in their studies (~300 m). Fuchs et al. (2017) suggested that track or wheel irregularities and static axle load are main mechanisms of vibrations generated by trains. Wheel irregularities represent moving source and would have Doppler effect, while axle load are quasi-static and explains constant spacing between spectral lines. The overtones with increasing and decreasing frequencies and spectral lines with constant spacing observed in our study could be a combination of multiple wheel regularities and axle loads.

The beamforming analysis on the ultra-dense gradiometer sub-array shows moving sources from north to south, west of the sub-array for most LPLD events, and 1~2 events moving from south to north, both consistent with the azimuths of the railway. Assuming that the source is on the railway, we estimate the source to move at a speed of ~80 km/h, which is also comparable to a typical freight train speed. Unfortunately, the detailed schedule on the UP railway is not openly available at this stage. Hence we cannot confirm our observation with known train schedule. Comparison with seismic data

recorded by stations very close to the railway would also provide additional information about the passage of train-signals and the decay of seismic signals with distances.

In regions where seismic arrays are exposed to heavy cultural noises (trains, highways, helicopters, wind turbines, etc.), it is possible that the corresponding seismic signals might be mislabeled as natural events, such as LPLD tremor events or micro-earthquakes (Riahi and Gerstoft, 2015; Meng and Ben-Zion, 2018). Hence, we need to be cautious when analyzing seismic data in these regions (e.g., Hutchison and Ghosh, 2017). There are also some other types of anthropogenic noises in our study region. For example, the beamforming shows a constant back-azimuth around 180°, and we believe this is from noise of a nearby wind farm located to the south of the array (Stammler and Ceranna, 2016). We rule out the possibility that our detected LPLD events are from signals generated by wind turbines for the following reasons: the location of LPLD events start from northwest to the ultra-dense array, which is different from the locations of wind turbines. The occurrence time of the LPLD events did not show any correlation with the hourly wind speed. In addition, the wind turbines are evenly distributed from west to east, so it is not likely to cause a higher cumulative energy on the western part of the array.

Finally, the observation of energy is compatible with the assumption that the source of the signal is from the vibration of trains on the nearby railway. The decay rate of energy across the linear array perpendicular to the railway fits well with body wave decay considering near-surface attenuation from sediments. In addition, we did not find any events with higher energy in the eastern side of the array, indicating the signals persistently come from the west.

5.3.5 Conclusion

In this study we detected 21 LPLD tremor-like events in Oklahoma from seismic data collected by the IRIS Community Wavefield Experiment array. Our subsequent analysis revealed that they are most likely generated by moving trains along a nearby railway, rather than generated by slow slip induced by hydraulic fracturing or waste-water injections. We came up with a catalog of train-related LPLD events identified with both local similarity and beamforming methods, and the stacked local similarity trace for all 30 days. These possible train-related signals could be used as a potential labeled dataset for future automatic detection/classification of similar signals in this and other regions.

5.4 Detection of micro-seismicity with ultra-dense array

5.4.1 Introduction

With the local-similarity method, we could further exploit the IRIS Community Wavefield Experiment array dataset to detect very small earthquakes that are missing by regional networks. It provides an opportunity to obtain precisely spatial distribution of microearthquakes to illuminate subsurface fault structures. Furthermore, the travel times of micro-earthquakes in the nodal array could serve as basics of high-resolution seismic imaging. In this study, we mainly focus on detecting and locating microearthquakes with the IRIS Community Wavefield Experiment nodal array.

5.4.2 Method

Similar to data processing described in section 5.3.2, we first band-pass filter continuous waveform with 2-12 Hz, and convert daily recording on all the stations to local-similarity traces. To achieve the goal of locating detected micro-earthquakes, we

incorporate beamforming and time-shifting from predicted travel times in the local similarity method to obtain coarse locations of these events, and then pick station-wise arrival times around the detections and further relocate them. We set up $1km \times 0.5km \times 1km$ 3D grids as initial locations of detected events (Figure 5.10a). Then the travel time tables for each grid are computed with a 1D velocity model, and the time of local-similarity traces are shifted according to the travel-time table and stacked. If the location of the grid is close to the true location of an event, the shifted and stacked local-similarity would have the highest value on the arrival time (Figure 5.10b). After computing the MAD of all the shifted-and-stacked local similarity traces for all grid points, we keep the data point with the highest MAD as the true detection.

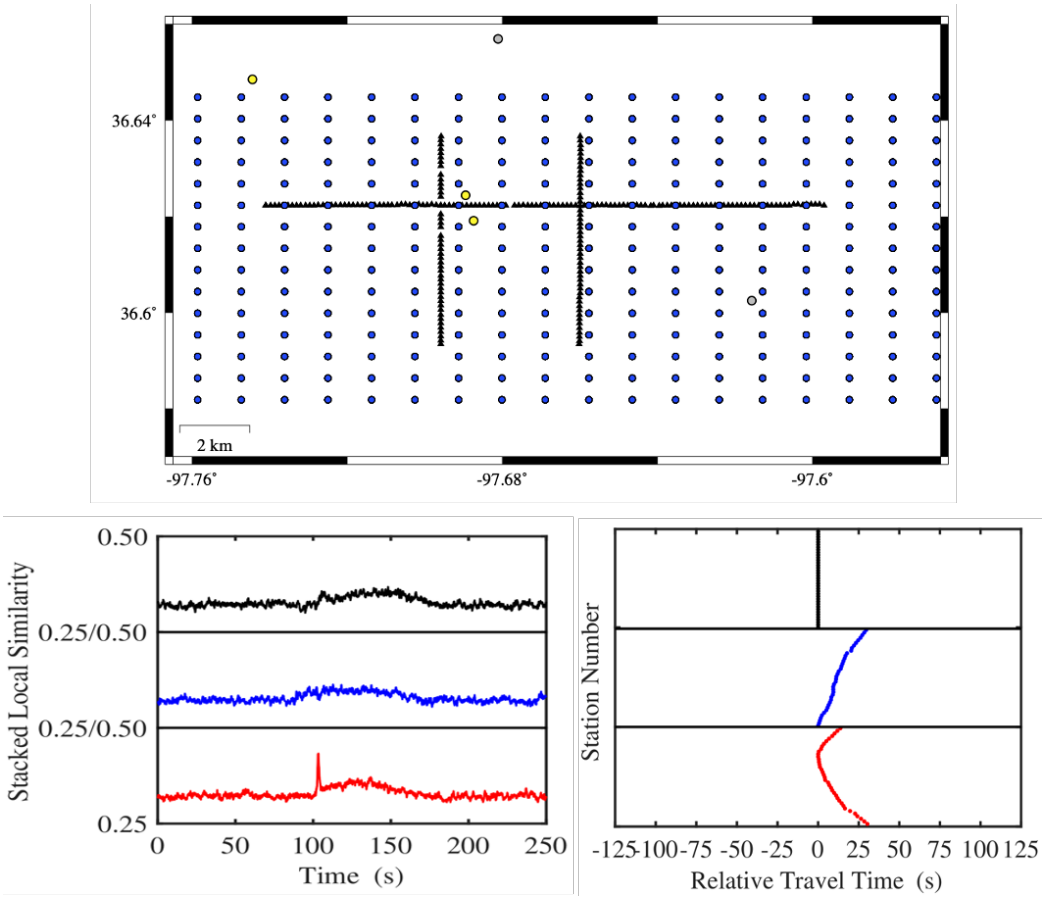

Figure 5.10 – (a) Initial setup of 3D grids, solid blue dots are the 3D grids, black traingles are nodal stations, gray dots are earthquakes on the Oklahoma Geological Survey (OGS) catalog (Walter et al., 2020) during the study period, yellow dots are earthquakes detected by a matched-filter technique with state-wide network (Skoumal et al., 2019). (b) Stacked local similarity with different time shift according to source locations, and the corresponding predicted arrival time table.

5.4.3 Results

Figure 5.11 shows two examples of waveforms and stacked local similarities. The first one is a M=2.0 earthquake on 07-11, 2016 located southeast to the intersection between seismic lines 1 and 2 (Figure 5.12). Its arrival times exhibit hyperbolic move-outs across the array. The second event is likely a small earthquake outside of the dense array, not listed in either the OGS catalog or the matched-filter catalog in Oklahoma (Skoumal et al., 2019).

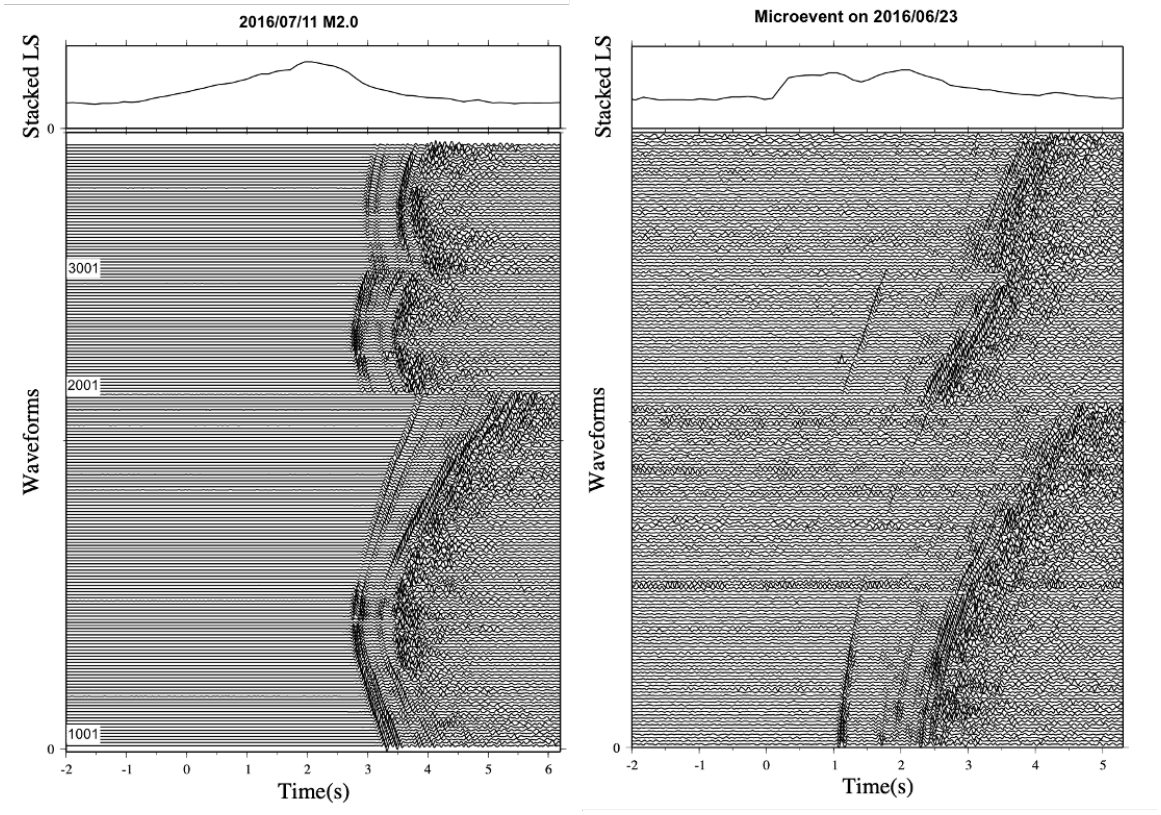

Figure 5.11 - Waveform and stacked local similarity (LS) of two detected events, one M2.0 earthquake on 2016/07/11, another is a new microearthquake not listed on the catalog.

The beamforming & local-similarity method detects more than 1000 events in total, and our next step is to relocate them. We cross-correlate waveforms around predicted arrival times for every 5 stations in the seismic lines, and the time differences are used as inputs for the double-pair double-difference (DD) relocation technique (Guo et al., 2017). The locations of 700 detected earthquakes are displayed in Figure 5.12. Although the distribution of events are scattered around the network, there are a few linear patterns (marked as dashed lines) that likely reveal small fault lines in this region.

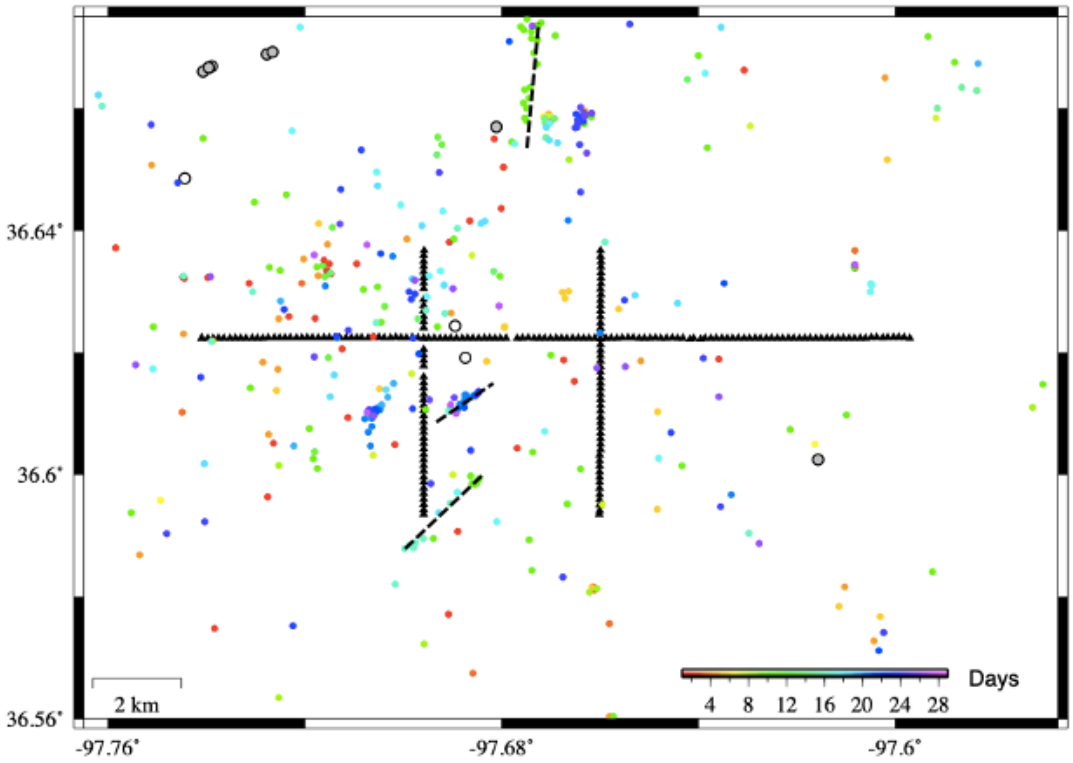

Figure 5.12 - Preliminary result for about 700 relocated events with the Double-difference TomoDD technique. Color indicates days since 2016/06/22.

5.4.4 Summary and future work

We detected and located 700 microearthquakes during the 1-month deployment of nodal array in IRIS Community Wavefield Experiment. These events can be used as templates for the matched-filter technique, and applied to the broadband recordings deployed for more than 3 months. In collaboration with a graduate student Qiushi Zhai in our group, we plan to expand the detection and refine the arrival times and improve locations of all events. This work demonstrates the workflow of seismic event detection with no prior-knowledge of existing events with a large-N array.

CHAPTER 6. TRANSFER LEARNING WITH CNN-BASED PHASE-IDENTIFICATION CLASSIFIER (CPIC)

In this chapter, I present a case study of transfer learning with a CNN-based Phase-Identification Classifier (CPIC) model. In this study, we demonstrate the possibility to apply the CPIC model trained in Wenchuan, China to different geographical regions. The work has been presented in the 2018 AGU annual meeting (Li et al., 2018c).

6.1 Introduction

Machine learning algorithms have become a powerful tool in different areas of seismology, such as earthquake detection/location, earthquake early warning, seismic event classification and signal denoising (e.g., Bergen et al., 2019; Kong et al., 2019). Deep learning, especially convolutional neural networks (CNN) have been applied to continuous seismic waveform recordings to perform efficient phase picking and event detection with good accuracy (Ross et al., 2018; Zhu and Beroza, 2018; Perol et al., 2018). However, the general off-line training of CNN requires millions of accurately picked seismic phases, which makes it difficult to be applied to regions without sufficient picked phases. Zhu et al. (2019) proposed a light-weight CNN-based Phase-Identification Classifier (CPIC) that can achieve a high accuracy (>95%) for seismic phase classification when trained with only ~70,000 training phases from aftershocks of the 2008 M7.9 Wenchuan earthquake, China. The seismic phase picking is regarded as a classification problem in CPIC, which aims to give probabilities of the three-channel input seismogram being P/S phase or noise.

The CNN network structure designed by Zhu et al. (2019) is displayed in Figure 6.1. The input is 20-s three-channel seismograms with sampling rate of 100/s. As it passes through 11 convolutional and max-pooling layers for feature extraction, the data shrinks in time but expands in the feature dimension. The final layer is fully connected with 3 outputs that give the probabilities of a window being noise, P, and S phases.

The previous work by Zhu et al. (2019) demonstrates its capability with a relatively small amount training data (~60,000). In this chapter we would like to apply CPIC to regions with even a smaller amount of labeled data through transfer learning (e.g., Yosinski et al., 2014; Donahue et al., 2014).

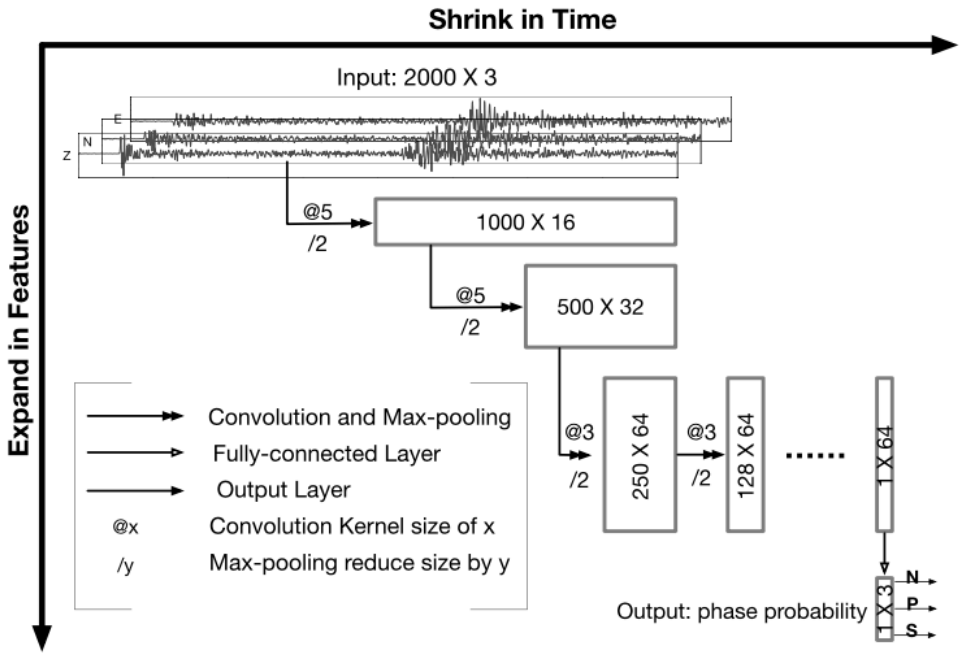

Figure 6.1. Diagram of the CNN structure in CPIC. Modified from Zhu et al. 2019.

6.2 Method and Results

The idea of transfer learning is simple: instead of training a CNN from scratch (random initial weights), we use a pre-trained CNN model from another dataset for either

initialization or feature extraction. In the seismological studies, to the additional seismic data comes from different regions or stations. There are three major strategies in transfer learning:

- Fixed feature extractor. Take a pretrained CNN model (such as the famous ConvNet pretrained on ImageNet), remove the last fully-connected layer which outputs labels for the original dataset, then treat the rest of model as a fixed feature extractor for the new dataset. After extracting the features, train a linear classifier (such as Support Vector Machine or SVM) for the new dataset. In our case, we do not replace the last layer with other linear regression methods, because the classes we need to label are the same for different regions (P, S or noise). So we simply retrain the last fully connected (FC) layer with a new dataset.
- Fine-tuning. In this scenario, the weights of a pretrained CNN model are fine-tuned from the new dataset. One could choose to fine-tune all the layers in the model, or only the last few layers. The reason to keep the earlier layers fixed is that the CNN features are believed to be more generic in early layers and more location-dataset-specific in later layers. We test with fine-tuning all the layers and only the last 1~2 layers of the CNN model.
- Pretrained models. We could use pretrained CNN models from others for fine-tuning. For example, some researchers have released their model weights on github. In our case, we use the pretrained CNN model in Wenchuan dataset (Zhu et al., 2019).

The choice of strategy for transfer learning depends on the size of new dataset and whether it's similar to the original dataset. To validate how well transfer learning works

for CPIC, we first apply the CNN trained on aftershocks in Wenchuan, China to a dataset containing likely human-induced earthquakes in Oklahoma (Figure 6.2). The new dataset in Oklahoma is from 895 events recorded on a regional network in central Oklahoma, with 5000 labeled phases (Chen et al., 2018). The classification accuracy is defined as the percentage of correctly labeled P/S or noise phases in the testing dataset with 5000 or 3000 phases, depending on whether fine-tuning is involved. When testing with data only from three stations, CPIC with slight fine-tuning shows high-accuracy on phase classification in Oklahoma (Table 8). The refined CNN classification results are comparable with the matched filter results using the same catalog events as templates (Chen et al., 2018).

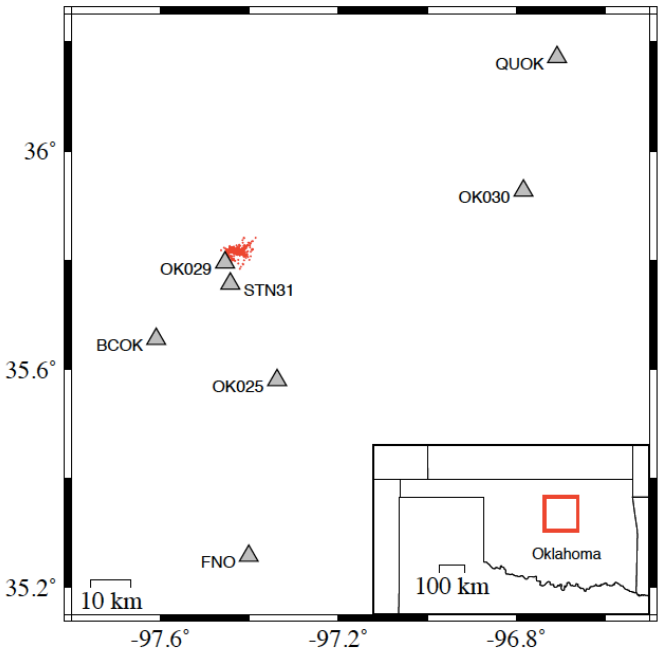

Figure 6.2. Map of dataset in Oklahoma, central U.S. Red dots are 890 events with 11293 labelled P and S phase arrivals, gray triangles are seven broadband stations of the US Geological Survey Networks (GS).

Table 8. Classification accuracy with phases recorded from three stations in Oklahoma. The first row is results of directly applying pre-trained CPIC in Wenchuan to 5000 phases in Oklahoma. The second row is after fine-tuning the fully-connected layer with 2000 phases.

Station	OK025	OK029	OK030	All
Original (%)	95.7	92.2	69.9	87.5
Fine-tuned (%)	98.8	96.2	94.2	97.0

We then expand transfer learning to a larger dataset including more stations in Oklahoma, and two other regions, the Salton Sea Geothermal Field in California, and New Zealand (Figure 6.3). There are around 15,000 phases in each region. As discussed before, we fine-tune part of the networks (FC layer or FC layer+last CNN layer) with the local seismicity in these regions. In addition, we compare the results of training a new model from scratch with a local dataset and fine-tuning the entire model obtained from pretrained dataset in Wenchuan, and compare the influence of training phase numbers with 1000 and 2000 training phases (Table 9).

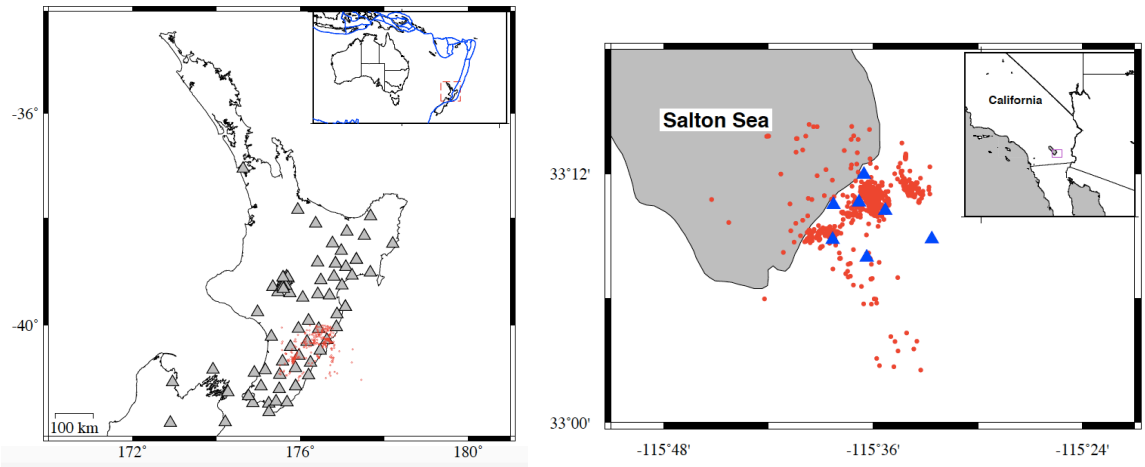

Figure 6.3. Location of stations and events in New Zealand and Salton Sea. Red dots are events in both maps, solid triangles are stations.

Table 9. Classification accuracy of labeled P and S phases, when using CNN trained from Wenchuan dataset directly, or retraining the last fully-connected (FC) layer and last convolutional layer with local data on three different regions.

Region	Training Size	Central Oklahoma	Salton Sea	New Zealand
Total phases		15903	14639	15696
Wenchuan model		79%	41%	84%
New model with local data	1000	81%	95%	86%
	2000	91%	97%	90%
Fine-tune all the layers	1000	86%	89%	91%
	2000	87%	91%	91%
Fine-tune FC layer only	1000	95%	96%	87%
	2000	98%	98%	91%
Fine-tune FC + last 2 layers	1000	94%	94%	94%
	2000	95%	95%	95%

Finally, we demonstrate the capability of event detection with CPIC on continuous waveforms (Figure 6.4). This is performed by applying CNN to a 20-s sliding window with 10% of overlapping to the continuous data (Zhu et al., 2019). An event with M=2.8 and two events with M=0.4 and M=0.6 are detected in New Zealand and SSGF, respectively.

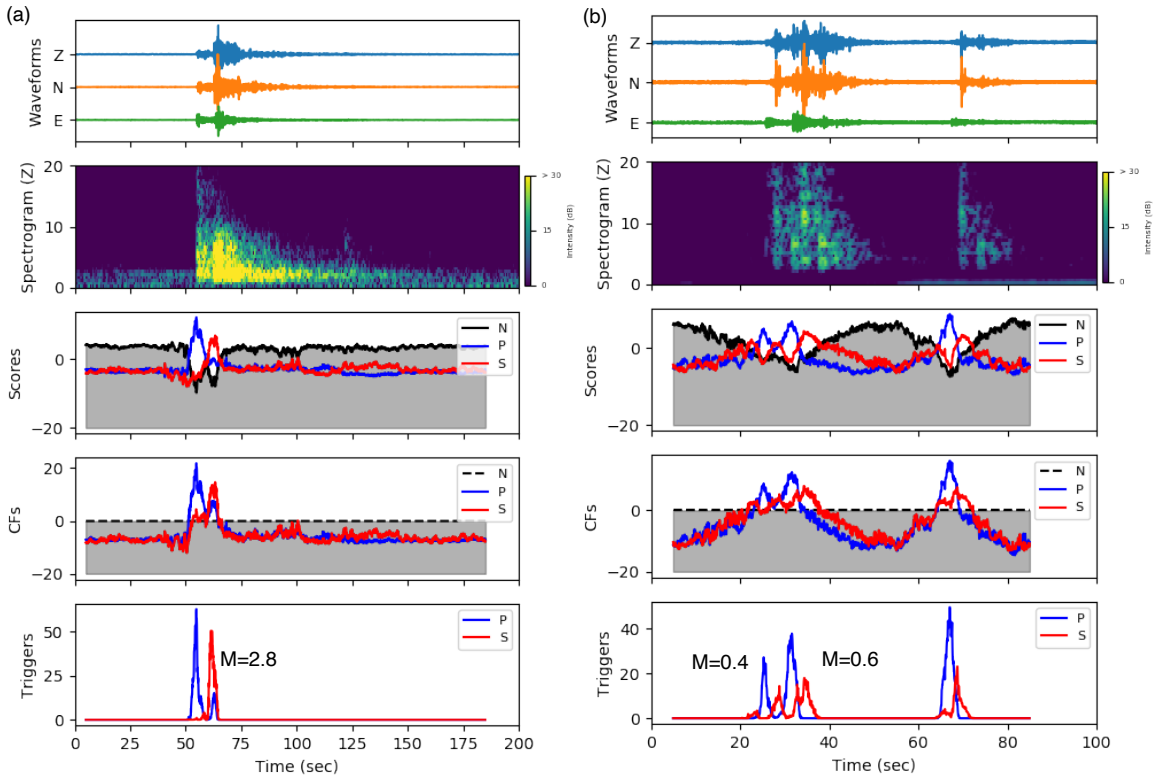

Figure 6.4. Example of detection on continuous data in (a) New Zealand and (b) Salton Sea Geothermal Field.

6.3 Discussion and Conclusion

The tectonic environments in these regions are very different: Wenchuan is in the Longmenshan fault zone formed by continental-continental collisions; Oklahoma is in the intraplate region with many human-induced earthquakes; New Zealand is along plate boundary with a subduction zone and volcanoes; Salton Sea is a geothermal field close to the transform plate boundary. Although the geological environments in Oklahoma and New Zealand are very different from Wenchuan, the direct transfer results are acceptable with accuracy around 80%. Among the three regions, SSGF has the lowest classification accuracy when we directly apply the pretrained CNN in Wenchuan to the local dataset. One major difference in SSGF is that the instrument type here are borehole stations, different from the surface broadband stations in other three regions. We expect that the

CNN phase classifier is either sensitive to instrument type or near-surface conditions because the borehole stations are buried tens of meters underground. This could be further examined with data recorded by a broadband station in SSGF. We did not further explore this because after fine-tuning the accuracy of all three regions is greatly increased to > 95%, which is enough for the goal of phase picking and classification.

It is evident that when the number of training phases increases, the accuracy also increases. When we train a new model with 1000 or 2000 phases, the accuracy is sometimes higher than fine-tuning, but it takes a longer time than only fine-tuning the last few layers. Therefore, the advantage of transfer learning is that we could use less training data and spend less time to obtain the goal of phase picking in a new region. In addition, we can expand the training dataset of the original CNN model to include different regions and instrument types, and use it as an universal phase picker to regions with insufficient labelled data (e.g., Mostafa Mousavi, 2020).

CHAPTER 7. CONCLUSION

In Chapters 2 and 3 of this thesis, I reported several case studies using WMFT to study earthquake triggering in different tectonic settings, mainly focused on dynamic triggering at volcanic/geothermal regions. The first evidence of dynamic triggering by remote large earthquakes in Changbaishan volcano is mainly based on visual inspection and manual-picking (Liu et al., 2017). The follow-up work (Liu et al., in prep) focuses on using a template-matching catalog to better understand the possible triggering relationship between the 2002-2005 volcano unrest and the 2002 M7.2 Wangqing deep-focus earthquake. More recent studies in Mt. Erebus and SSGF are based on WMFT to search for dynamic triggered events. With a six-year of WMFT-based catalog in SSGF, we further look into the impact of geothermal productivity on seismicity in SSGF.

Here are major findings in Chapter 2 and Chapter 3: all of the three regions show responses of dynamic triggering to large earthquakes with high dynamic stress changes; the Changbaishan volcano is more suspectable to seismic waves dominant with long-period waves; Mt. Erebus is more sensitive to distant earthquakes with short-period surface waves; the SSGF is more likely to be triggered by regional earthquakes with high-frequency surface waves. These studies collectively show that it is relatively hard to establish a universal triggering threshold based on either amplitude or frequency content, likely due to differences in tectonic environments, and different types of triggered events.

In Chapter 4 we show a study that utilize WMFT to successfully detect more than 2000 aftershocks for the 2015 Mw7.5 Hindu Kush intermediate-depth earthquake. With further relocation we find clear spatial distribution of the aftershocks with respect to the

mainshock slip, and infer the possible driving mechanisms of them. This work indicates that at least some earthquakes deeper than 100 km could have missing aftershocks, and with good station coverage and a robust detection method we could retrieve the events that are not listed on catalog previously.

At the later stage of my Ph.D. study, I worked on additional earthquake detection problems. With the local-similarity method designed for large-N array, I searched for both regular earthquakes and LPLD events with the IRIS Oklahoma wavefield array in Northern Oklahoma (Chapter 5). During the array deployment period, there are very few earthquakes listed in the OGS catalog, and there have been no reported LPLD event in Oklahoma. Although the LPLD signals we found are finally proven to be generated by moving trains, it demonstrates the capability of classifying natural events and human noises with large-N array. In Chapter 6, we also showed that transfer learning provides new opportunity to apply CNN-based phase picking and event detection method to regions with less prior known events and training dataset.

In the near future, I will continue to work on earthquake detection in Southeast Asia with template matching, machine learning and array techniques during my postdoctoral period in Nanyang Technological University. I will also explore the possibility to combine event detection with determination of source properties such as focal mechanisms and stress drops, and combine seismological studies with other geophysical observations such as geodetic measurements to better understand the physical mechanisms of earthquake interaction and nucleation.

REFERENCES

Aiken, C., X. Meng, and J. Hardebeck, 2016, Testing for the 'predictability'of dynamically triggered earthquakes in The Geysers geothermal field: Earth and Planetary Science Letters, v. 486, p. 129-140.

Aiken, C., and Z. Peng, 2014, Dynamic triggering of microearthquakes in three geothermal/volcanic regions of California: Journal of Geophysical Research: Solid Earth, v. 119, p. 6992-7009.

Aki, K., and P. G. Richards, 2002, Quantitative seismology.

Allen, R., 1982, Automatic phase pickers: Their present use and future prospects: Bulletin of the Seismological Society of America, v. 72, p. S225-S242.

Araki, E., D. M. Saffer, A. J. Kopf, L. M. Wallace, T. Kimura, Y. Machida, S. Ide, E. Davis, and I. Expedition, 2017, Recurring and triggered slow-slip events near the trench at the Nankai Trough subduction megathrust: Science, v. 356, p. 1157-1160.

Aron, A., and J. Hardebeck, 2009a, Seismicity Rate Changes along the Central California Coast due to Stress Changes from the 2003 M 6.5 San Simeon and 2004 M 6.0 Parkfield Earthquakes: Bulletin of the Seismological Society of America, v. 99, p. 2280-2292.

Aron, A., and J. L. Hardebeck, 2009b, Seismicity rate changes along the central California coast due to stress changes from the 2003 M 6.5 San Simeon and 2004 M 6.0 Parkfield earthquakes: Bulletin of the Seismological Society of America, v. 99, p. 2280-2292.

Atkinson, G. M., D. W. Eaton, and N. Igonin, 2020, Developments in understanding seismicity triggered by hydraulic fracturing: Nature Reviews Earth & Environment, p. 1-14.

Baer, M., and U. Kradolfer, 1987, An automatic phase picker for local and teleseismic events: Bulletin of the Seismological Society of America, v. 77, p. 1437-1445.

Bennington, N., C. Thurber, K. L. Feigl, and J. Murray-Moraleda, 2011, Aftershock distribution as a constraint on the geodetic model of coseismic slip for the 2004 Parkfield earthquake: Pure and applied geophysics, v. 168, p. 1553-1565.

Bergen, K. J., P. A. Johnson, V. Maarten, and G. C. Beroza, 2019, Machine learning for data-driven discovery in solid Earth geoscience: Science, v. 363, p. eaau0323.

Beroza, G. C., and S. Ide, 2011, Slow earthquakes and nonvolcanic tremor: Annual review of Earth and planetary sciences, v. 39, p. 271-296.

Billington, S., B. L. Isacks, and M. Barazangi, 1977, Spatial distribution and focal mechanisms of mantle earthquakes in the Hindu Kush–Pamir region: A contorted Benioff zone: Geology, v. 5, p. 699-704.

Boschi, L., A. Piersanti, and G. Spada, 2000, Global postseismic deformation: Deep earthquakes: Journal of Geophysical Research: Solid Earth, v. 105, p. 631-652.

Bosl, W., and A. Nur, 2002, Aftershocks and pore fluid diffusion following the 1992 Landers earthquake: Journal of Geophysical Research: Solid Earth, v. 107, p. ESE 17-1-ESE 17-12.

Brodsky, E. E., and L. J. Lajoie, 2013, Anthropogenic seismicity rates and operational parameters at the Salton Sea Geothermal Field: Science, v. 341, p. 543-546.

Brodsky, E. E., and S. G. Prejean, 2005, New constraints on mechanisms of remotely triggered seismicity at Long Valley Caldera: Journal of Geophysical Research: Solid Earth, v. 110.

Brodsky, E. E., E. Roeloffs, D. Woodcock, I. Gall, and M. Manga, 2003, A mechanism for sustained groundwater pressure changes induced by distant earthquakes: Journal of Geophysical Research: Solid Earth, v. 108.

Brodsky, E. E., and N. J. van der Elst, 2014, The uses of dynamic earthquake triggering: Annual Review of Earth and Planetary Sciences, v. 42, p. 317-339.

Brown, J. R., G. C. Beroza, and D. R. Shelly, 2008, An autocorrelation method to detect low frequency earthquakes within tremor: Geophysical Research Letters, v. 35.

Caffagni, E., D. Eaton, M. van der Baan, and J. P. Jones, 2015, Regional seismicity: A potential pitfall for identification of long-period long-duration events: Geophysics, v. 80, p. A1-A5.

Castro, R. R., R. Clayton, E. Hauksson, and J. Stock, 2017, Observations of remotely triggered seismicity in Salton Sea and Coso geothermal regions, Southern California, USA, after big (MW> 7.8) teleseismic earthquakes: Geofísica internacional, v. 56, p. 269-286.

Chao, K., Z. Peng, Y. J. Hsu, K. Obara, C. Wu, K. E. Ching, S. van der Lee, H. C. Pu, P. L. Leu, and A. Wech, 2017a, Temporal variation of tectonic tremor activity in southern Taiwan around the 2010 ML6. 4 Jiashian earthquake: Journal of Geophysical Research: Solid Earth, v. 122, p. 5417-5434.

Chao, K., Z. Peng, Y. J. Hsu, K. Obara, C. Wu, K. E. Ching, S. van der Lee, H. C. Pu, P. L. Leu, and A. Wech, 2017b, Temporal variation of tectonic tremor activity in southern Taiwan around the 2010 ML6. 4 Jiashian earthquake: Journal of Geophysical Research: Solid Earth, v. 122, p. 5417-5434.

Chaput, J., M. Campillo, R. Aster, P. Roux, P. Kyle, H. Knox, and P. Czoski, 2015a, Multiple scattering from icequakes at Erebus volcano, Antarctica: Implications for imaging at glaciated volcanoes: Journal of Geophysical Research: Solid Earth, v. 120, p. 1129-1141.

Chaput, J., M. Campillo, R. C. Aster, P. Roux, P. R. Kyle, H. Knox, and P. Czoski, 2015b, Multiple scattering from icequakes at Erebus volcano, Antarctica: Implications for imaging at glaciated volcanoes: Journal of Geophysical Research: Solid Earth, v. 120, p. 1129-1141.

Chaput, J., V. Clerc, M. Campillo, P. Roux, and H. Knox, 2015c, On the practical convergence of coda-based correlations: a window optimization approach: Geophysical Journal International, v. 204, p. 736-747.

Chaput, J., V. Clerc, M. Campillo, P. Roux, and H. Knox, 2016, On the practical convergence of coda-based correlations: a window optimization approach: Geophysical Journal International, v. 204, p. 736-747.

Chaput, J., D. Zandomeneghi, R. Aster, H. Knox, and P. Kyle, 2012a, Imaging of Erebus volcano using body wave seismic interferometry of Strombolian eruption coda: Geophysical Research Letters, v. 39.

Chaput, J. A., D. Zandomeneghi, R. C. Aster, H. Knox, and P. R. Kyle, 2012b, Imaging of Erebus volcano using body wave seismic interferometry of Strombolian eruption coda: Geophysical Research Letters, v. 39.

Chatelain, J.-L., S. Roecker, D. Hatzfeld, and P. Molnar, 1980, Microearthquake seismicity and fault plane solutions in the Hindu Kush region and their tectonic implications: Journal of Geophysical Research: Solid Earth, v. 85, p. 1365-1387.

Chen, H., F. Niu, Y. Tang, and K. Tao, 2018a, Toward the origin of long-period long-duration seismic events during hydraulic fracturing treatment: A case study in the shale play of Sichuan Basin, China: Seismological Research Letters, v. 89, p. 1075-1083.

Chen, Q.-f., L. Li, G. Li, L. Chen, W.-t. Peng, Y. Tang, Y. Chen, and F.-y. Wang, 2004, Seismic features of vibration induced by train: Acta Seismologica Sinica, v. 17, p. 715-724.

Chen, X., J. Haffener, T. H. W. Goebel, X. Meng, Z. Peng, and J. C. Chang, 2018b, Temporal correlation between seismic moment and injection volume for an

induced earthquake sequence in central Oklahoma: Journal of Geophysical Research: Solid Earth, v. 123, p. 3047-3064.

Chen, X., and P. Shearer, 2011, Comprehensive analysis of earthquake source spectra and swarms in the Salton Trough, California: Journal of Geophysical Research: Solid Earth, v. 116.

Das, I., and M. D. Zoback, 2013a, Long-period long-duration seismic events during hydraulic stimulation of shale and tight-gas reservoirs — Part 2: Location and mechanisms: GEOPHYSICS, v. 78, p. KS109-KS117.

Das, I., and M. D. Zoback, 2013b, Long-period, long-duration seismic events during hydraulic stimulation of shale and tight-gas reservoirs—Part 1: Waveform characteristicsLPLD events: Waveform characteristics: Geophysics, v. 78, p. KS107-KS118.

Das, S., and C. H. Scholz, 1981, Off-fault aftershock clusters caused by shear stress increase?: Bulletin of the Seismological Society of America, v. 71, p. 1669-1675.

Donahue, J., Y. Jia, O. Vinyals, J. Hoffman, N. Zhang, E. Tzeng, and T. Darrell, 2014, Decaf: A deep convolutional activation feature for generic visual recognition: International conference on machine learning, p. 647-655.

Efron, B., and G. Gong, 1983, A leisurely look at the bootstrap, the jackknife, and cross-validation: The American Statistician, v. 37, p. 36-48.

Efron, B., and R. Tibshirani, 1991, Statistical data analysis in the computer age: Science, v. 253, p. 390-395.

Eibl, E. P., I. Lokmer, C. J. Bean, E. Akerlie, and K. S. Vogfjörd, 2015, Helicopter vs. volcanic tremor: Characteristic features of seismic harmonic tremor on volcanoes: Journal of Volcanology and Geothermal Research, v. 304, p. 108-117.

Ellsworth, W. L., 2013, Injection-induced earthquakes: Science, v. 341, p. 1225942.

Ellsworth, W. L., D. Giardini, J. Townend, S. Ge, and T. Shimamoto, 2019, Triggering of the Pohang, Korea, Earthquake (M w 5.5) by Enhanced Geothermal System Stimulation: Seismological Research Letters, v. 90, p. 1844-1858.

Enescu, B., K. Shimojo, A. Opris, and Y. Yagi, 2016, Remote triggering of seismicity at Japanese volcanoes following the 2016 M7. 3 Kumamoto earthquake: Earth, Planets and Space, v. 68, p. 1-9.

Fletcher, J. B., P. Spudich, and L. M. Baker, 2006a, Rupture propagation of the 2004 Parkfield, California, earthquake from observations at the UPSAR: Bulletin of the Seismological Society of America, v. 96, p. S129-S142.

Fletcher, J. B., P. Spudich, and L. M. Baker, 2006b, Rupture propagation of the 2004 Parkfield, California, earthquake from observations at the UPSAR: Bulletin of the Seismological Society of America, v. 96, p. S129-S142.

Foulger, G. R., M. P. Wilson, J. G. Gluyas, B. R. Julian, and R. J. Davies, 2018, Global review of human-induced earthquakes: Earth-Science Reviews, v. 178, p. 438-514.

Frank, W., and N. Shapiro, 2014, Automatic detection of low-frequency earthquakes (LFEs) based on a beamformed network response: Geophysical Journal International, v. 197, p. 1215-1223.

Freed, A. M., 2005, Earthquake triggering by static, dynamic, and postseismic stress transfer: Annu. Rev. Earth Planet. Sci., v. 33, p. 335-367.

Freed, A. M., 2007, Afterslip (and only afterslip) following the 2004 Parkfield, California, earthquake: Geophysical Research Letters, v. 34.

Frohlich, C., 1987, Aftershocks and temporal clustering of deep earthquakes: Journal of Geophysical Research: Solid Earth, v. 92, p. 13944-13956.

Frohlich, C., 1989, The nature of deep-focus earthquakes: Annual Review of Earth and Planetary Sciences, v. 17, p. 227-254.

Frohlich, C., 2006, Deep earthquakes, Cambridge university press.

Fuchs, F., and G. Bokelmann, 2018a, Equidistant spectral lines in train vibrations: Seismological Research Letters, v. 89, p. 56-66.

Fuchs, F., and G. Bokelmann, 2018b, Equidistant spectral lines in train vibrations: Seismological Research Letters, v. 89, p. 56-66.

Fuchs, F., and G. Bokelmann, 2018c, Equidistant spectral lines in train vibrations: Seismological Research Letters, v. 89, p. 56-66.

Gibbons, S. J., and F. Ringdal, 2006, The detection of low magnitude seismic events using array-based waveform correlation: Geophysical Journal International, v. 165, p. 149-166.

Gomberg, J., 2001, The failure of earthquake failure models: Journal of Geophysical Research: Solid Earth, v. 106, p. 16253-16263.

Gomberg, J., P. Bodin, K. Larson, and H. Dragert, 2004, Earthquake nucleation by transient deformations caused by the M= 7.9 Denali, Alaska, earthquake: Nature, v. 427, p. 621-624.

Gomberg, J., and S. Davis, 1996, Stress/strain changes and triggered seismicity at The Geysers, California: Journal of Geophysical Research: Solid Earth, v. 101, p. 733-749.

Gomberg, J., W. Schulz, P. Bodin, and J. Kean, 2011a, Seismic and geodetic signatures of fault slip at the Slumgullion Landslide Natural Laboratory: Journal of Geophysical Research: Solid Earth, v. 116.

Gomberg, J., W. Schulz, P. Bodin, and J. Kean, 2011b, Seismic and geodetic signatures of fault slip at the Slumgullion Landslide Natural Laboratory: Journal of Geophysical Research: Solid Earth, v. 116.

Green, H. W., and H. Houston, 1995, The mechanics of deep earthquakes: Annual Review of Earth and Planetary Sciences, v. 23, p. 169-213.

Green, H. W., and C. Marone, 2002, Instability of deformation: Reviews in mineralogy and geochemistry, v. 51, p. 181-199.

Guglielmi, Y., F. Cappa, J.-P. Avouac, P. Henry, and D. Elsworth, 2015, Seismicity triggered by fluid injection–induced aseismic slip: Science, v. 348, p. 1224-1226.

Guo, H., and H. Zhang, 2016, Development of double-pair double difference earthquake location algorithm for improving earthquake locations: Geophysical Journal International, p. ggw397.

Guo, H., H. Zhang, R. M. Nadeau, and Z. Peng, 2017, High-resolution deep tectonic tremor locations beneath the San Andreas Fault near Cholame, California, using the double-pair double-difference location method: Journal of Geophysical Research: Solid Earth, v. 122, p. 3062-3075.

Gutenberg, B., and C. F. Richter, 1944, Frequency of earthquakes in California: Bulletin of the Seismological Society of America, v. 34, p. 185-188.

Hainzl, S., 2016, Rate-dependent incompleteness of earthquake catalogs: Seismological Research Letters, v. 87, p. 337-344.

Hamburger, M. W., D. R. Sarewitz, T. L. Pavlis, and G. A. Popandopulo, 1992, Structural and seismic evidence for intracontinental subduction in the Peter the First Range, central Asia: Geological Society of America Bulletin, v. 104, p. 397-408.

Harris, R. A., 2017a, Large earthquakes and creeping faults: Reviews of Geophysics, v. 55, p. 169-198.

Harris, R. A., 2017b, Large earthquakes and creeping faults: Reviews of Geophysics, v. 55, p. 169-198.

Hauksson, E., W. Yang, and P. M. Shearer, 2012, Waveform relocated earthquake catalog for southern California (1981 to June 2011): Bulletin of the Seismological Society of America, v. 102, p. 2239-2244.

Helffrich, G., J. Wookey, and I. Bastow, 2013a, The seismic analysis code: A primer and user's guide, Cambridge University Press.

Helffrich, G., J. Wookey, and I. Bastow, 2013b, The seismic analysis code: A primer and user's guide, Cambridge University Press.

Helmstetter, A., and S. Garambois, 2010, Seismic monitoring of Séchilienne rockslide (French Alps): Analysis of seismic signals and their correlation with rainfalls: Journal of Geophysical Research: Earth Surface, v. 115.

Hill, D. P., F. Pollitz, and C. Newhall, 2002, Earthquake-volcano interactions: Physics Today, v. 55, p. 41-47.

Hill, D. P., and S. Prejean, 2015, Dynamic triggering. In: Gerald Schubert (editor-in-chief) Treatise on Geophysics, 2nd edition, Vol 4. Oxford: Elsevier; 2015. p. 273-304.

Hobbs, B. E., and A. Ord, 1988, Plastic instabilities: Implications for the origin of intermediate and deep focus earthquakes: Journal of Geophysical Research: Solid Earth, v. 93, p. 10521-10540.

Hotovec, A. J., S. G. Prejean, J. E. Vidale, and J. Gomberg, 2013, Strongly gliding harmonic tremor during the 2009 eruption of Redoubt Volcano: Journal of Volcanology and Geothermal Research, v. 259, p. 89-99.

Hough, S. E., and H. Kanamori, 2002, Source properties of earthquakes near the Salton Sea triggered by the 16 October 1999 M 7.1 Hector Mine, California, earthquake: Bulletin of the Seismological Society of America, v. 92, p. 1281-1289.

Houston, H., and S. Gerald, 2007, Deep earthquakes, Treatise on Geophysics, Elsevier, Amsterdam.

Hsu, Y.-J., M. Simons, J.-P. Avouac, J. Galetzka, K. Sieh, M. Chlieh, D. Natawidjaja, L. Prawirodirdjo, and Y. Bock, 2006, Frictional afterslip following the 2005 Nias-Simeulue earthquake, Sumatra: Science, v. 312, p. 1921-1926.

Hu, H., A. Li, and R. Zavala-Torres, 2017, Long-period long-duration seismic events during hydraulic fracturing: Implications for tensile fracture development: Geophysical Research Letters, v. 44, p. 4814-4819.

Husen, S., R. Taylor, R. Smith, and H. Healser, 2004, Changes in geyser eruption behavior and remotely triggered seismicity in Yellowstone National Park produced by the 2002 M 7.9 Denali fault earthquake, Alaska: Geology, v. 32, p. 537-540.

Hutchison, A. A., and A. Ghosh, 2016, Very low frequency earthquakes spatiotemporally asynchronous with strong tremor during the 2014 episodic tremor and slip event in Cascadia: Geophysical Research Letters, v. 43, p. 6876-6882.

Hutchison, A. A., and A. Ghosh, 2017, Ambient tectonic tremor in the san jacinto fault, near the anza gap, detected by multiple mini seismic arraysambient tectonic tremor in the san jacinto fault, near the anza gap, detected by multiple mini seismic arrays: Bulletin of the Seismological Society of America, v. 107, p. 1985-1993.

Ito, Y., and K. Obara, 2006, Dynamic deformation of the accretionary prism excites very low frequency earthquakes: Geophysical Research Letters, v. 33.

Iwata, T., 2008, Low detection capability of global earthquakes after the occurrence of large earthquakes: Investigation of the Harvard CMT catalogue: Geophysical Journal International, v. 174, p. 849-856.

Johnson, C. W., and R. Bürgmann, 2016, Delayed dynamic triggering: Local seismicity leading up to three remote M≥ 6 aftershocks of the 11 April 2012 M8. 6 Indian Ocean earthquake: Journal of Geophysical Research: Solid Earth, v. 121, p. 134-151.

Johnston, M., D. Hill, and A. Pitt, 2002, Deformation and seismicity triggered beneath Mammoth Mountain, California, by surface waves from the M7. 9 Denali fault, Alaska, earthquake of 3 November 2002: AGU Fall Meeting Abstracts.

Kagan, Y., and L. Knopoff, 1980, Dependence of seismicity on depth: Bulletin of the Seismological Society of America, v. 70, p. 1811-1822.

Kagan, Y. Y., 2004, Short-term properties of earthquake catalogs and models of earthquake source: Bulletin of the Seismological Society of America, v. 94, p. 1207-1228.

Kanamori, H., and E. Hauksson, 1992, A slow earthquake in the Santa Maria Basin, California: Bulletin of the Seismological Society of America, v. 82, p. 2087-2096.

Karato, S.-i., M. R. Riedel, and D. A. Yuen, 2001, Rheological structure and deformation of subducted slabs in the mantle transition zone: implications for mantle circulation and deep earthquakes: Physics of the Earth and Planetary Interiors, v. 127, p. 83-108.

Kato, A., and S. Nakagawa, 2014, Multiple slow-slip events during a foreshock sequence of the 2014 Iquique, Chile Mw 8.1 earthquake: Geophysical Research Letters, v. 41, p. 5420-5427.

Kato, A., and K. Obara, 2014, Step-like migration of early aftershocks following the 2007 Mw 6.7 Noto-Hanto earthquake, Japan: Geophysical Research Letters, v. 41, p. 3864-3869.

Kato, A., K. Obara, T. Igarashi, H. Tsuruoka, S. Nakagawa, and N. Hirata, 2012, Propagation of slow slip leading up to the 2011 Mw 9.0 Tohoku-Oki earthquake: Science, v. 335, p. 705-708.

Kato, N., 2007, Expansion of aftershock areas caused by propagating post-seismic sliding: Geophysical Journal International, v. 168, p. 797-808.

Keranen, K. M., H. M. Savage, G. A. Abers, and E. S. Cochran, 2013, Potentially induced earthquakes in Oklahoma, USA: Links between wastewater injection and the 2011 Mw 5.7 earthquake sequence: Geology, v. 41, p. 699-702.

Kilb, D., J. Gomberg, and P. Bodin, 2000, Triggering of earthquake aftershocks by dynamic stresses: Nature, v. 408, p. 570-574.

Kilb, D., R. Newman, F. Vernon, J. Eakins, L. Ziegler, J. Bowen, and J. Otero, 2003, Education and outreach based on data from the Anza seismic network in southern California: Seismological Research Letters, v. 74, p. 522-528.

Kilb, D., Z. Peng, D. Simpson, A. Michael, M. Fisher, and D. Rohrlick, 2012, Listen, watch, learn: SeisSound video products: Seismological Research Letters, v. 83, p. 281-286.

Kim, K.-H., J.-H. Ree, Y. Kim, S. Kim, S. Y. Kang, and W. Seo, 2018, Assessing whether the 2017 Mw 5.4 Pohang earthquake in South Korea was an induced event: Science, v. 360, p. 1007-1009.

King, G., and M. Devès, 2015, Fault interaction, earthquake stress changes, and the evolution of seismicity.

King, G. C., R. S. Stein, and J. Lin, 1994, Static stress changes and the triggering of earthquakes: Bulletin of the Seismological Society of America, v. 84, p. 935-953.

Kirby, S. H., S. Stein, E. A. Okal, and D. C. Rubie, 1996, Metastable mantle phase transformations and deep earthquakes in subducting oceanic lithosphere: Reviews of geophysics, v. 34, p. 261-306.

Kong, Q., D. T. Trugman, Z. E. Ross, M. J. Bianco, B. J. Meade, and P. Gerstoft, 2019, Machine learning in seismology: Turning data into insights: Seismological Research Letters, v. 90, p. 3-14.

Kufner, S.-K., B. Schurr, C. Haberland, Y. Zhang, J. Saul, A. Ischuk, and I. Oimahmadov, 2017, Zooming into the Hindu Kush slab break-off: a rare glimpse on the terminal stage of subduction: Earth and Planetary Science Letters, v. 461, p. 127-140.

Kufner, S.-K., B. Schurr, C. Sippl, X. Yuan, L. Ratschbacher, A. Ischuk, S. Murodkulov, F. Schneider, J. Mechie, and F. Tilmann, 2016, Deep India meets deep Asia: Lithospheric indentation, delamination and break-off under Pamir and Hindu Kush (Central Asia): Earth and Planetary Science Letters, v. 435, p. 171-184.

Lei, X., Z. Wang, and J. Su, 2019, The December 2018 ML 5.7 and January 2019 ML 5.3 earthquakes in south Sichuan basin induced by shale gas hydraulic fracturing: Seismological Research Letters, v. 90, p. 1099-1110.

Li, C., Z. Li, Z. Peng, C. Zhang, and N. Nakata, 2017a, Detecting micro-seismicity and long-duration tremor-like events from the Oklahoma wavefield experiment: AGU Fall Meeting Abstracts.

Li, L., D. Yao, X. Meng, Z. Peng, and B. Wang, 2017b, Increasing seismicity in Southern Tibet following the 2015 Mw 7.8 Gorkha, Nepal earthquake: Tectonophysics, v. 714, p. 62-70.

Li, C., Z. Li, Z. Peng, C. Zhang, N. Nakata, and T. Sickbert, 2018a, Long-period long-duration events detected by the IRIS community wavefield demonstration experiment in Oklahoma: Tremor or train signals?: Seismological Research Letters, v. 89, p. 1652-1659.

Li, C., Z. Peng, D. Yao, H. Guo, Z. Zhan, and H. Zhang, 2018b, Abundant aftershock sequence of the 2015 M w7. 5 Hindu Kush intermediate-depth earthquake: Geophysical Journal International, v. 213, p. 1121-1134.

Li, C., L. Zhu, D. Yao, X. Meng, Z. Peng, J. H. McClellan, and J. I. Walter, 2018c, Transfer learning for seismic phase picking on different geographic regions: AGUFM, v. 2018, p. S11E-0431.

Li, Z., Z. Peng, D. Hollis, L. Zhu, and J. McClellan, 2018d, High-resolution seismic event detection using local similarity for Large-N arrays: Scientific Reports, v. 8, p. 1646.

Li, Z., M. A. Meier, E. Hauksson, Z. Zhan, and J. Andrews, 2018e, Machine learning seismic wave discrimination: Application to earthquake early warning: Geophysical Research Letters, v. 45, p. 4773-4779.

Linde, A. T., M. T. Gladwin, M. J. Johnston, R. L. Gwyther, and R. G. Bilham, 1996, A slow earthquake sequence on the San Andreas fault: Nature, v. 383, p. 65-68.

Lister, G., B. Kennett, S. Richards, and M. Forster, 2008, Boudinage of a stretching slablet implicated in earthquakes beneath the Hindu Kush: Nature Geoscience, v. 1, p. 196-201.

Liu, G., C. Li, Z. Peng, X. Li, and J. Wu, 2017, Detecting remotely triggered microseismicity around Changbaishan Volcano following nuclear explosions in North Korea and large distant earthquakes around the world: Geophysical Research Letters, v. 44, p. 4829-4838.

Liu, M., Y. Huang, and J. Ritsema, 2019, Stress drop variation of deep-focus earthquakes based on empirical Green's functions: Geophysical Research Letters, p. e2019GL086055.

Lohman, R., and J. McGuire, 2007, Earthquake swarms driven by aseismic creep in the Salton Trough, California: Journal of Geophysical Research: Solid Earth, v. 112.

Marsan, D., 2011, Seismicity rate changes, *in* M. Wyss, ed.

Matsuzawa, T., Y. Asano, and K. Obara, 2015, Very low frequency earthquakes off the Pacific coast of Tohoku, Japan: Geophysical Research Letters, v. 42, p. 4318-4325.

Matthews, M. V., and P. A. Reasenberg, 1988, Statistical methods for investigating quiescence and other temporal seismicity patterns: Pure and Applied Geophysics, v. 126, p. 357-372.

McGarr, A., D. Simpson, L. Seeber, and W. Lee, 2002, Case histories of induced and triggered seismicity: International Geophysics Series, v. 81, p. 647-664.

McGuire, J. J., J. A. Collins, E. Davis, K. Becker, and M. Heesemann, 2018, A lack of dynamic triggering of slow slip and tremor indicates that the shallow Cascadia megathrust offshore Vancouver Island is likely locked: Geophysical Research Letters, v. 45, p. 11,095-11,103.

McNutt, S. R., 2005, Volcanic seismology: Annu. Rev. Earth Planet. Sci., v. 32, p. 461-491.

Meng, H., and Y. Ben-Zion, 2018, Characteristics of airplanes and helicopters recorded by a dense seismic array near Anza California: Journal of Geophysical Research: Solid Earth, v. 123, p. 4783-4797.

Meng, X., and Z. Peng, 2014, Seismicity rate changes in the Salton Sea Geothermal Field and the San Jacinto Fault Zone after the 2010 M w 7.2 El Mayor-Cucapah earthquake: Geophysical Journal International, v. 197, p. 1750-1762.

Meng, X., Z. Peng, and J. L. Hardebeck, 2013, Seismicity around Parkfield correlates with static shear stress changes following the 2003 Mw6. 5 San Simeon earthquake: Journal of Geophysical Research: Solid Earth, v. 118, p. 3576-3591.

Mousavi, S. M., Y. Sheng, W. Zhu, and G. C. Beroza, 2019, STanford EArthquake Dataset (STEAD): A Global Data Set of Seismic Signals for AI: IEEE Access.

Myers, S. C., T. C. Wallace, S. L. Beck, P. G. Silver, G. Zandt, J. Vandecar, and E. Minaya, 1995, Implications of spatial and temporal development of the aftershock sequence for the Mw 8.3 June 9, 1994 deep Bolivian earthquake: Geophysical research letters, v. 22, p. 2269-2272.

Negredo, A. M., A. Replumaz, A. Villaseñor, and S. Guillot, 2007, Modeling the evolution of continental subduction processes in the Pamir–Hindu Kush region: Earth and Planetary Science Letters, v. 259, p. 212-225.

Nur, A., and J. R. Booker, 1972, Aftershocks caused by pore fluid flow?: Science, v. 175, p. 885-887.

Nyffenegger, P., and C. Frohlich, 2000, Aftershock occurrence rate decay properties for intermediate and deep earthquake sequences: Geophysical Research Letters, v. 27, p. 1215-1218.

Obara, K., 2002, Nonvolcanic deep tremor associated with subduction in southwest Japan: Science, v. 296, p. 1679-1681.

Obara, K., H. Hirose, F. Yamamizu, and K. Kasahara, 2004, Episodic slow slip events accompanied by non-volcanic tremors in southwest Japan subduction zone: Geophysical Research Letters, v. 31.

Obara, K., and A. Kato, 2016, Connecting slow earthquakes to huge earthquakes: Science, v. 353, p. 253-257.

Ogata, Y., 1988, Statistical models for earthquake occurrences and residual analysis for point processes: Journal of the American Statistical association, v. 83, p. 9-27.

Ogawa, M., 1987, Shear instability in a viscoelastic material as the cause of deep focus earthquakes: Journal of Geophysical Research: Solid Earth, v. 92, p. 13801-13810.

Pankow, K. L., and D. Kilb, 2020, Going Beyond Rate changes as the Sole indicator for Dynamic triggering of earthquakes: Scientific reports, v. 10, p. 1-12.

Parsons, T., 2005, A hypothesis for delayed dynamic earthquake triggering: Geophysical Research Letters, v. 32.

Paul Winberry, J., S. Anandakrishnan, D. A. Wiens, and R. B. Alley, 2013, Nucleation and seismic tremor associated with the glacial earthquakes of Whillans Ice Stream, Antarctica: Geophysical Research Letters, v. 40, p. 312-315.

Pavlis, G. L., and M. W. Hamburger, 1991, Aftershock sequences of intermediate-depth earthquakes in the Pamir-Hindu Kush seismic zone: Journal of Geophysical Research: Solid Earth, v. 96, p. 18107-18117.

Pegler, G., and S. Das, 1998, An enhanced image of the Pamir–Hindu Kush seismic zone from relocated earthquake hypocentres: Geophysical Journal International, v. 134, p. 573-595.

Peng, Z., and J. Gomberg, 2010, An integrated perspective of the continuum between earthquakes and slow-slip phenomena: Nature geoscience, v. 3, p. 599-607.

Peng, Z., D. P. Hill, D. R. Shelly, and C. Aiken, 2010, Remotely triggered microearthquakes and tremor in central California following the 2010 Mw 8.8 Chile earthquake: Geophysical Research Letters, v. 37.

Peng, Z., L. T. Long, and P. Zhao, 2011, The relevance of high-frequency analysis artifacts to remote triggering: Seismological Research Letters, v. 82, p. 654-660.

Peng, Z., J. E. Vidale, M. Ishii, and A. Helmstetter, 2007, Seismicity rate immediately before and after main shock rupture from high-frequency waveforms in Japan: Journal of Geophysical Research: Solid Earth, v. 112.

Peng, Z., J. I. Walter, R. C. Aster, A. Nyblade, D. A. Wiens, and S. Anandakrishnan, 2014a, Antarctic icequakes triggered by the 2010 Maule earthquake in Chile: Nature Geoscience, v. 7, p. 677-681.

Peng, Z., J. I. Walter, R. C. Aster, A. Nyblade, D. A. Wiens, and S. Anandakrishnan, 2014b, Antarctic icequakes triggered by the 2010 Maule earthquake in Chile: Nature Geoscience, v. 7, p. 677-681.

Peng, Z., and P. Zhao, 2009, Migration of early aftershocks following the 2004 Parkfield earthquake: Nature Geoscience, v. 2, p. 877-881.

Perfettini, H., and J. P. Avouac, 2004, Postseismic relaxation driven by brittle creep: A possible mechanism to reconcile geodetic measurements and the decay rate of

aftershocks, application to the Chi-Chi earthquake, Taiwan: Journal of Geophysical Research: Solid Earth, v. 109.

Perol, T., M. Gharbi, and M. Denolle, 2018, Convolutional neural network for earthquake detection and location: Science Advances, v. 4, p. e1700578.

Persh, S. E., and H. Houston, 2004, Strongly depth-dependent aftershock production in deep earthquakes: Bulletin of the Seismological Society of America, v. 94, p. 1808-1816.

Petit, J. P., and M. Barquins, 1988, Can natural faults propagate under mode II conditions?: Tectonics, v. 7, p. 1243-1256.

Poli, P., G. Prieto, E. Rivera, and S. Ruiz, 2016a, Earthquakes initiation and thermal shear instability in the Hindu Kush intermediate depth nest: Geophysical Research Letters, v. 43, p. 1537-1542.

Poli, P., G. Prieto, C. Yu, M. Florez, H. Agurto-Detzel, T. Mikesell, G. Chen, V. Dionicio, and P. Pedraza, 2016b, Complex rupture of the M 6.3 2015 March 10 Bucaramanga earthquake: Evidence of strong weakening process: Geophysical Journal International, v. 205, p. 988-994.

Pollitz, F. F., and M. J. Johnston, 2006, Direct test of static stress versus dynamic stress triggering of aftershocks: Geophysical research letters, v. 33.

Prejean, S. G., D. P. Hill, E. E. Brodsky, S. E. Hough, M. J. S. Johnston, S. D. Malone, D. H. Oppenheimer, A. M. Pitt, and K. B. Richards-Dinger, 2004, Remotely triggered seismicity on the United States west coast following the M w 7.9 Denali fault earthquake: Bulletin of the Seismological Society of America, v. 94, p. S348-S359.

Prieto, G. A., G. C. Beroza, S. A. Barrett, G. A. López, and M. Florez, 2012, Earthquake nests as natural laboratories for the study of intermediate-depth earthquake mechanics: Tectonophysics, v. 570, p. 42-56.

Prozorov, A., and A. Dziewonski, 1982, A method of studying variations in the clustering property of earthquakes: application to the analysis of global seismicity: Journal of Geophysical Research: Solid Earth, v. 87, p. 2829-2839.

Quiros, D. A., L. D. Brown, and D. Kim, 2016, Seismic interferometry of railroad induced ground motions: Body and surface wave imaging: Geophysical Supplements to the Monthly Notices of the Royal Astronomical Society, v. 205, p. 301-313.

Raleigh, C. B., and M. Paterson, 1965, Experimental deformation of serpentinite and its tectonic implications: Journal of Geophysical Research, v. 70, p. 3965-3985.

Reid, H. F., 1911, The elastic-rebound theory of earthquakes: Univ. Calif. Publ.. Bull. Dept. Geol., v. 6, p. 413-444.

Riahi, N., and P. Gerstoft, 2015, The seismic traffic footprint: Tracking trains, aircraft, and cars seismically: Geophysical Research Letters, v. 42, p. 2674-2681.

Roecker, S., O. Soboleva, I. Nersesov, A. Lukk, D. Hatzfeld, J.-L. Chatelain, and P. Molnar, 1980, Seismicity and fault plane solutions of intermediate depth earthquakes in the Pamir-Hindu Kush region: Journal of Geophysical Research: Solid Earth, v. 85, p. 1358-1364.

Rogers, G., and H. Dragert, 2003, Episodic tremor and slip on the Cascadia subduction zone: The chatter of silent slip: Science, v. 300, p. 1942-1943.

Ross, Z. E., M. A. Meier, and E. Hauksson, 2018, P wave arrival picking and first-motion polarity determination with deep learning: Journal of Geophysical Research: Solid Earth, v. 123, p. 5120-5129.

Ross, Z. E., D. T. Trugman, E. Hauksson, and P. M. Shearer, 2019, Searching for hidden earthquakes in Southern California: Science, v. 364, p. 767-771.

Rost, S., and C. Thomas, 2002, Array seismology: Methods and applications: Reviews of geophysics, v. 40, p. 2-1-2-27.

Ruan, X., X. Meng, Z. Peng, F. Long, and R. Xie, 2017, Microseismic Activity in the Last Five Months before the M w 7.9 Wenchuan Earthquake: Bulletin of the Seismological Society of America, v. 107, p. 1582-1592.

Schwartz, S., 2015, Episodic aseismic slip at plate boundaries.

Shearer, P. M., 1994, Global seismic event detection using a matched filter on long-period seismograms: Journal of Geophysical Research: Solid Earth, v. 99, p. 13713-13725.

Shelly, D. R., G. C. Beroza, and S. Ide, 2007, Non-volcanic tremor and low-frequency earthquake swarms: Nature, v. 446, p. 305-307.

Shelly, D. R., W. L. Ellsworth, and D. P. Hill, 2016, Fluid-faulting evolution in high definition: Connecting fault structure and frequency-magnitude variations during the 2014 Long Valley Caldera, California, earthquake swarm: Journal of Geophysical Research: Solid Earth, v. 121, p. 1776-1795.

Shelly, D. R., and J. L. Hardebeck, 2010, Precise tremor source locations and amplitude variations along the lower-crustal central San Andreas Fault: Geophysical Research Letters, v. 37.

Shelly, D. R., D. P. Hill, F. Massin, J. Farrell, R. B. Smith, and T. a. Taira, 2013, A fluid-driven earthquake swarm on the margin of the Yellowstone caldera: Journal of Geophysical Research: Solid Earth, v. 118, p. 4872-4886.

Shelly, D. R., Z. Peng, D. P. Hill, and C. Aiken, 2011, Triggered creep as a possible mechanism for delayed dynamic triggering of tremor and earthquakes: Nature Geoscience, v. 4, p. 384-388.

Sippl, C., B. Schurr, X. Yuan, J. Mechie, F. Schneider, M. Gadoev, S. Orunbaev, I. Oimahmadov, C. Haberland, and U. Abdybachaev, 2013, Geometry of the Pamir-Hindu Kush intermediate-depth earthquake zone from local seismic data: Journal of Geophysical Research: Solid Earth, v. 118, p. 1438-1457.

Stammler, K., and L. Ceranna, 2016, Influence of wind turbines on seismic records of the Gräfenberg array: Seismological Research Letters, v. 87, p. 1075-1081.

Sun, W. F., Z. Peng, C. H. Lin, and K. Chao, 2015, Detecting deep tectonic tremor in Taiwan with a dense array: Bulletin of the Seismological Society of America, v. 105, p. 1349-1358.

Sweet, J. R., K. R. Anderson, S. Bilek, M. Brudzinski, X. Chen, H. DeShon, C. Hayward, M. Karplus, K. Keranen, and C. Langston, 2018, A community experiment to record the full seismic wavefield in Oklahoma: Seismological Research Letters, v. 89, p. 1923-1930.

Taira, T. a., A. Nayak, F. Brenguier, and M. Manga, 2018, Monitoring reservoir response to earthquakes and fluid extraction, Salton Sea geothermal field, California: Science Advances, v. 4, p. e1701536.

Tang, C. C., Z. Peng, K. Chao, C. H. Chen, and C. H. Lin, 2010, Detecting low-frequency earthquakes within non-volcanic tremor in southern Taiwan triggered by the 2005 Mw8. 6 Nias earthquake: Geophysical research letters, v. 37.

Tang, Y., M. Obayashi, F. Niu, S. P. Grand, Y. J. Chen, H. Kawakatsu, S. Tanaka, J. Ning, and J. F. Ni, 2014, Changbaishan volcanism in northeast China linked to subduction-induced mantle upwelling: Nature Geoscience, v. 7, p. 470-475.

Tibi, R., D. A. Wiens, and H. Inoue, 2003, Remote triggering of deep earthquakes in the 2002 Tonga sequences: Nature, v. 424, p. 921-925.

To, A., K. Obana, H. Sugioka, E. Araki, N. Takahashi, and Y. Fukao, 2015, Small size very low frequency earthquakes in the Nankai accretionary prism, following the 2011 Tohoku-Oki earthquake: Physics of the Earth and Planetary Interiors, v. 245, p. 40-51.

Toda, S., R. S. Stein, G. C. Beroza, and D. Marsan, 2012, Aftershocks halted by static stress shadows: Nature Geoscience, v. 5, p. 410-413.

Utsu, T., and Y. Ogata, 1995, The centenary of the Omori formula for a decay law of aftershock activity: Journal of Physics of the Earth, v. 43, p. 1-33.

Van Der Elst, N. J., and E. E. Brodsky, 2010, Connecting near-field and far-field earthquake triggering to dynamic strain: Journal of Geophysical Research: Solid Earth, v. 115.

Van der Elst, N. J., H. M. Savage, K. M. Keranen, and G. A. Abers, 2013, Enhanced remote earthquake triggering at fluid-injection sites in the midwestern United States: Science, v. 341, p. 164-167.

Vinnik, L., A. Lukk, and I. Nersesov, 1977, Nature of the intermediate seismic zone in the mantle of Pamirs—Hindu-Kush: Tectonophysics, v. 38, p. T9-T14.

Wadati, K., 1928, Shallow and deep earthquakes: Geophys. Mag., v. 1, p. 162-202.

Waldhauser, F., and W. L. Ellsworth, 2000, A double-difference earthquake location algorithm: Method and application to the northern Hayward fault, California: Bulletin of the Seismological Society of America, v. 90, p. 1353-1368.

Wallace, L. M., S. C. Webb, Y. Ito, K. Mochizuki, R. Hino, S. Henrys, S. Y. Schwartz, and A. F. Sheehan, 2016, Slow slip near the trench at the Hikurangi subduction zone, New Zealand: Science, v. 352, p. 701-704.

Walter, J. I., P. Ogwari, A. Thiel, F. Ferrer, I. Woelfel, J. C. Chang, A. P. Darold, and A. A. Holland, 2020, The Oklahoma Geological Survey Statewide Seismic Network: Seismological Research Letters, v. 91, p. 611-621.

Walter, J. I., X. Meng, Z. Peng, S. Y. Schwartz, A. V. Newman, and M. Protti, 2015, Far-field triggering of foreshocks near the nucleation zone of the 5 September 2012 (MW 7.6) Nicoya Peninsula, Costa Rica earthquake: Earth and Planetary Science Letters, v. 431, p. 75-86.

Walter, J. I., S. Y. Schwartz, J. M. Protti, and V. Gonzalez, 2011, Persistent tremor within the northern Costa Rica seismogenic zone: Geophysical Research Letters, v. 38.

Wang, B., R. M. Harrington, Y. Liu, H. Yu, A. Carey, and N. J. van der Elst, 2015, Isolated cases of remote dynamic triggering in Canada detected using cataloged earthquakes combined with a matched-filter approach: Geophysical Research Letters, v. 42, p. 5187-5196.

Wei, M., Y. Kaneko, Y. Liu, and J. J. McGuire, 2013, Episodic fault creep events in California controlled by shallow frictional heterogeneity: Nature geoscience, v. 6, p. 566-570.

Wiemer, S., 2001, A software package to analyze seismicity: ZMAP: Seismological Research Letters, v. 72, p. 373-382.

Wiens, D. A., 2001, Seismological constraints on the mechanism of deep earthquakes: Temperature dependence of deep earthquake source properties: Physics of the Earth and Planetary Interiors, v. 127, p. 145-163.

Wiens, D. A., J. J. McGuire, P. J. Shore, M. G. Bevis, K. Draunidalo, G. Prasad, and S. P. Helu, 1994, A deep earthquake aftershock sequence and implications for the rupture mechanism of deep earthquakes: Nature, v. 372, p. 540-543.

Wiens, D. A., and N. O. Snider, 2001, Repeating deep earthquakes: evidence for fault reactivation at great depth: Science, v. 293, p. 1463-1466.

Woessner, J., and S. Wiemer, 2005, Assessing the quality of earthquake catalogues: Estimating the magnitude of completeness and its uncertainty: Bulletin of the Seismological Society of America, v. 95, p. 684-698.

Wu, J., D. Yao, X. Meng, Z. Peng, J. Su, and F. Long, 2017, Spatial-temporal evolutions of early aftershocks following the 2013 Mw 6.6 Lushan earthquake in Sichuan, China: Journal of Geophysical Research: Solid Earth, v. 122, p. 2873-2889.

Xu, J., G. Liu, J. Wu, Y. Ming, Q. Wang, D. Cui, Z. Shangguan, B. Pan, X. Lin, and J. Liu, 2012, Recent unrest of Changbaishan volcano, northeast China: A precursor of a future eruption?: Geophysical Research Letters, v. 39.

Yamanaka, Y., and K. Shimazaki, 1990, Scaling relationship between the number of aftershocks and the size of the main shock: Journal of Physics of the Earth, v. 38, p. 305-324.

Yao, D., Z. Peng, and X. Meng, 2015, Remotely triggered earthquakes in South-Central Tibet following the 2004 M w 9.1 Sumatra and 2005 M w 8.6 Nias earthquakes: Geophysical Journal International, v. 201, p. 543-551.

Yao, D., J. I. Walter, X. Meng, T. E. Hobbs, Z. Peng, A. V. Newman, S. Y. Schwartz, and M. Protti, 2017, Detailed spatiotemporal evolution of microseismicity and repeating earthquakes following the 2012 Mw 7.6 Nicoya earthquake: Journal of Geophysical Research: Solid Earth, v. 122, p. 524-542.

Ye, L., T. Lay, Z. Zhan, H. Kanamori, and J.-L. Hao, 2016, The isolated~ 680 km deep 30 may 2015 Mw 7.9 Ogasawara (Bonin) Islands earthquake: Earth and Planetary Science Letters, v. 433, p. 169-179.

Yoon, C. E., O. O'Reilly, K. J. Bergen, and G. C. Beroza, 2015, Earthquake detection through computationally efficient similarity search: Science advances, v. 1, p. e1501057.

Yosinski, J., J. Clune, Y. Bengio, and H. Lipson, 2014, How transferable are features in deep neural networks?: Advances in neural information processing systems, p. 3320-3328.

Younker, L. W., P. W. Kasameyer, and J. D. Tewhey, 1982, Geological, geophysical, and thermal characteristics of the Salton Sea Geothermal Field, California: Journal of Volcanology and Geothermal Research, v. 12, p. 221-258.

Yu, W. c., and L. Wen, 2012, Deep-focus repeating earthquakes in the Tonga–Fiji subduction zone: Bulletin of the Seismological Society of America, v. 102, p. 1829-1849.

Zarifi, Z., and J. Havskov, 2003, Characteristics of dense nests of deep and intermediate-depth seismicity: Advances in geophysics, v. 46, p. 238-278.

Zecevic, M., G. Daniel, and D. Jurick, 2016, On the nature of long-period long-duration seismic events detected during hydraulic fracturingOn the nature of LPLD events: Geophysics, v. 81, p. KS113-KS121.

Zhan, Z., 2017, Gutenberg–Richter law for deep earthquakes revisited: A dual-mechanism hypothesis: Earth and Planetary Science Letters, v. 461, p. 1-7.

Zhan, Z., and H. Kanamori, 2016, Recurring large deep earthquakes in Hindu Kush driven by a sinking slab: Geophysical Research Letters, v. 43, p. 7433-7441.

Zhan, Z., H. Kanamori, V. C. Tsai, D. V. Helmberger, and S. Wei, 2014, Rupture complexity of the 1994 Bolivia and 2013 Sea of Okhotsk deep earthquakes: Earth and Planetary Science Letters, v. 385, p. 89-96.

Zhang, M., and L. Wen, 2015, An effective method for small event detection: match and locate (M&L): Geophysical Journal International, v. 200, p. 1523-1537.

Zhao, D., and Y. Tian, 2013, Changbai intraplate volcanism and deep earthquakes in East Asia: a possible link?: Geophysical Journal International, v. 195, p. 706-724.

Zhao, D., Y. Tian, J. Lei, L. Liu, and S. Zheng, 2009, Seismic image and origin of the Changbai intraplate volcano in East Asia: role of big mantle wedge above the stagnant Pacific slab: Physics of the Earth and Planetary Interiors, v. 173, p. 197-206.

Zhu, L., Z. Peng, J. McClellan, C. Li, D. Yao, Z. Li, and L. Fang, 2019, Deep learning for seismic phase detection and picking in the aftershock zone of 2008 Mw7. 9

Wenchuan Earthquake: Physics of the Earth and Planetary Interiors, v. 293, p. 106261.

Zhu, W., and G. C. Beroza, 2019, PhaseNet: a deep-neural-network-based seismic arrival-time picking method: Geophysical Journal International, v. 216, p. 261-273.

Zhuang, J., C. P. Chang, Y. Ogata, and Y. I. Chen, 2005, A study on the background and clustering seismicity in the Taiwan region by using point process models: Journal of Geophysical Research: Solid Earth, v. 110.

Zhuang, J., Y. Ogata, and D. Vere-Jones, 2002, Stochastic declustering of space-time earthquake occurrences: Journal of the American Statistical Association, v. 97, p. 369-380.

Zhuang, J., Y. Ogata, and D. Vere-Jones, 2004, Analyzing earthquake clustering features by using stochastic reconstruction: Journal of Geophysical Research: Solid Earth, v. 109.

Zigone, D., C. Voisin, E. Larose, F. Renard, and M. Campillo, 2011, Slip acceleration generates seismic tremor like signals in friction experiments: Geophysical Research Letters, v. 38.